

Thesis presented to the Instituto Tecnológico de Aeronáutica, in partial fulfillment of the requirements for the degree of Doctor of Science in the Program of Space Science and Technology, Area of Space Sensors and Actuators.

Roberto Yuji Tanaka

**STUDY OF INDIUM SEGREGATION IN SELF-ASSEMBLED
QUANTUM DOTS**

Thesis approved in its final version by signatories below:

Prof. Dr. Angelo Passaro
Advisor

Prof. Dr. Euzi Conceição Fernandes da Silva
Co-advisor

Prof. Dr. Luiz Carlos Sandoval Góes
Prorector of Graduate Studies and Research

Campo Montenegro
São José dos Campos, SP – Brazil
2016

Cataloging-in Publication Data
Documentation and Information Division

Tanaka, Roberto Yuji

Study of Indium Segregation in Self-Assembled Quantum Dots / Roberto Yuji Tanaka.

São José dos Campos, 2016.

103f.

Thesis of Doctor of Science – Course of Space Science and Technology, Area of Space Sensors and Actuators – Instituto Tecnológico de Aeronáutica, 2016. Advisor: Professor Dr. Angelo Passaro. Co-advisor: Professor Dr. Euzi Conceição Fernandes da Silva.

1. Quantum dot. 2. Inverse problem. 3. Finite Element Method. I. Instituto Tecnológico de Aeronáutica. II. Study of Indium Segregation in Self-Assembled Quantum Dots.

BIBLIOGRAPHIC REFERENCE

TANAKA, Roberto Yuji. **Study of Indium Segregation in Self-Assembled Quantum Dots**. 2016. 103f. Thesis of Doctor of Science in Space Science and Technology – Instituto Tecnológico de Aeronáutica, São José dos Campos.

CESSION OF RIGHTS

AUTHOR'S NAME: Roberto Yuji Tanaka

PUBLICATION TITLE: Study of Indium Segregation in Self-Assembled Quantum Dots

PUBLICATION KIND/YEAR: Thesis / 2016

It is granted to Instituto Tecnológico de Aeronáutica permission to reproduce copies of this thesis to only loan or sell copies for academic and scientific purposes. The author reserves other publication rights and no part of this thesis can be reproduced without his authorization.

Roberto Yuji Tanaka

Instituto de Estudos Avançados

Trevo Coronel Aviador José Alberto Albano do Amarante, nº1, Putim

12.228-001 – São José dos Campos – SP

STUDY OF INDIUM SEGREGATION IN SELF-ASSEMBLED QUANTUM DOTS

Roberto Yuji Tanaka

Thesis Committee Composition:

Prof. Dr. Nicolau Andre Silveira Rodrigues	Chairperson	- ITA
Prof. Dr. Angelo Passaro	Advisor	- ITA/IEAv
Prof. Dr. Euzi Conceição Fernandes da Silva	Co-advisor	- USP
Prof. Dr. Marcelo Marques	Internal Member	- ITA
Prof. Dr. Paulo Sérgio Soares Guimarães	External Member	- UFMG
Prof. Dr. Marcos Henrique Degani	External Member	- UNICAMP

ITA

Acknowledgments

I would like to express my great appreciation and respect to my advisors Professor Dr. Angelo Passaro and Professor Dr. Euzi Conceição Fernandes da Silva, whose excellent and enduring support and guidance had helped me to conclude this work. Their patience, motivation, and ability to demystify complex ideas had inspired me in this research. It is my hope that this thesis does not represent the end of our collaborative efforts but of a new beginning.

I am indebted to Dr. Alain André Quivy for sharing his awesome expertise in mining significant conclusions from the avalanche of data that were generated for my first publication. I am also most grateful to all my colleagues whose coffee-time chatter has always provided not only a light relief from my work but also a pleasant research atmosphere: Nancy Mieko Abe, Onofre Felix de Lima Neto, Gustavo Soares Vieira, Carlos Alberto da Silva Jr., Wakim Boulos Saba, Marcio Martins da Silva Costa, Diogo de Moura Pedroso, Natalia Maria Antonangelo Athanazio, Tiago Gonçalves Santos, Reviane Cristina Lopes, André Flederico Pereira, and Dárley Domingos de Almeida.

I thank Vanusa Candia de Sousa and my family for understanding when my path kept me away from them, and for supporting and encouraging me along the way.

This study was made possible by the financial assistance of the Instituto Nacional de Ciência e Tecnologia em Nanodispositivos Semicondutores (INCT-DISSE) and the Brazilian funding foundation CNPq (310578/2012-4 and 304265/2012-8).

"An expert is a man who has made all the mistakes which can be made in a very narrow field".

Niels Bohr (1885-1962)

As quoted by Edward Teller (10 October 1972), and A Dictionary of Scientific Quotations (1991) by Alan L. Mackay, p. 35

Resumo

Pontos quânticos auto-organizados de InAs/GaAs apresentam uma composição não-homogênea de átomos de índio resultante de efeitos de segregação e difusão de átomos entre camadas. Atualmente, não existe um método para obter informações em tempo real a respeito da migração dos átomos dentro de pontos quânticos. Medidas de raio-x “*ex-situ*” são sempre possíveis mas o volume diminuto dos pontos quânticos tornam o gradiente da concentração de índio dentro destas nanoestruturas praticamente imperceptível nas medidas. A descrição do perfil de composição de índio é crucial em qualquer cálculo. Nesta tese é apresentado um procedimento inédito que combina um método de resolução da equação de Schrödinger baseada em Elementos Finitos e métodos de otimização metaheurística para acertar os picos de fotoluminescência por meio de um ajuste fino da distribuição de índio dentro de pontos quânticos de $\text{In}_x\text{Ga}_{1-x}\text{As}/\text{GaAs}$ crescidos por epitaxia de feixe molecular. Este procedimento leva em conta tanto a variação vertical quanto radial na composição de índio dentro dos pontos quânticos resultantes de efeitos de segregação e difusão.

Abstract

Self-assembled InAs/GaAs quantum dots have a non-homogeneous indium composition profile resulting from segregation and intermixing effects. Currently, there is not a method to obtain any real-time information on the migration of atoms inside the quantum dots. *Ex-situ* x-ray measurements are always possible, but in general, the very small volume of the quantum dots makes the signal almost insensitive to the indium gradient inside these nanostructures. The description of this indium composition profile is most crucial in any calculation. This thesis presents a novel iterative procedure that combines a Finite Element based solver for the Schrödinger equation and a metaheuristic optimization to match experimental photoluminescence peaks by fine-tuning the indium distribution inside $\text{In}_x\text{Ga}_{1-x}\text{As}/\text{GaAs}$ quantum dots grown by molecular-beam epitaxy. This procedure takes into account both the vertical and radial indium-composition profiles resulting from segregation and intermixing effects.

List of Figures

FIGURE 1.1 – Infrared atmospheric transmission spectre. Reproduced from [18].	28
FIGURE 1.2 – The band gap of $\text{Hg}_{1-x}\text{Cd}_x\text{Te}$ as a function of fraction mole x of CdTe at 0 K.	29
FIGURE 1.3 – XSTM images of a layer of self-assembled QDs in (a) an as grown sample and (b) an annealed sample. The arrows indicate the growth direction. Reproduced from [36].	31
FIGURE 2.1 – Schematic illustration of two type of strained growth. Adapted from [72].	36
FIGURE 2.2 – PL arrangement, with laser, sample and cryostat, monochromator, and detector (D). Lens (L) focuses the PL signal; filters F1 and F2 block unwanted laser light; choppers C1 and C2 modulate the intensity of a light beam. Adapted from [85].	40
FIGURE 2.3 – Schematic electronic band structure of a QD. VB and CB stand for valence and conduction bands, respectively.	40
FIGURE 2.4 – (a) Three-dimensional model showing the lens-shaped QD in blue color and the front removed enclosing cylinder in red. (b) The axially symmetric QD model for our FEM implementation, showing the mesh close to the QD. The lines Γ_1 indicate where boundary condition of Dirichlet type is applied. The lines Γ_2 indicate where boundary condition of Neumann type are applied. The insets show details of the mesh inside the QD, as well as an element τ of the mesh.	42
FIGURE 2.5 – Model of a lens-shaped QD (spherical cap from a sphere of radius R) with a radius R_{QD} and height H_{QD} inside a large cylinder of radius R_c and height H_c .	44
FIGURE 3.1 – Conduction and valence band profiles of a $\text{GaAs}/\text{In}_x\text{Ga}_{1-x}\text{As}/\text{GaAs}$ heterostructure with and without taking into account lattice mismatch strain.	48
FIGURE 3.2 – Perpendicular and parallel components of electron effective mass for $\text{In}_x\text{Ga}_{1-x}\text{As}$ as a function of indium concentration, x .	49

FIGURE 3.3 – General scheme of the <i>sdk-levsoft</i> library. The white boxes indicate the modules that had classes included or modified in this thesis.....	49
FIGURE 3.4 – Partial classes of the finite element module. The white boxes indicate the classes that were developed or modified in this thesis.....	50
FIGURE 3.5 – Partial classes of the phenomenon and project modules. The white boxes indicate the classes that were developed or modified in this thesis.	51
FIGURE 3.6 – Diagram of the classes that treat the automatic building of FEM model.	51
FIGURE 3.7 – Some meshes created to study the influence of the mesh refinement on the convergence of the calculations with FEM.....	53
FIGURE 3.8 – Convergence of the ground state z_0^1	54
FIGURE 3.9 – Convergence of the ground state z_1^1	54
FIGURE 3.10 – Convergence of the ground state z_2^1	55
FIGURE 3.11 – Convergence of the ground state z_0^2	55
FIGURE 3.12 – Convergence of the state z_4^1	56
FIGURE 3.13 – Convergence of the state z_0^4	56
FIGURE 3.14 – Convergence of the state z_4^4	57
FIGURE 3.15 – Computation time as a function of the mesh density for the case of infinite spherical potential well.	57
FIGURE 3.16 – Various views of the probability density computed with FEM for the state z_0^1	58
FIGURE 3.17 – Energies of the ground-state as a function of QD radius for different QD heights computed with the Expansion Method (dashed line) and FEM (continuous line).	59
FIGURE 3.18 – Energies of the first excited state as a function of QD radius for different QD heights computed with the Expansion Method (dashed line) and FEM (continuous line).	59

FIGURE 3.19 – Convergence curve of the ground state as a function of the density of elements using first order finite elements of Lagrangian-type (diamond) and Hermitian-type (circle).....	61
FIGURE 3.20 – Convergence curve of the first excited state as a function of the density of elements using first order finite elements of Lagrangian-type (diamond) and Hermitian-type (circle).....	61
FIGURE 3.21 – Computational time to compute the energies of confined states as a function of the density of elements using first order finite elements of Lagrangian-type (diamond) and Hermitian-type (circle).	61
FIGURE 3.22 – Concentration of indium in the n -th monolayer of the WL. The arrow indicates the growth direction. Therefore, $n = 1$ indicates the lowest layer of the WL.....	63
FIGURE 3.23 – FEM model of a lens-shaped QD (a) without WL and (b) with WL.	64
FIGURE 3.24 – Indium composition x ($\text{In}_x\text{Ga}_{1-x}\text{As}$).	64
FIGURE 3.25 – Energy values of the ground state in the conduction band and the valence band for several pure InAs QDs with different heights and base radius. The dashed line curves were computed without WL and the continuous line with WL.	65
FIGURE 3.26 – Energy values of the first excited state in the conduction band and the valence band for several pure InAs QDs with different heights and base radius. The dashed line curves were computed without WL and the continuous line with WL.	65
FIGURE 3.27 – Comparison of computation time between a case set calculated without the WL (dashed line) and calculated with the WL (continuous line). Case set with QD height of 3 nm.	66
FIGURE 3.28 – Models of indium distribution within QDs: (a) Giddings, (b) Blokland.....	68
FIGURE 3.29 – Flowchart of the inverse problem.	72

FIGURE 4.1 – (a) Low-temperature PL spectrum of the reference QD sample. (b) TEM image of the same sample showing a typical QD after GaAs capping. The full line shows the lens shape adopted in the first simulations, while the dashed line represents the disk shape used in the last simulations of this monograph. (Reproduced from [70].)	73
FIGURE 4.2 – Energy values of the fundamental transition energy $e1hh1$ from the ground state ($e1$) in conduction band to the first heavy-hole state ($hh1$) in the valence band for several QD heights and base radii. Comparison between the Giddings model and pure InAs QD results.	74
FIGURE 4.3 – Transition energies $e1hh1$ from the ground state ($e1$) in conduction band to the first heavy-hole state ($hh1$) in the valence band and $e2hh1$ from the first excited state ($e2$) in conduction band to the first heavy-hole state ($hh1$) in the valence band for several QD heights and base radii. Comparison between the Blokland model and pure InAs QD results.	75
FIGURE 4.4 – Theoretical results of indium distribution that reproduce the experimental PL peaks according to the Giddings model using the parameters values presented in Table 4.1.	77
FIGURE 4.5 – Theoretical results of indium distribution that reproduce the experimental PL peaks according to the Giddings model using the parameters values presented in Table 4.2.	79
FIGURE 4.6 – Profile of indium distribution and elastic potential energy for the best solution found according to the Giddings model using the parameters values presented in Tables 4.1 and 4.2.	81
FIGURE 4.7 – Theoretical results of indium distribution according to the Giddings model ..	84
FIGURE 4.8 – Plot of the elastic potential energy as a function of the value of parameter X.	85
FIGURE 4.9 – Plots of the parameters β (diamond) and γ (circle) as a function of the value of parameter X.	85
FIGURE 4.10 – Comparison between the case with the smallest (“L_EA_16”) elastic potential energy and the greater (“L_EA_12”) one. Dimensions (height x length) of rectangle	

with continuous lines: 10 nm x 20 nm. Dimension of rectangle with dotted lines:
4 nm x 10 nm. 86

FIGURE 4.11 – Strain distribution for the case “L_EA_16”. Dimensions (height x length) of a
rectangle with continuous lines: 10 nm x 20 nm. Dimension of rectangle with dotted lines:
4 nm x 10 nm. 86

List of Tables

TABLE 3.1 – Energy values obtained from the semi-analytical solution of an infinite spherical potential with radius of 10 nm, in eV. z_l^n represents the state with principal quantum number n and azimuthal quantum number l (see Appendix B).	52
TABLE 3.1 – Components of the inverse problem.	69
TABLE 4.1 – Values of parameters α , β , γ , and X for the cases with smallest values of objective function for a lens-shaped QD ($R_{\text{QD}} = 10$ nm, $H_{\text{QD}} = 4$ nm).	76
TABLE 4.2 – Values of parameters α , β , γ , and X for the cases with smallest values of objective function for a disk-shaped QD ($R_{\text{QD}} = 8$ nm, $H_{\text{QD}} = 4$ nm).	78
TABLE 4.3 – Values of parameters α , $\beta \cdot R_{\text{QD}}$, $\gamma \cdot H_{\text{QD}}$, and X for the best cases ordered by objective function ($R_{\text{QD}} = 20$ nm, $H_{\text{QD}} = 10$ nm, $*R_{\text{QD}} = 8$ nm, $*H_{\text{QD}} = 4$ nm).	82
TABLE A.1 – Values of parameters E_g^0 , A and B. Sources [76, 78].	101
TABLE A.2 – Values of parameters F , E_P , Δ_{SO} , γ_1 , γ_2 , and VBO. Source [76].	101
TABLE A.3 – Values of parameters C_{11} , C_{12} , C_{44} , a_c , a_v , b e a^{lc} . Sources [76, 78].	102
TABLE A.4 – Bowing values for ternary alloys. Source [76].	102

List of Abbreviations and Acronyms

BH	Black Hole
FEM	Finite Element Method
DCTA	Department of Aerospace Science and Technology (from “Departamento de Ciência e Tecnologia Aeroespacial”)
GA	Genetic Algorithm
IEAV	Institute of Advanced Studies (from “Instituto de Estudos Avançados”)
LEV	Virtual Engineering Laboratory (from “Laboratório de Engenharia Virtual”)
MBE	Molecular Beam Epitaxy
PL	Photoluminescence
PSO	Particle Swarm Optimization
QD	Quantum Dot
QW	Quantum Well
RHEED	Reflection High-Energy Electron Diffraction
SDK	Software Development Kit
STM	Scanning Tunneling Microscopy
TEM	Transmission Electron Microscopy
WL	Wetting Layer

List of Symbols

$a_c, a_v, \text{ and } b$	deformation potentials
C	elastic stiffness constants of the crystalline semiconductor material
E_g	band gap energy
E_P	electron momentum
E_X	exciton binding energy
F	Kane parameter
\mathbf{k}	wave vector
m_0	free electron mass
m_q	azimuthal quantum number
m^*	effective mass
m_{\perp}^*	perpendicular effective mass
$m_{//}^*$	in-plane effective mass
\mathbf{M}	effective mass tensor of particle
n_e	total number of finite elements
n_p	number of nodal points in the finite element
N	set of base functions of the finite element
P	arbitrary weighting function
Q	quantum well width in quantity of monolayers
\mathbf{r}	position vector
R	diffusion parameter
T	temperature
U	elastic potential energy

V	potential energy band edge
x	molar concentration of a compound in a ternary alloy
W_{AB}	bowing parameter used to compute the value of a ternary alloy property from the values of the property in the constituent binary compounds A and B
A and B	Varshni parameters when used in equations related to semiconductor materials parameters
Δ_{SO}	spin-orbit coupling parameter
ε	strain
γ	Luttinger parameter
Γ	domain boundary
Ω	domain of a function
ψ	wave function
τ	a generic finite element

Contents

ACKNOWLEDGMENTS.....	V
RESUMO.....	IX
ABSTRACT	XI
LIST OF FIGURES.....	XIII
LIST OF TABLES.....	XIX
LIST OF ABBREVIATIONS AND ACRONYMS.....	XXI
LIST OF SYMBOLS.....	XXIII
1 INTRODUCTION	27
2 MATHEMATICAL FORMULATIONS.....	35
2.1 Elastic potential energy	35
2.2 Electronic structure parameters	37
2.3 Photoluminescence.....	39
2.4 Numerical methods.....	41
2.4.1 Finite Element Method	41
2.4.2 Expansion Method.....	44
3 METHODOLOGY AND IMPLEMENTATION	47
3.1 InAs/GaAs material system	47
3.2 Computational codes	49
3.2.1 Convergence study of the finite element module	52
3.2.2 Validation of the finite element module with the Expansion Method.....	58
3.2.3 The finite element of Hermitian-type	60

3.3	The wetting-layer	62
3.4	Nonuniform indium distribution within QD	66
3.4.1	The inverse problem.....	68
3.4.2	Software implementation	71
4	RESULTS AND DISCUSSION	73
4.1	The elastic potential energy.....	80
5	CONCLUSION AND FUTURE WORKS	87
5.1	Dots-in-a-well nanostructures.....	89
5.2	Vertically aligned QDs.....	90
	BIBLIOGRAPHY	91
	APPENDIX A – SEMICONDUCTOR PARAMETERS VALUES	101
	APPENDIX B – SOLUTION OF THE SCHRÖDINGER EQUATION FOR THE INFINITE SPHERICAL POTENTIAL WELL.....	103

1 Introduction

Quantum dots (QDs) are semiconductor nanostructures that confine carrier in all three spatial dimensions, and consequently the energy levels in these nanostructures have properties that resemble those of an atom. QDs can be produced in many different shapes and sizes, with dimensions ranging from a few to dozens of nanometers. Spherical-shaped QDs have electron wave functions similar to atoms due to their spherical symmetry. However, unlike atoms, QDs are not restricted to a spherical shape and, therefore, different electronic shell structures are possible. Moreover, whereas the spacing of the atomic energy levels is about 1-10 eV, the spacing of energy levels in semiconductor QDs is on the order of 1-10 meV. This fact suggested that QDs could be used to investigate phenomena that are experimentally challenging or even unattainable in atoms like the study performed by Kouwenhoven, Austing, and Tarucha 2001 [1], which presents the effect of magnetic fields on the electronic shells of QDs. Magnetic field on the order of 1 T is sufficient to considerably change the shape of electronic shells in QDs, but a similar modification in the electronic shell of atoms would require magnetic fields on the order of 10^6 T [1]. With such characteristics, QDs unlock nanoscale phenomena that are very interesting not only for scientific research but also for technological applications with potential use in novel or improved performance devices in areas such as lasers [2–4], quantum information [5–8], photodetectors [9, 10], and solar cells [11, 12]. While lasers based on QDs have already reached commercialization level, other QD devices still face the challenge of finding the theoretically expected high performance. The following paragraphs present some applications of QDs in memory devices, photodetectors, and solar cells.

At present, the memory density of hard disk drives based on magnetic technology is in the order of 0.47 Tb/cm^2 [13, 14]. Imamura *et al.* [15] proposed a concept of device that may increase the memory density: an optical memory device based on QDs that employs the memory effect by photocurrent. Such optical memory devices present the possibility of storing one bit per QD, so that a surface density of one QD per 100 nm^2 would have a memory density of 10^{12} bit/cm^2 (1 Tb/cm^2). The spin of an electron in QDs may also be used to store and retrieve quantum information. On this line of investigation, Kroutvar *et al.* [16] proposed an electron spin memory device using semiconductor QDs. Therefore, this is a spintronic device, as opposed to the Imamura *et al.*, which is an optical device. Besides

memory devices, the long coherence time of electron spin in QDs [17] also promotes fields such as quantum computing and quantum cryptography.

The gases that compose the atmosphere of the Earth absorb electromagnetic energy in very specific regions of the spectrum. Figure 1.1 shows the infrared atmospheric transmission spectrum. There are regions of the electromagnetic spectrum that are weakly absorbed and, consequently, present high transmission rates through atmosphere. Those regions are known as atmospheric windows and they are represented by the blue areas tagged with SWIR (short-wavelength infrared), MWIR (mid-wavelength infrared), and LWIR (long-wavelength infrared) in Figure 1.1. Most remote sensors onboard aircrafts and Earth observation satellites operate in one or more of these windows. These sensors are engineered to detect specific wavelengths that pass through the atmosphere such as the mid-wave infrared (3–5 μm) and the long-wave infrared (8–12 μm) regions. Moreover, many molecular compounds have vibrational modes in the 3–17 μm part of the spectrum. Exploring the electromagnetic emissions associated to these vibrational modes allows, for instance, the detection and measurement of air pollutants and detection of hidden explosives.

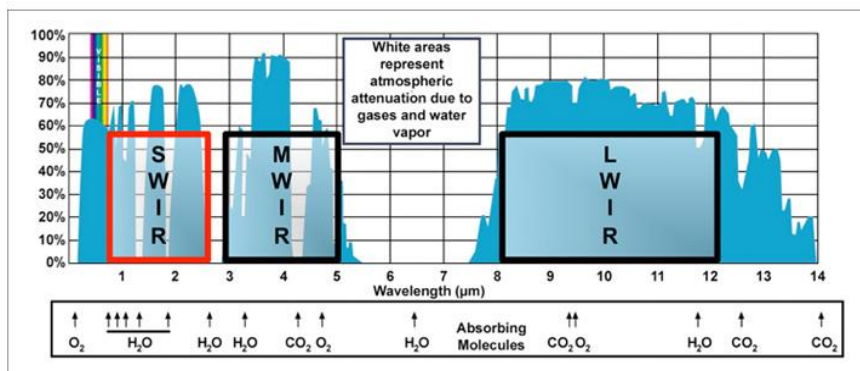


FIGURE 1.1 – Infrared atmospheric transmission spectre. Reproduced from [18].

Besides, the mid-wave infrared window is interesting because this is the region of the wavelength signature of jet engines exhaust plume that guided missile sensors are adjusted to seek. Detection of these regions requires semiconductor materials with narrow band-gaps (0.10–0.41 eV) corresponding to photon energies in these windows. Nowadays, the commercial devices that operate in these regions of infrared spectrum are concentrated in two technologies. One is based on bulk semiconductor materials and the other on quantum well nanostructures. Two semiconductor materials dominate the fabrication of bulk detectors [19]: indium antimonide (InSb) and mercury cadmium telluride (HgCdTe) semiconductors. The first has been fabricated commercially since the late 1950's and the other a little past in 1962

when the first HgCdTe-based detector was created. Bulk detectors have achieved great commercial penetration due to ease of large-scale fabrication and high detectivity at cryogenic temperatures. However, InSb-based detectors lack wavelength tunability. HgCdTe system allows wavelength tunability through material composition but precise control to obtain a fine-tuned fraction mole of CdTe compound is a major issue for HgCdTe-based devices, particularly as the band gap of the material decreases towards the detection of long-wave infrared (8–12 μm) and beyond [20]. Figure 1.2 shows the energy gap of $\text{Hg}_{1-x}\text{Cd}_x\text{Te}$ as a function of fraction mole of CdTe at 0 K obtained from the most widely used expression [21]:

$$E_g(x, T) = -0.302 + 1.93x + 0.000535(1 - 2x)T - 0.81x^2 + 0.832x^3. \quad (1.1)$$

As the band gap goes down, variation of the mole composition of HgCdTe by 0.001 can have drastic effects on the performance of a detector and that level of control is extremely difficult, regardless of the growth method.

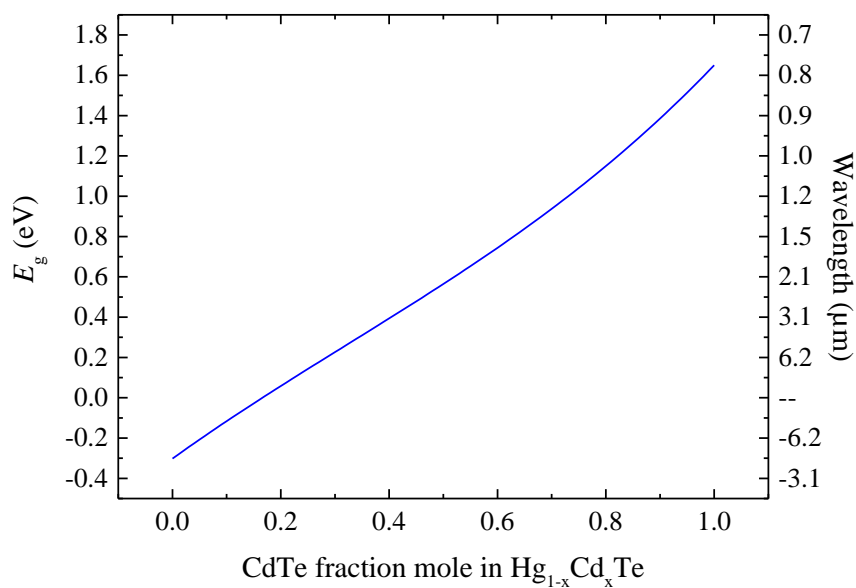


FIGURE 1.2 – The band gap of $\text{Hg}_{1-x}\text{Cd}_x\text{Te}$ as a function of fraction mole x of CdTe at 0 K.

With regard to quantum-well infrared photodetectors (QWIPs), its main disadvantage is the insensitivity to normally incident radiation, thus requiring complicated optical systems. QD-based infrared photodetectors (QDIPs) offer a very promising future alternative, which would be sensitive to normally incident radiation and would presumably have very low dark currents even at room temperature due to the three-dimensional confinement of electrons in the QD [22]. QDIPs have been demonstrated to be superior to QWIPs but their full potential has not yet been achieved, and QDIPs are currently under intensive experimental and theoretical study [23–26]. Moreover, the delta function-like density of states of QDs

theoretically ensures strong luminescence over a narrow spectrum even at high temperatures [27] making them more efficient sources for several optoelectronics applications. Long-distance telecommunication [28, 29] has huge demands for high-quality emitters and receivers matching the absorption and dispersion minimum of optical fibers (wavelengths of 1.3 μm and 1.5 μm). The selectivity characteristic of a QD makes it ideal candidate to build such devices and would benefit several applications relied on optical fibers.

Concerning energy sources, there has been a global focus to search for new and renewable energy sources motivated by possible energy shortage and by demands of environmental protection. Solar energy is one of the promising candidates for clean and renewable energy. Moreover, photovoltaic solar panels are the main powering device for spacecrafts and satellites operating in the inner Solar System. For space applications, solar cells made of III-V compound semiconductors are typically favored over crystalline silicon because they have higher efficiency and power to mass ratio [30]. Nowadays, the best single-junction solar cell is based on GaAs and it demonstrates an efficiency of 28.8% and go up to 38.8% if multi-junction is considered [31]. Much of the lower energy (lower than band gap of semiconductor) components of the solar spectrum are simply lost because they do not contain enough energy to create an exciton for photocurrent generation. The introduction of impurity or intermediate bands [32] is an alternative approach to bypass this efficiency. Theoretically, a single intermediate band could raise the efficiency to 63% and could go up to 85% by considering an infinite number of bands [33]. The presence of an array of semiconducting QDs within the junction of a p-type / intrinsic / n-type cell may lead to the formation of an energy band or bands within the band gap of the solar cell making these nanostructures a promising candidate for this technology [34, 35].

For illustrative purpose, Figure 1.3 shows a cross-sectional scanning tunneling microscopy (XSTM) image of a InAs/GaAs layer of self-assembled QDs reproduced from [36], in which InAs (GaAs) rich regions appear bright (dark) and the arrow indicates the growth direction. Figure 1.3-a refers to the as grown sample and Figure 1.3-b refers to the annealed sample.

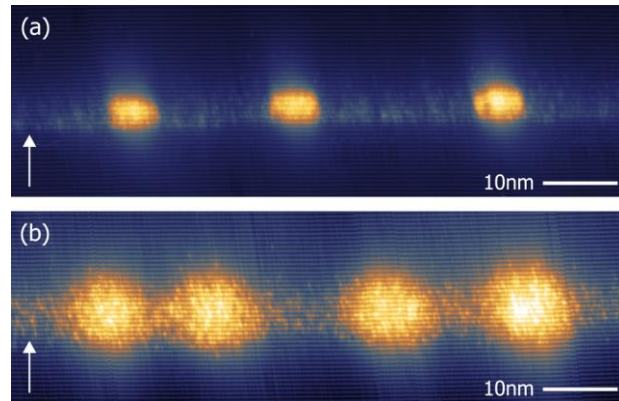


FIGURE 1.3 – XSTM images of a layer of self-assembled QDs in (a) an as grown sample and (b) an annealed sample. The arrows indicate the growth direction. Reproduced from [36].

In order to realize the potentials and exploit the possibilities mentioned above further knowledge of the fundamental physics involving these nanostructures is still necessary. For this purpose, several researchers are conducting further studies in the understanding of the mechanisms behind the formation and composition of self-assembled QDs built by heteroepitaxial growth. The heteroepitaxial growth of crystalline semiconductor material occurs when the chemical identity of the epitaxial layer differs from that of the substrate. When these two materials have a misfit in their lattice parameters, the growth occurs in a strained mode. Generally, small misfits are accommodated by elastic distortions in which the deposited layer maintains the coherence with the substrate lattice, but greater misfits lead to plastic deformation (dislocations) in the strained layer. However, some highly strained heteroepitaxial systems (lattice mismatch $\geq 3\%$) present a transition in the growth-mode from two-dimensional to three-dimensional nucleation prior to the incorporation of dislocations, forming coherently strained (defect-free) QDs [37]. During the QD formation process, a wetting layer (WL) is formed and may remain depending on the system and growth conditions. Self-assembly of QDs has proven to be the most attractive approach to grow these nanostructures because it allows the production of a large number of coherently strained and relatively homogeneous QDs [38, 39] without slow and costly lithography steps.

Bimberg *et al.* [40] and Prior *et al.* [41] are the pioneers to investigate the nature of the strain tensor in QD nanostructures and the strain effects are reviewed in details by Stangl *et al.* [39]. Actually, there are strong evidences that the trade-off between coherency energy and surface energy explain the strain-induced formation of QDs, however the detailed mechanism of nucleation and growth remains an open question [42–51]. Anyway, generally speaking, the formation of a coherently strained QD is associated with an overall relaxation of the strain energy. The elastic potential relaxation, which initially drives the QD configuration,

is opposed by the increase in surface energy associated with the increase in total surface area due to the island formation. Because of this increase in surface energy, the growth of the QDs is limited, and the strain energy of the system is not fully eliminated [51, 52]. This balance makes the QD formation very sensitive to variations on the main growth parameters. Furthermore, the size, shape, and chemical composition of a self-assembled QD are subject to random fluctuations, even in the presence of ordering mechanism. Deeply related to the strain, issues such as the shape [52–54] and composition [55–61] of the QDs are still source of considerable debate in the literature, since they have direct impact on the effectiveness of QD-based devices.

Coherently strained QDs usually have a non-homogeneous composition [62–64]. The non-homogeneous composition profile can be caused not only by intermixing of QDs with the surrounding layers (substrate and cap layer) [55] but also by atomic diffusion effects [65]. These atomic migrations cannot be tracked precisely neither by *in situ* techniques like reflection high-energy electron diffraction (RHEED) nor by *ex situ* techniques like x-ray measurements. In general, the very small volume of the QDs makes the signal of these measurements almost insensitive to the indium gradient inside these nanostructures [66–69]. Biasiol *et al.* [58] reviewed the experimental works on the compositional mapping of semiconductor QDs.

In this context, the objective of this thesis is to contribute to the study of self-assembled QDs. In order to achieve this end, several independent computer modules were developed:

- a module that compute the remaining elastic potential energy from lattice mismatch in the nanostructure and other quantities such as photoluminescence peaks of energy (Chapter 2, Sections 2.1 and 2.3);
- a class of material properties for several semiconductors of family III-V and theirs alloys. This class of material properties takes into account the effect of strain in the energy of gap and effective mass of charges in lattice mismatched strained films, the effective mass anisotropy, and the effect of temperature on the values of these properties (Chapter 2, Section 2.2);
- a solver for the Schrödinger equation using the Finite Element Method in which the effective mass anisotropy and the azimuthal quantum number due to axisymmetric symmetry are taken into account (Chapter 2, Section 2.4.1);

- an automated builder for the finite element model of the QD nanostructure. This module constructs the geometric model, the mesh, and attributes the materials and boundary conditions (Chapter 3, Section 3.2);
- a module that combine all the previous modules with a metaheuristic optimization framework to solve the inverse problem of non-homogeneous material distribution in a sample of self-assembled QDs given as input a measured physical quantity such as the photoluminescence peak energy obtained from a sample (Chapter 3, Section 3.4).

The last module contributed to investigate the composition of a sample grown by Molecular Beam Epitaxy (MBE). The results from this investigation were published in [70]. A summary of this study is presented in Chapter 4. In principle, it focuses on InAs/GaAs system although most of the approaches and conclusions presented in that article will apply to other systems of self-assembled structures.

Finally, the set of the developed computer codes is novel and up-to-date in the field of QDs. An optoelectronic device designer will undoubtedly benefit from simulations that are possible to execute with developed software, as it certainly would help shorten then development lifecycle of a prototype. For example, in a computer aided design environment, the part of the code that computes the electronic structure may be used to engineer the effective bandgap energy of the strained QDs. With further studies using this software, a designer can make an enlightened decision as to how many QD layers should be stacked vertically, how thick the QD layers and barrier spacing should be, how much lateral expansion of the dots of the higher layers can be expected and so forth. These are intricate questions, which are susceptible to affect the device performance and thus require an in-depth analysis of the material. Both, the bandgap engineering considering the strain and the study of vertically coupled QDs will be handled in future works and are not treated in this thesis.

This thesis is organized as follows. The theme of this thesis is introduced in Chapter 1. It also contains some motivations and summarizes the achievements of this work. The theoretical background and the mathematical formulations to compute several phenomena in a nanostructure based on self-assembled QDs are presented in Chapter 2. The methodology and the computer code developed in this work as well as validation tests are presented in Chapter 3. The results are presented in Chapter 4. The conclusions, recommendations, and potential extensions of this work are presented in Chapter 5.

2 Mathematical formulations

This chapter presents the theoretical framework used in this thesis together with the mathematical modeling of the electronic structure of semiconductor QDs and QWs as well as the numerical methods applied to solve the differential equation used to model the electronic states of these nanostructures.

Devices based on QDs make use of the quantized energy levels of electrons and holes in these nanostructures to control the flow of charge. In this work, the effective-mass envelope-function theory [71] is assumed valid for both electron and hole within each semiconductor layer in the nanostructure. In this approach, the quantized levels, described by eigenstates, are computed by solving the Schrödinger equation:

$$\hat{H}\Psi(\mathbf{r}) = E\Psi(\mathbf{r}) \Leftrightarrow \left\{ -\frac{\hbar^2}{2} \nabla \cdot [\mathbf{M}(\mathbf{r}) \nabla] + V(\mathbf{r}) \right\} \Psi(\mathbf{r}) = E\Psi(\mathbf{r}), \quad (2.1)$$

where ∇ stands for the vector differential operator, \mathbf{r} represents the particle position, $\mathbf{M}(\mathbf{r})$ is the space-dependent electron or hole effective mass tensor, and $\Psi(\mathbf{r})$ is the wave function. The potential energy $V(\mathbf{r})$ is determined by the conduction- or valence-band offset at the heterojunction, and includes strain effects. The formulation to compute the elastic potential energy from the lattice parameter misfit is presented in Section 2.1. The mathematical formulations to compute the potential energy and the effective masses are presented in Section 2.2. Section 2.3 contains the background to compute photoluminescence peak transition energies. The numerical methods to solve Equation (2.1) are presented in Section 2.4.

2.1 Elastic potential energy

There are several approaches to calculate the strain profiles in a self-assembled nanostructure [41]. In this work, it is adopted the approach based on classical elasticity [72, 73] in which the potential energy is computed calculating the relative displacement of each lattice site. If a thin epitaxial layer is deposited on a much thicker substrate then the lattice constant $a_d^{\text{lc}}(\mathbf{r})$ in the plane perpendicular to the growth direction will be forced to adjust itself to the lattice constant of the substrate a_s^{lc} . Consequently, the epitaxial layer lattice is under

biaxial stress along the growth interface and while no force is applied along the growth direction, the crystal is able to relax freely along that direction. This biaxial stress results in the appearance of an in-plane strain, which in defect-free case can be calculated as

$$\varepsilon_{//}(\mathbf{r}) = \varepsilon_{xx}(\mathbf{r}) = \varepsilon_{yy}(\mathbf{r}) = \frac{a_s^{lc} - a_d^{lc}(\mathbf{r})}{a_d^{lc}(\mathbf{r})}. \quad (2.2)$$

In the perpendicular direction, just like the width of a rubber band contracts when it is stretched along its length, the lattice constant in the growth direction is still forced to change due to the Poisson effect, defining two types of coherently strained growth depending if the lattice constant of the epitaxial layer is either smaller (Figure 2.1-a) or larger (Figure 2.1-b) than the lattice constant of the substrate. In the first case, there is a tensile strain ($\varepsilon_{//} > 0$) which forces it to expand and in the second case, there is a compressive strain ($\varepsilon_{//} < 0$) which forces the lattice constant of the epitaxial layer to shrink.

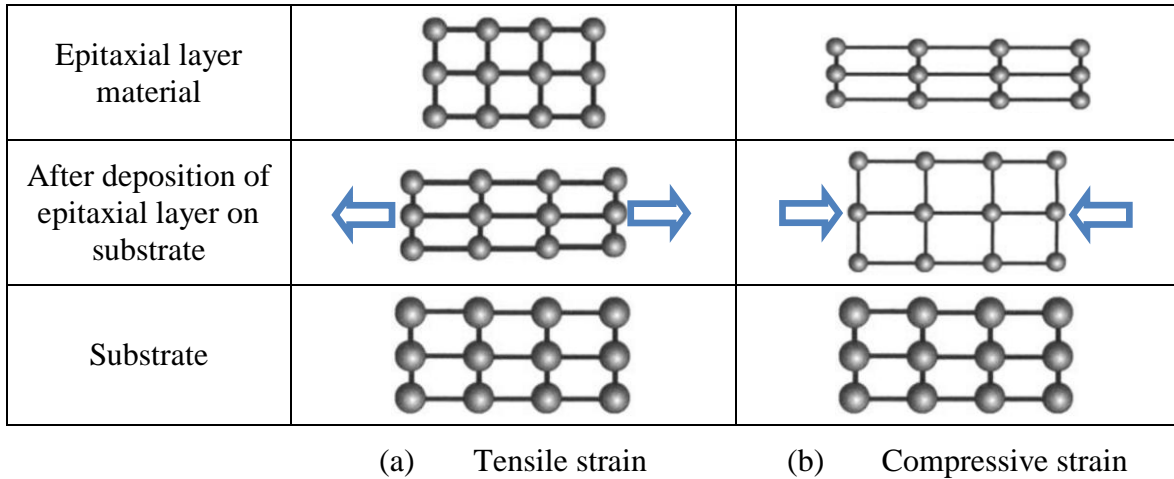


FIGURE 2.1 – Schematic illustration of two type of strained growth. Adapted from [72].

The ratio that determines the increase or decrease of the lattice constant due to in-plane stress is called Poisson ratio ν , which connects the in-plane and the perpendicular strain:

$$\varepsilon_{\perp}(\mathbf{r}) = \varepsilon_{zz}(\mathbf{r}) = -\nu \varepsilon_{//}(\mathbf{r}). \quad (2.3)$$

For the commonly used cubic semiconductor materials grown along the [001] direction, the perpendicular strain is given by [72]:

$$\varepsilon_{\perp}(\mathbf{r}) = -2 \frac{C_{12}(\mathbf{r})}{C_{11}(\mathbf{r})} \varepsilon_{//}(\mathbf{r}). \quad (2.4)$$

The parameter $C_{ij}(\mathbf{r})$, in which i and j are integers, is the elastic stiffness constants of the crystalline semiconductor material.

The total elastic strain energy in cubic semiconductor materials grown along the [001] is given by [74, 75]:

$$U = \int_V \left\{ \frac{1}{2} C_{11}(\mathbf{r}) [\varepsilon_{xx}^2(\mathbf{r}) + \varepsilon_{yy}^2(\mathbf{r}) + \varepsilon_{zz}^2(\mathbf{r})] + 2C_{44}(\mathbf{r}) [\varepsilon_{xy}^2(\mathbf{r}) + \varepsilon_{yz}^2(\mathbf{r}) + \varepsilon_{zx}^2(\mathbf{r})] + C_{12}(\mathbf{r}) [\varepsilon_{xx}(\mathbf{r})\varepsilon_{yy}(\mathbf{r}) + \varepsilon_{yy}(\mathbf{r})\varepsilon_{zz}(\mathbf{r}) + \varepsilon_{zz}(\mathbf{r})\varepsilon_{xx}(\mathbf{r})] \right\} dV, \quad (2.5)$$

For heterojunctions made of two zinc-blended-structure materials, the off-diagonal strain components are all zero ($\varepsilon_{xy} = \varepsilon_{yz} = \varepsilon_{zx} = 0$) due to crystal symmetry.

2.2 Electronic structure parameters

This section deals with the computation of the two input parameters for the Schrödinger Equation (2.1), the effective-mass tensor \mathbf{M} and the band-edge profile V . These parameters are determined from several measured or estimated parameters of the materials that compound the structures. The definitions and values of these parameters can be obtained in [76–78].

The effective mass of a charge carrier is related to the curvature of the dispersion relation in which it is moving [78] and can be obtained from the bulk energy dispersion defined by [76, 79]:

$$m^* = \hbar^2 \left(\frac{\partial^2 E}{\partial \mathbf{k}^2} \right)^{-1}, \quad (2.6)$$

where \mathbf{k} represents the wave vector of the particle. Using this procedure, the electron effective mass in the conduction (electron) and valence bands (heavy hole and light hole) can be approximated in terms of the band parameters by [76]:

$$\frac{m_0}{m_e^*(\mathbf{r})} = 1 + 2F(\mathbf{r}) + \frac{E_p(\mathbf{r}) + \frac{2}{3}E_p(\mathbf{r})E_g(\mathbf{r})\Delta_{SO}(\mathbf{r})}{E_g(\mathbf{r}) + \Delta_{SO}(\mathbf{r})}, \quad (2.7a)$$

$$\frac{m_0}{m_{hh}^*(\mathbf{r})} = \gamma_1(\mathbf{r}) - 2\gamma_2(\mathbf{r}), \text{ and} \quad (2.7b)$$

$$\frac{m_0}{m_{lh}^*(\mathbf{r})} = \gamma_1(\mathbf{r}) + 2\gamma_2(\mathbf{r}). \quad (2.7c)$$

where $E_g(\mathbf{r})$ is the band gap of the material, $F(\mathbf{r})$ is the Kane parameter, $E_p(\mathbf{r})$ is related to the electron momentum, $\Delta_{SO}(\mathbf{r})$ is the spin-orbit coupling parameter, and the $\gamma(\mathbf{r})$ variables are the Luttinger parameters. The effective-mass tensor has zero off-diagonal terms [80] and, due to

strain, its diagonal has the form $\text{diag}\mathbf{M}=(m_{//}^*, m_{//}^*, m_{\perp}^*)$. The diagonal components of the electrons effective-mass tensor, as determined by time-independent perturbation theory [80], are given by

$$\frac{m_{\perp}^*(\mathbf{r})}{m_e^*(\mathbf{r})} = \frac{V_c(\mathbf{r}) - V_{lh}(\mathbf{r})}{E_g(\mathbf{r})}, \quad (2.8a)$$

and

$$\frac{m_{//}^*(\mathbf{r})}{m_e^*(\mathbf{r})} = \frac{[V_c(\mathbf{r}) - V_{hh}(\mathbf{r})][V_c(\mathbf{r}) - V_{lh}(\mathbf{r})]}{E_g(\mathbf{r})[V_c(\mathbf{r}) - 0.25V_{hh}(\mathbf{r}) - 0.75V_{lh}(\mathbf{r})]}, \quad (2.8b)$$

where $m_{\perp}^*(\mathbf{r})$ and $m_{//}^*(\mathbf{r})$ are the perpendicular and the in-plane effective masses of the electrons, respectively. The remaining components of the effective-mass tensor are zero. The Equations (2.8a) and (2.8b) will be used to compute the effective mass of electrons in strained $\text{In}_x\text{Ga}_{1-x}\text{As}$ that form the QD of InAs/GaAs. In the barrier region (GaAs) the effective masses are given by Equation (2.7) as will be shown in Section 3.1. For single InAs/GaAs QD almost all the low-lying confined states in the valence bands are dominated by its heavy-hole component but for coupled QDs the analysis of the band mixing becomes relevant [81].

The strain due to lattice mismatch has a strong effect on the electronic structure of semiconductors. The displacement of constituent atoms from their equilibrium positions changes the potential created by them and therefore the band structure is modified. When the split-off bands are taken into account, the band-edge energies at the Brillouin-zone center ($\mathbf{k} = 0$) for electrons, heavy-holes and light-holes bands of strained layers can be computed, respectively, by [78, 80]:

$$V_c(\mathbf{r}) = E_g(\mathbf{r}) + a_c(\mathbf{r})\varepsilon_h(\mathbf{r}), \quad (2.9a)$$

$$V_{hh}(\mathbf{r}) = a_v(\mathbf{r})\varepsilon_h(\mathbf{r}) + \frac{1}{2}b(\mathbf{r})\varepsilon_b(\mathbf{r}), \quad (2.9b)$$

and

$$V_{lh}(\mathbf{r}) = a_v(\mathbf{r})\varepsilon_h(\mathbf{r}) - \frac{1}{2} \left[\frac{b(\mathbf{r})\varepsilon_b(\mathbf{r})}{2} + \Delta_{SO}(\mathbf{r}) - \sqrt{\left[\Delta_{SO}(\mathbf{r}) - \frac{b(\mathbf{r})\varepsilon_b(\mathbf{r})}{2} \right]^2 + 8 \left[\frac{b(\mathbf{r})\varepsilon_b(\mathbf{r})}{2} \right]^2} \right]. \quad (2.9c)$$

In Equations (2.9a)–(2.9c), $a_c(\mathbf{r})$, $a_v(\mathbf{r})$, and $b(\mathbf{r})$ are the deformation potentials and the hydrostatic strain that determines the position of the electron and hole levels and biaxial strain, whose main influence is on the splitting of the light- and heavy-hole states, are respectively defined as:

$$\varepsilon_h(\mathbf{r}) = \varepsilon_{xx}(\mathbf{r}) + \varepsilon_{yy}(\mathbf{r}) + \varepsilon_{zz}(\mathbf{r}), \quad (2.10a)$$

and

$$\varepsilon_b(\mathbf{r}) = \varepsilon_{xx}(\mathbf{r}) + \varepsilon_{yy}(\mathbf{r}) - 2\varepsilon_{zz}(\mathbf{r}). \quad (2.10b)$$

The temperature effect on the energy gap of a semiconductor material is computed using the empiric Varshni equation [76]:

$$E_g(T) = E_g^0 - \frac{AT^2}{T+B}, \quad (2.11)$$

where A and B are the Varshni parameters, E_g^0 is the value of the energy gap for theoretical absolute zero temperature. The values for all parameters cited in this chapter for several semiconductor compounds of family III-V are compiled in Appendix A. Those values were gathered from literature [76–78].

Ternary alloys in the form E_xF_{1-x} have parameter values derived from their corresponding binary compounds (E and F) through linear interpolation using the following expression:

$$T_{E_xF_{1-x}}(x) = xT_E + (1-x)T_F - x(1-x)W_{EF}, \quad (2.12)$$

where the bowing parameter W_{EF} accounts for the deviation from a linear interpolation between the two compounds E and F.

2.3 Photoluminescence

Photoluminescence (PL) spectroscopy is a commonly used technique to characterize optical response of various organic and inorganic materials such as insulators and semiconductors (including nanostructures: quantum well, quantum wires, and quantum dots) [82, 83]. Figure 2.2 shows the common elements of a set up for photoluminescence spectroscopy. By probing the QD sample with a laser whose photon energy exceeds the fundamental transition energy of the heterostructure or above the barriers, electrons are excited to high energy levels generating electrons in the conduction band and holes in the valence band. Then, the electrons and holes recombine (radiative transitions) emitting photons [84]. The light emitted from the QD sample is then collected and passed through a monochromator, which selects a wavelength to transmit to a detector (D). The focal length of the monochromator determines the resolution of the system and the grating spacing sets the wavelength detection range. For example, a simple monochromator with focal length of 0.22 m and grating of 1200 groove/mm covers the visible to the near infrared wavelength range with an energy resolution of approximately 1 meV [85]. The signal is then sent to a

computer controlling the monochromator, scanning through a range of wavelengths, and recording the detector's voltage output corresponding to the wavelength. The data is then plotted, producing the sample output spectrum.

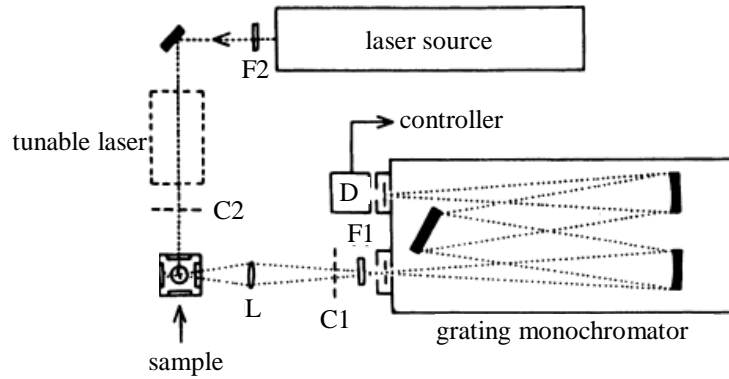


FIGURE 2.2 – PL arrangement, with laser, sample and cryostat, monochromator, and detector (D). Lens (L) focuses the PL signal; filters F1 and F2 block unwanted laser light; choppers C1 and C2 modulate the intensity of a light beam. Adapted from [85].

Figure 2.3 shows a schematic representation of a QD band structure. The electron in the conduction band and the hole in the valence band are attracted to each other by the electrostatic Coulomb force and form an exciton. The exciton binding energy is represented by the E_X parameter in Figure 2.3. Therefore, at low temperature, the energy of the optical transition associated to a peak in the PL spectrum can be computed by the following expression [86]:

$$e_n hh_m = e_n + E_g + hh_m - E_X, \quad (2.13)$$

where e_n is the energy of a confined electron state, hh_m is the energy of a confined hole state, and E_X is the binding energy of the exciton.

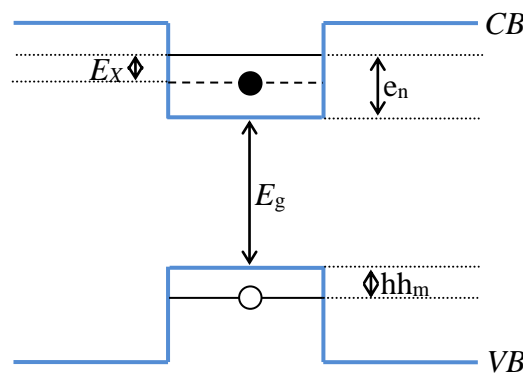


FIGURE 2.3 – Schematic electronic band structure of a QD. VB and CB stand for valence and conduction bands, respectively.

2.4 Numerical methods

In this monograph, it is assumed that QDs have cylindrical symmetry with the axial coordinate z parallel to the growth direction. This symmetry allows one to write the wave function as a product of two functions:

$$\Psi(\mathbf{r}) = \psi_1(r, z)\psi_2(\varphi), \quad (2.14)$$

which enables the separation of the azimuthal component (φ) from the other two variables. Then, the eigenstates in the nanostructure can be obtained from the following equations:

$$-\frac{\partial^2 \psi_2(\varphi)}{\partial \varphi^2} = m_q^2 \psi_2(\varphi), \quad (2.15a)$$

$$\left[\frac{-\hbar^2}{2} \nabla \mathbf{M}(r, z) \nabla + V(r, z) - E \right] \psi_1(r, z) = \frac{-\hbar^2}{2} \frac{\mathbf{M}(r, z)}{r^2} m_q^2 \psi_1(r, z). \quad (2.15b)$$

The first equation (2.15a) has a general solution of the form $\psi_2(\varphi) = \varphi_0 e^{im_q \varphi}$, where m_q is the azimuthal quantum number and assumes integer values. The second equation (2.15b) is the two-dimensional Schrödinger equation, which is solved numerically. Two numerical methods were implemented in this work to solve the Schrödinger equation for comparison and validation purpose. The first one is the Finite Element Method. This method is the main technique used in this thesis due to its flexibility. Together with a mesh generator, it is possible to solve the Schrödinger equation in any geometry with no change in the implemented code. The second method is based on a classical method in Physics to solve differential equations in which the unknown variable is expanded in terms of a linear combination of a certain set of orthogonal base functions [87]. This method will be referenced in this work as the Expansion Method and it is applied in the validation section.

2.4.1 Finite Element Method

The Figure 2.4 shows a geometrical model of a simple lens-shaped QD. The left figure (a) shows the three-dimensional model of an enclosing cylinder in red color with the front removed and the lens-shaped QD in blue. The right figure (b) shows the two-dimensional axially symmetric model that generates the left figure (a) by rotation around z -axis. The dashed lines at the top and the bottom indicate that the figure was truncated in the vertical

direction with the aim to show the details near the QD region. The following boundary conditions are imposed:

$$\psi(\mathbf{r})|_{\Gamma_1} = \psi_s, \quad (2.16a)$$

$$\frac{\partial \psi(\mathbf{r})}{\partial n} \Big|_{\Gamma_2} = f_s. \quad (2.16b)$$

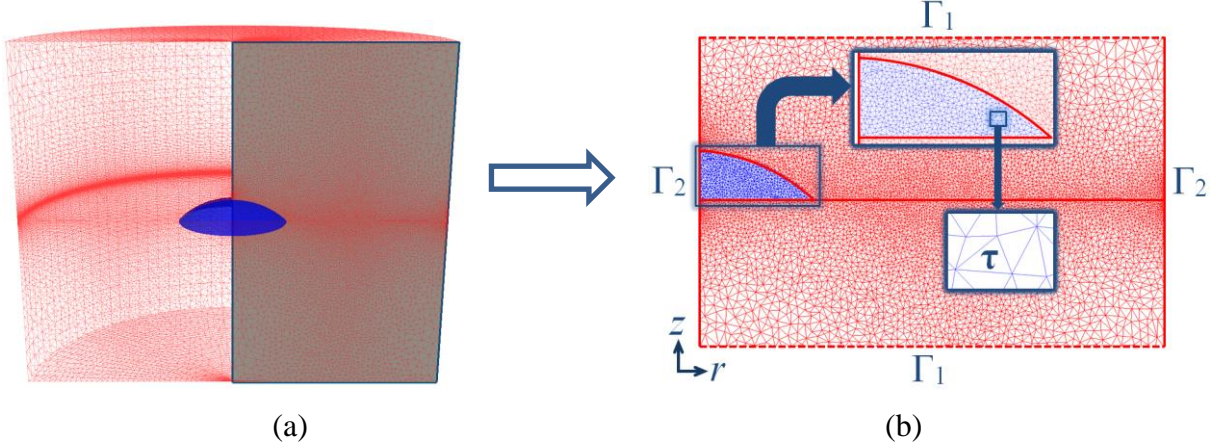


FIGURE 2.4 – (a) Three-dimensional model showing the lens-shaped QD in blue color and the front removed enclosing cylinder in red. (b) The axially symmetric QD model for our FEM implementation, showing the mesh close to the QD. The lines Γ_1 indicate where boundary condition of Dirichlet type is applied. The lines Γ_2 indicate where boundary condition of Neumann type are applied. The insets show details of the mesh inside the QD, as well as an element τ of the mesh.

In FEM, the problem domain (Ω) is divided into elements of simple geometry, each of which defines a subdomain Ω^τ . The nodal variables (dependent variables) and, when necessary, their derivatives are computed at each nodal point. In Lagrangian-type elements of the first order, the nodal point quantity and position coincide with the vertices of the finite element and the wave function is the only nodal variable. Hermitian-type elements have two nodal variables: the wave function and its derivative.

Inside each finite element, τ , the wave function is expanded in terms of a compact set (in a topological space) [88] of base functions, N_i :

$$\psi^\tau(\mathbf{r}) = \sum_{i=1}^{n_p} N_i^\tau \psi_i^\tau, \quad (2.17)$$

where n_p is the number of nodal points in the finite element and ψ_i^τ is the value of the wave function computed at each nodal point. The base function has the following properties on the nodal points:

$$N_i^\tau(\mathbf{r}_j) = \delta_{ij}, \quad (2.18)$$

where δ_{ij} is Kronecker's delta function. The base functions for a determined element τ are valid only in the limits of this element. This way, the solution for the entire domain is obtained by:

$$\psi(\mathbf{r}) = \sum_{\tau=1}^{n_e} \sum_{i=1}^{n_p} N_i^\tau \psi_i^\tau. \quad (2.19)$$

The Weighted Residual Method [89] was used to transform Equations (2.15b), (2.16a), and (2.16b) in the following integral equation:

$$\frac{\hbar^2}{2} \int_{\Omega} \nabla(P\mathbf{M}) \cdot \nabla \psi_1(r, z) d\Omega + \int_{\Omega} P(V - E) \psi_1(r, z) d\Omega + \frac{\hbar^2}{2} m_q^2 \int_{\Omega} P \frac{\mathbf{M}}{r^2} \psi_1(r, z) d\Omega = 0, \quad (2.20)$$

where P is an arbitrary weighting function. After the expansion of the wave function, Equation (2.17), the number of equations must be balanced with the number of unknown parameters. In this case, a number of weighting functions, equal to the number of nodal points times the number of unknown parameters, has to be chosen. To compute the values of these weighting functions, the Galerkin method is used, in which the weighting functions inside each element are chosen to be equal to the base functions used to describe the state variables ($P_j^\tau = N_j^\tau, j = 1, 2, \dots, n_p$) resulting in:

$$\begin{aligned} & \frac{\hbar^2}{2} \sum_{\tau=1}^{n_e} \sum_{i,j=1}^{n_p} \int_{\Omega^\tau} \nabla N_j^\tau \mathbf{M}^\tau \nabla N_i^\tau d\Omega^\tau \psi_i^\tau + V^\tau \sum_{\tau=1}^{n_e} \sum_{i,j=1}^{n_p} \int_{\Omega^\tau} N_j^\tau N_i^\tau d\Omega^\tau \psi_i^\tau \\ & + \frac{\hbar^2}{2} m_q^2 \sum_{\tau=1}^{n_e} \sum_{i,j=1}^{n_p} \int_{\Omega^\tau} N_j^\tau \frac{\mathbf{M}^\tau}{r^2} N_i^\tau d\Omega^\tau \psi_i^\tau = E \sum_{\tau=1}^{n_e} \sum_{i,j=1}^{n_p} \int_{\Omega^\tau} N_j^\tau N_i^\tau d\Omega^\tau \psi_i^\tau \end{aligned}, \quad (2.21)$$

where n_e is the total number of finite elements. Adopting the following notations T , $\{\mathbf{x}\}$, $\{\mathbf{x}\}^T$, and $[\mathbf{x}]$ to represent a transpose, a row vector, a column vector, and a matrix, respectively, Equation (2.21) can be written as:

$$\begin{aligned} & \frac{\hbar^2}{2} \sum_{\tau=1}^{n_e} \int_{\Omega^\tau} \nabla \{N^\tau\}^T [\mathbf{M}^\tau] \nabla \{N^\tau\} d\Omega^\tau \{\psi^\tau\}^T + V^\tau \sum_{\tau=1}^{n_e} \int_{\Omega^\tau} \{N^\tau\}^T \{N^\tau\} d\Omega^\tau \{\psi^\tau\}^T \\ & + \frac{\hbar^2}{2} m_q^2 \sum_{\tau=1}^{n_e} \int_{\Omega^\tau} \{N^\tau\}^T \frac{[\mathbf{M}^\tau]}{r^2} \{N^\tau\} d\Omega^\tau \{\psi^\tau\}^T = E \sum_{\tau=1}^{n_e} \int_{\Omega^\tau} \{N^\tau\}^T \{N^\tau\} d\Omega^\tau \{\psi^\tau\}^T \end{aligned}. \quad (2.22)$$

Therefore, the final matrix equation for the entire domain is given by:

$$(\mathbf{A} + \mathbf{B} + \mathbf{C})\{\psi^\tau\}^T = E\mathbf{D}\{\psi^\tau\}^T, \quad (2.23)$$

where

$$\begin{aligned} \mathbf{A} &= \frac{\hbar^2}{2} \sum_{\tau=1}^{n_e} \int_{\Omega^\tau} \nabla \{N^\tau\}^T [\mathbf{M}^\tau] \nabla \{N^\tau\} d\Omega^\tau, \\ \mathbf{B} &= V^\tau \sum_{\tau=1}^{n_e} \int_{\Omega^\tau} \{N^\tau\}^T \{N^\tau\} d\Omega^\tau, \\ \mathbf{C} &= \frac{\hbar^2}{2} m_q^2 \sum_{\tau=1}^{n_e} \int_{\Omega^\tau} \{N^\tau\}^T \frac{[\mathbf{M}^\tau]}{r^2} \{N^\tau\} d\Omega^\tau, \text{ and} \\ \mathbf{D} &= \sum_{\tau=1}^{n_e} \int_{\Omega^\tau} \{N^\tau\}^T \{N^\tau\} d\Omega^\tau. \end{aligned}$$

2.4.2 Expansion Method

The numerical formulation for the Expansion Method used in this work is the same as the one presented by Maia *et al.* [90] for lens-shaped QDs. Figure 2.4 shows a geometrical model of a simple lens-shaped QD with indications of the variables that are used in the mathematical formulation of the Expansion Method. The boundary conditions are the same shown for Finite Element formulation.

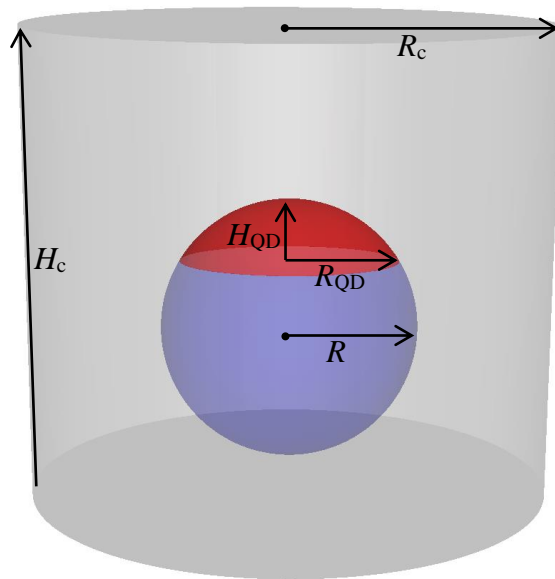


FIGURE 2.5 – Model of a lens-shaped QD (spherical cap from a sphere of radius R) with a radius R_{QD} and height H_{QD} inside a large cylinder of radius R_c and height H_c .

Assuming cylindrical symmetry and given a complete set of orthonormal base functions $\phi_{ln}(r, z)$ one can expand any function of $\psi_1(r, z)$ in terms of this complete orthonormal set:

$$\psi_1(r, z) = \sum_{l=1}^{l_{\max}} \sum_{n=1}^{n_{\max}} a_{ln} \phi_{ln}(r, z), \quad (2.24)$$

and a_{ln} are the coefficients of the expansion. The orthonormal functions $\phi_{ln}(r, z)$ are the large cylinder eigenstates:

$$\phi_{ln}(r, z) = \beta_{m_q n} J_{m_q} \left(k_{m_q n} r \right) \sin \left[l \pi \left(\frac{1}{2} - \frac{z}{H_c} \right) \right], \quad (2.25)$$

where l and n are the quantity of bases used to describe the wave function in z - and r -direction, respectively. H_c is the height of the large cylinder containing the substrate material, $J_{m_q} \left(k_{m_q n} r \right)$ is the Bessel function of the first kind of integral order m_q . To satisfy the boundary condition on the cylinder surface, $k_{m_q n}$ is given by $k_{m_q n} = \frac{x_{m_q n}}{R_c}$ where $x_{m_q n}$ is the n -th root of Bessel function of order m_q . The normalization factor $\beta_{m_q n}$ is given by:

$$\beta_{m_q n} = \sqrt{\frac{2}{H_c R_c^2 \pi J_{m_q+1}^2 \left(k_{m_q n} R_c \right)}}, \quad (2.26)$$

where R_c is the radius of the large cylinder.

Hence, the Schrödinger Equation (2.15b) can be written as:

$$\hat{H} \sum_{l=1}^{l_{\max}} \sum_{n=1}^{n_{\max}} a_{ln} \phi_{ln}(r, z) = E \sum_{l=1}^{l_{\max}} \sum_{n=1}^{n_{\max}} a_{ln} \phi_{ln}(r, z). \quad (2.27)$$

Multiplying Equation (2.27) by $\phi_{l'n'}^*(r, z)$, integrating over the spatial domain, and using the orthonormality condition $\left(\int_{\Omega} \phi_{l'n'}^*(r, z) \phi_{ln}(r, z) dr dz = \delta_{l'n'ln} \right)$ we get:

$$\sum_{l=1, l'=1}^{l_{\max}} \sum_{n=1, n'=1}^{n_{\max}} a_{ln} \int_{\Omega} \phi_{l'n'}^*(r, z) \hat{H} \phi_{ln}(r, z) dr dz = E \sum_{l=1, l'=1}^{l_{\max}} \sum_{n=1, n'=1}^{n_{\max}} a_{ln} \delta_{l'n'ln}, \quad (2.28)$$

where $\delta_{n'n}$ is the Kronecker delta function and is equal to 1 if $n' = n$ or $l' = l$ and 0, otherwise.

Assuming a shorthand notation for the matrix element

$\int_{\Omega} \phi_{l'n'}^*(r, z) \hat{H} \phi_{ln}(r, z) dr dz = H_{l'n', ln}$ one could write Equation (2.28) in matrix format as

$$\mathbf{H}\mathbf{A} = E\mathbf{A} , \quad (2.29)$$

where

$$\mathbf{H} = \begin{bmatrix} H_{11,11} & H_{11,12} & \cdots & H_{11,l_{\max}n_{\max}} & H_{11,21} & \cdots & H_{11,l_{\max}n_{\max}} \\ H_{12,11} & H_{12,12} & \cdots & H_{12,l_{\max}n_{\max}} & H_{12,21} & \cdots & H_{12,l_{\max}n_{\max}} \\ H_{13,11} & H_{13,12} & \cdots & H_{13,l_{\max}n_{\max}} & H_{13,21} & \cdots & H_{13,l_{\max}n_{\max}} \\ \vdots & \vdots & & \vdots & \vdots & & \vdots \\ H_{21,11} & H_{21,12} & \cdots & H_{21,l_{\max}n_{\max}} & H_{21,21} & \cdots & H_{21,l_{\max}n_{\max}} \\ \vdots & \vdots & & \vdots & \vdots & & \vdots \\ H_{l_{\max}n_{\max},11} & H_{l_{\max}n_{\max},12} & \cdots & H_{l_{\max}n_{\max},l_{\max}n_{\max}} & H_{l_{\max}n_{\max},21} & \cdots & H_{l_{\max}n_{\max},l_{\max}n_{\max}} \end{bmatrix} \quad (2.30)$$

and

$$\mathbf{A} = \begin{bmatrix} a_{11} \\ a_{12} \\ \vdots \\ a_{1n_{\max}} \\ a_{21} \\ \vdots \\ a_{l_{\max}n_{\max}} \end{bmatrix} . \quad (2.31)$$

After solving the Equation (2.29) one obtains the eigenvalues and eigenvectors of the system. The eigenvalues corresponds to the energies (E) of the confined states. The associated wave function for each state is computed substituting the corresponding eigenvector into Equation (2.24).

Defining $\theta_l(z) = \frac{1}{2} + \frac{l\pi z}{H_c}$ then $H_{l'n',ln}$ has the form:

$$\begin{aligned} H_{l'n',ln} = & \left\{ \left[\frac{l'\pi^2\hbar^2}{2H_c} \int_{\frac{-H_c}{2}}^{\frac{+H_c}{2}} \frac{\cos[\theta_{l'}(z)]\cos[\theta_l(z)]}{m_{\perp}^*(r,z)} dz + \int_{\frac{-H_c}{2}}^{\frac{+H_c}{2}} V(r,z) \sin[\theta_{l'}(z)] \sin[\theta_l(z)] dz \right] \times \right. \\ & \beta_{m_q n'} \beta_{m_q n} \int_0^{R_c} J_{m_q}(k_{m_q n'} r) J_{m_q}(k_{m_q n} r) r dr + \frac{\hbar^2}{4} \beta_{m_q n'} \beta_{m_q n} k_{m_q n'} k_{m_q n} \times \\ & \int_0^{R_c} [J_{m_q-1}(k_{m_q n'} r) J_{m_q-1}(k_{m_q n} r) + J_{m_q+1}(k_{m_q n'} r) J_{m_q+1}(k_{m_q n} r)] r dr \times \\ & \left. \int_{\frac{-H_c}{2}}^{\frac{+H_c}{2}} \frac{\sin[\theta_{l'}(z)] \sin[\theta_l(z)]}{m_{\parallel}^*(r,z)} dz \right\} \end{aligned} \quad (2.32)$$

Additional details about this formulation can be obtained in [90].

3 Methodology and implementation

In this thesis, we consider InAs QDs embedded in a GaAs matrix. This system of materials is one of the most widely used to build self-assembled QDs [22, 50, 51, 91–97]. To solve the problem in an axisymmetric model, the QD is enclosed inside a cylinder at the surface of which adequate boundary conditions are imposed to the wave functions. The position dependency of the effective mass tensor \mathbf{M} and the potential energy V inside the cylinder is established through the indium concentration $x = x(\mathbf{r})$. To take into account the non-homogeneous composition in the nanostructure, it is considered that $x = x(\mathbf{r})$ vary inside both the QD and WL regions allowing thus the simulation of any indium profile, while preserving the cylindrical symmetry. For the distribution of the material inside the QD and the WL, a grid with an adequate number of monolayers was created within the QD and the WL regions.

The first section of this chapter presents the values of relevant band structure parameters related to the binary compounds InAs, GaAs, and the ternary alloy $\text{In}_x\text{Ga}_{1-x}\text{As}$ used in this monograph. Section 3.2 gives an overview of the computational codes implemented to treat the phenomenon of segregation delineated in Chapter 1 as well as some results of tests, which validate the computational implementation of the equations and methods presented in Chapter 2. Section 3.3 presents the treatment for the WL, in which it is adopted the same approach presented by Maia *et al.* [90] based on the phenomenological model described by of Muraki *et al.* [98]. Section 3.4 presents the framework developed in this thesis to study the distribution of indium within self-assembled InAs/GaAs QDs.

3.1 InAs/GaAs material system

The electronic band parameters used for InAs and GaAs are listed in Appendix A. The conduction band offset generally adopted in literature and followed in this work is $\Delta E_c / \Delta E_g = 70\%$, which gives $\Delta E_c = 770$ meV between unstrained GaAs and InAs [76, 78]. Expressions (2.7a)-(2.7c) and (2.8a)-(2.8b) were used to define electron and holes effective masses. The electron and holes confinement potentials were computed using expressions (2.9a)-(2.9c) for the $\text{In}_x\text{Ga}_{1-x}\text{As}$ strained layers. The lattice constant of $\text{In}_x\text{Ga}_{1-x}\text{As}$ is larger than the one of GaAs and, consequently, the QD and WL are strained. In order to demonstrate

the effect of the strain in the electronic band profile, Figure 3.1 shows the conduction band and the valence bands edges, with and without the strain perturbation for a theoretical layer of $\text{In}_x\text{Ga}_{1-x}\text{As}$ strained on GaAs substrate. In this example, the indium composition (x) of $\text{In}_x\text{Ga}_{1-x}\text{As}$ layer increases linearly from 0% up to 100% in the growth direction. The strain raises the conduction band and breaks the degeneracy of the heavy-hole and the light-hole in the valence band. Moreover, the heavy-hole effective masses are also much heavier than the effective masses of light-holes meaning greater density of states. Therefore, in this case, the heavy-hole states tend to dominate the properties at the valence-band extremum.

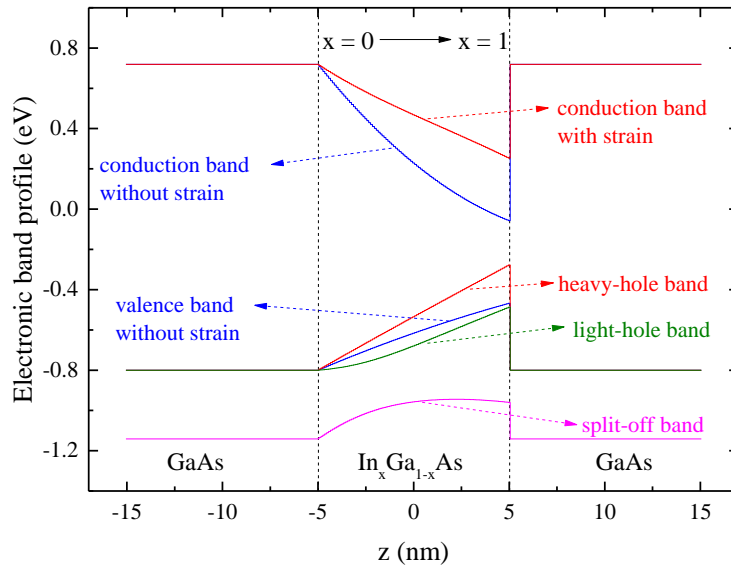


FIGURE 3.1 – Conduction and valence band profiles of a GaAs/ $\text{In}_x\text{Ga}_{1-x}\text{As}$ /GaAs heterostructure with and without taking into account lattice mismatch strain.

Analyzing Figure 3.1, it is worth noting the huge impact that strain has on the electronic structure of InAs/GaAs nanostructures. When strain is not taken into account, the energy gap of InAs layer is 0.4105 eV and with strain this value increases up to 0.5306 eV. An even greater change occurs in the conduction band edge, in which the depth of the potential well at the InAs/GaAs interface is 0.7762 eV when strain is disregarded in the calculation and decreases to 0.4660 eV when strain is considered.

Regarding effective mass anisotropy, the values of the electron effective-mass components, m_{\perp} and m_{\parallel} , for $\text{In}_x\text{Ga}_{1-x}\text{As}$ as a function of indium concentration (x) are shown in Figure 3.2. The m_{\perp} and m_{\parallel} values are computed accordingly to Equation (2.8). In Figure 3.2 we note that when $x = 0$ (pure GaAs) the material has isotropic effective mass for the electron, but it is anisotropic for any other concentration of indium.

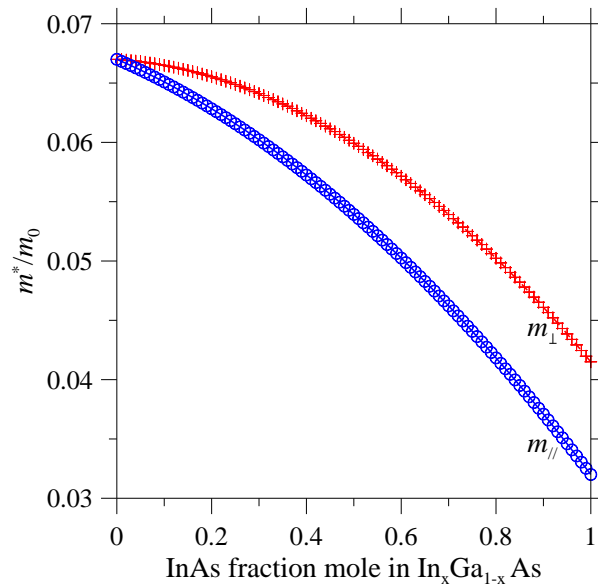


FIGURE 3.2 – Perpendicular and parallel components of electron effective mass for $\text{In}_x\text{Ga}_{1-x}\text{As}$ as a function of indium concentration, x .

3.2 Computational codes

This section presents an overview of the computational codes developed in this work. The computer codes developed in this thesis were designed not only to use but also to be integrated in a library of classes called *sdk-levsoft*. The *sdk-levsoft* library is coded in C++ language and was developed at the Laboratório de Engenharia Virtual of Instituto de Estudos Avançados. It has modules for manipulation of vectors, lists, sparse matrices, and iterative methods for sparse linear systems that permits the use of matrix preconditioning techniques, besides the finite element module. Figure 3.3 shows the modules that compose the *sdk-levsoft*. The white boxes indicate the modules that had classes included or modified in this thesis.

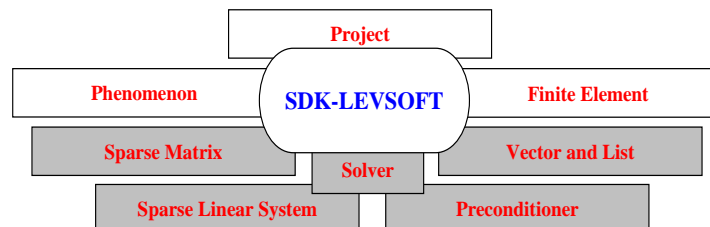


FIGURE 3.3 – General scheme of the *sdk-levsoft* library. The white boxes indicate the modules that had classes included or modified in this thesis.

Besides, a class named *CSemiconductorMaterial* was created that does not fit in any of those modules. It contains a parameter database with values commonly used in literature for several III-V binary compound semiconductors and computes the values of these parameters for ternary and quaternary alloys based on corresponding binary compound values. It also considers the temperature changing the parameters values accordingly.

In the finite element module, the Hermitian-type element was included. These finite elements ensure the BenDaniel-Duke continuity of $\frac{1}{m^*} \frac{\partial}{\partial n} \psi(\mathbf{r})$ at interface regions [99]. In addition, some methods regarding axial-symmetric integration were added to attend Equation (2.23). Figure 3.4 shows part of the classes that compose the finite element module. The white boxes indicate the classes that were developed or modified in this thesis.

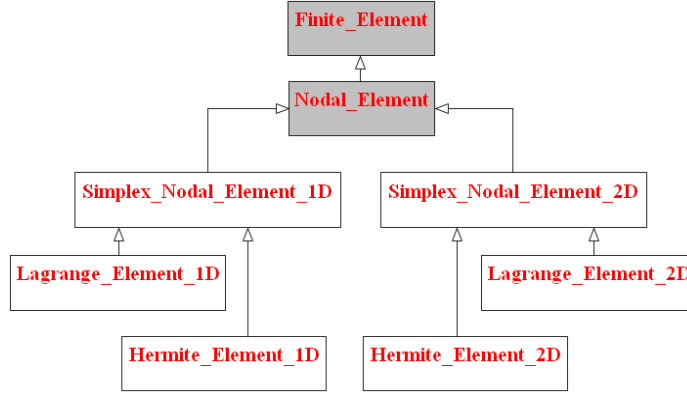


FIGURE 3.4 – Partial classes of the finite element module. The white boxes indicate the classes that were developed or modified in this thesis.

The FEM Integro-Differential Equation (2.23) was implemented in the phenomenon module of the *sdk-levsoft* in the class *CLev_Phen_Schrodinger* shown in Figure 3.5. The *CProject_Schrodinger* class derived from *CProject_Solver* centralizes the methods to read and write all the files in disk in this thesis. The classes *CLev_Phen_Schrodinger* and *CProject_Schrodinger* were implemented in [100] and they were originally designed to solve the Schrödinger equation in Cartesian coordinates. In this thesis, we extend these classes to solve the Schrödinger equation in cylindrical coordinates using the Finite Element Method which formulation was developed in Section 2.4.1. This implementation allows computing the electronic states of an axial symmetric QD and it takes into account the effective mass anisotropy of the electron in the conduction band.

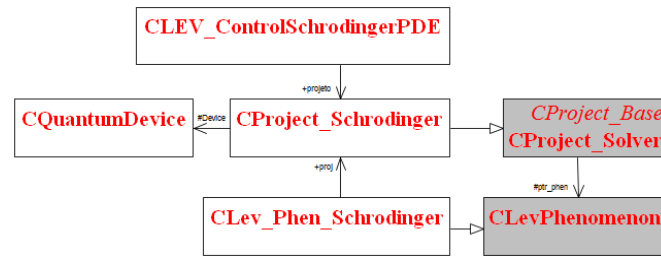


FIGURE 3.5 – Partial classes of the phenomenon and project modules. The white boxes indicate the classes that were developed or modified in this thesis.

The *CQuantumDevice* class stores the information of all the layers that compose the nanostructure. In *CQuantumDevice* there is a method that creates an object from the class *CSemiconductorMaterial* to obtain the materials properties. The *CSemiconductorMaterial* class computes, for example, the effective masses, Equation (2.8), and the potential energy, Equation (2.9), of all materials that compose the nanostructure.

Another set of classes were created to build automatically the FEM geometrical model of the QD nanostructure, shown in Figure 3.6. Currently, it has the capacity to build models of QD with shapes of cylinder, cone, and lens. The lens-shaped QD could be constructed either from a spherical cap or from a semi-ellipse. All these QD classes are derived from the *Nanostructure* class that also treats quantum wells and wetting layers. The *FEM_DOT* class manages the building of the geometrical model of the complete nanostructure, the finite element mesh generation, and the attribution of materials and boundary conditions. The *CLevDoc* class is the interface that connects this module with the *sdk-levsoft*.

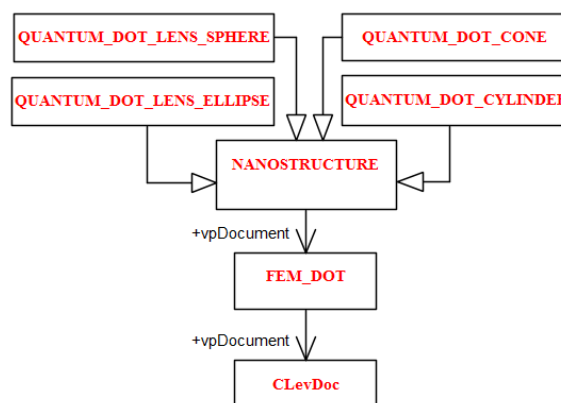


FIGURE 3.6 – Diagram of the classes that treat the automatic building of FEM model.

3.2.1 Convergence study of the finite element module

This section presents the results of the convergence tests performed on the implemented finite element computer code. The benchmark case that will be presented in this section is a standard problem in physics of a particle trapped in an infinite and spherically symmetric potential well. This problem allows the solution of the radial Schrödinger equation to be written in terms of standard functions.

The development of a semi-analytic solution of the Schrödinger equation for the infinite spherical potential well is presented in Appendix B. Table 3.1 shows the energy values of twenty states confined in an infinite spherical potential well with radius of 10 nm computed using the semi-analytic solution. The electronic state with principal quantum number n and azimuthal quantum number l is represented as z_l^n . The material of the sphere used in the computation is InAs, which has electron effective mass $m_e^*/m_0 = 0.023$. The effective mass anisotropy was not considered in these calculations.

TABLE 3.1 – Energy values obtained from the semi-analytical solution of an infinite spherical potential with radius of 10 nm, in eV. z_l^n represents the state with principal quantum number n and azimuthal quantum number l (see Appendix B).

z_l^n	$n = 1$	$n = 2$	$n = 3$	$n = 4$
$l = 0$	0.163498	0.653991	1.471479	2.615963
$l = 1$	0.334475	0.988638	1.969669	3.277669
$l = 2$	0.550273	1.370308	2.515594	3.987431
$l = 3$	0.808927	1.797658	3.108334	4.744588
$l = 4$	1.109150	2.269592	3.747039	5.548476

In general, a more refined mesh results in a more accurate solution, but at the expense of an increase in computation time. Hence, a compromise must be found in order to do not use neither a too sparse mesh that results in inaccurate solutions nor a too dense mesh that leads to a long time computations with no gain in accuracy. In order to study the convergence of FEM, several meshes were created for the axisymmetric spherical model, as shown in Figure 3.7. This figure presents the image of the mesh and the corresponding number of elements and density of elements (number of elements per domain area).

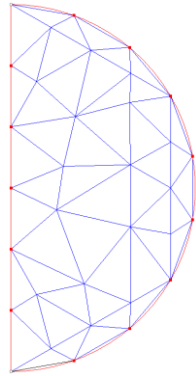
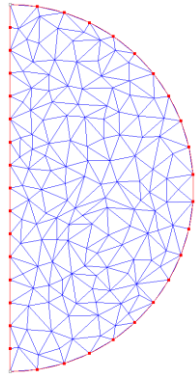
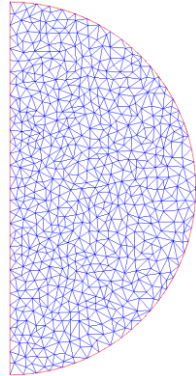
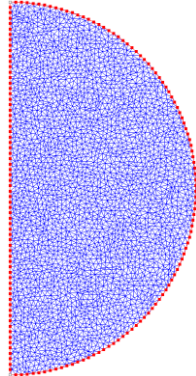
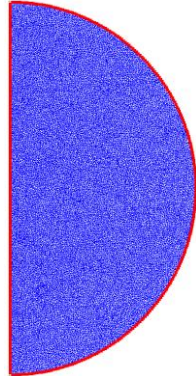
47 elements	297 elements	1262 elements	6214 elements	35095 elements
0.15 elem./nm ²	0.95 elem./nm ²	4.02 elem./nm ²	19.78 elem./nm ²	111.71 elem./nm ²
				
(a)	(b)	(c)	(d)	(e)

FIGURE 3.7 – Some meshes created to study the influence of the mesh refinement on the convergence of the calculations with FEM.

In this thesis, we are interested in states with the lowest energy values in relation to the conduction or valence band edge of the QD material. The convergence curves of the energy values as a function of the mesh density of the four states with lowest energy values are shown in Figures 3.8-3.11. These curves of convergence are for the Lagrangian-type elements of the first order, which is the simplest 2D finite element available. The ground state (z_0^1), Figure 3.8, presents the fastest convergence with the computed value of energy in good agreement with the semi-analytical value with a mesh density of 20 elem./nm². Similarly, good agreement is obtained with the states z_1^1 , z_2^1 , and z_0^2 . The convergence curves for the states z_1^1 , z_2^1 , and z_0^2 are shown in Figures 3.9-3.11. The absolute differences between the energy value computed with FEM with a mesh density of 20 elem./nm² and corresponding energy value computed with the semi-analytical method are 0.00013 eV, 0.00022 eV, and 0.00038 eV, respectively, for the states z_1^1 , z_2^1 , and z_0^2 .

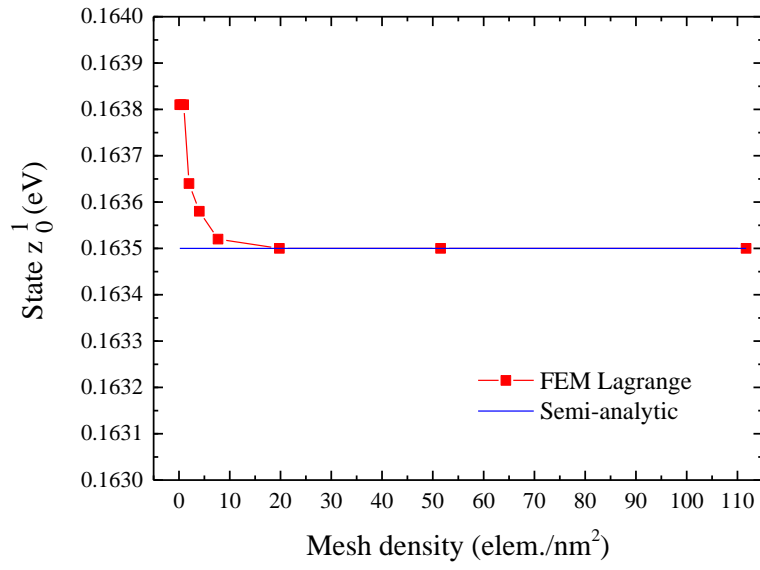


FIGURE 3.8 – Convergence of the ground state z_0^1 .

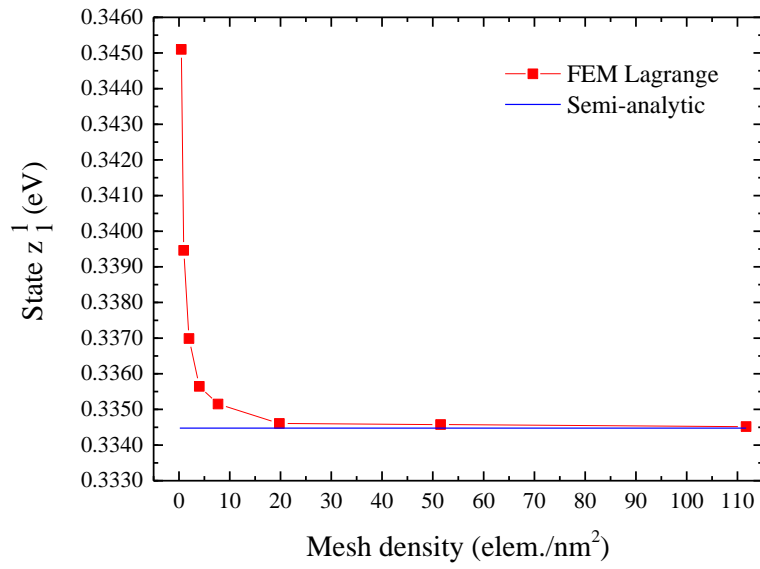


FIGURE 3.9 – Convergence of the ground state z_1^1 .

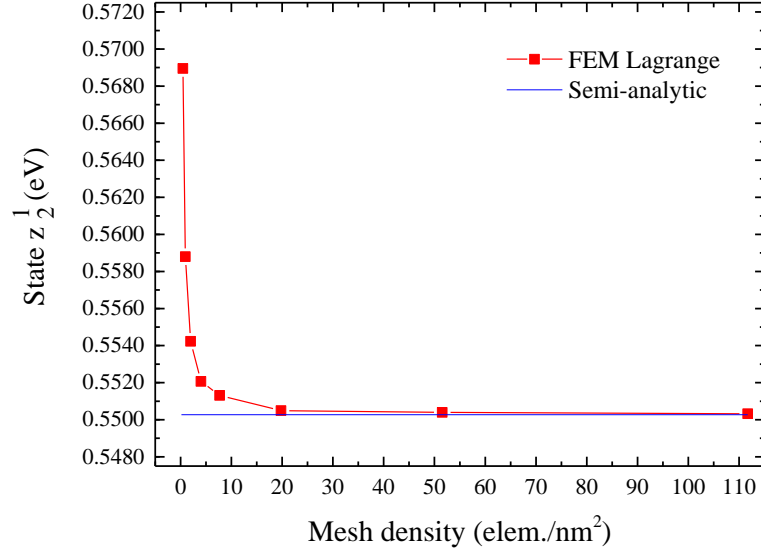


FIGURE 3.10 – Convergence of the ground state z_2^1 .

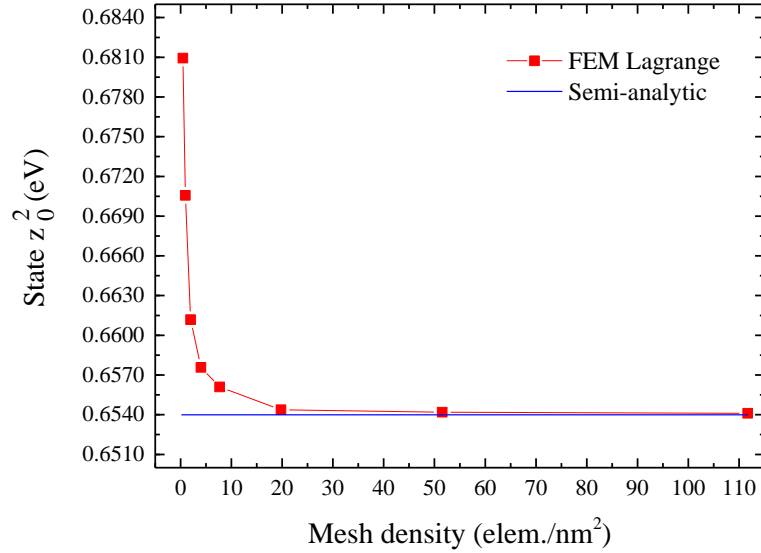


FIGURE 3.11 – Convergence of the ground state z_0^2 .

The convergence curves for higher energy states z_4^1 , z_0^4 , and z_4^4 are shown in Figures 3.12-3.14. The convergence of the state z_4^1 is shown in Figure 3.12. For a mesh density of 20 elem./nm², the difference between the value of the energy computed with the FEM and the semi-analytic model is 0.00254 eV (~0.23%). For the state z_0^4 , Figure 3.13, this difference is 0.01673 eV (~0.64%) for the same mesh density.

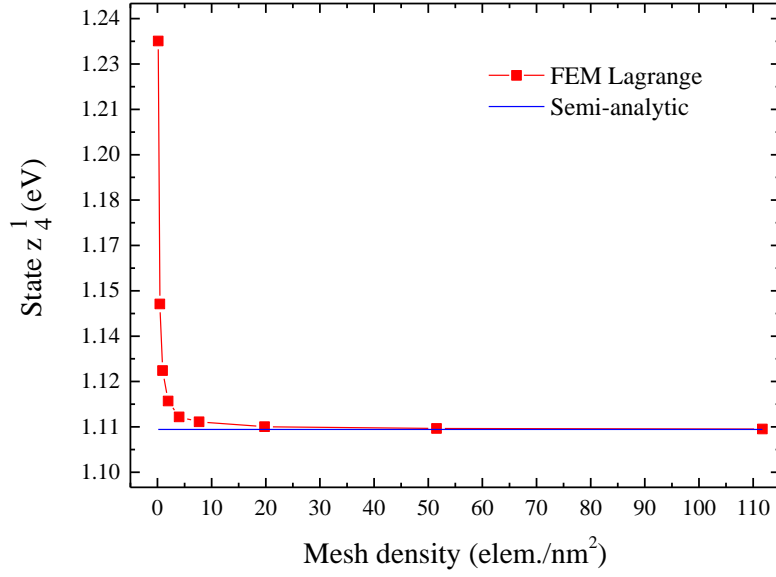


FIGURE 3.12 – Convergence of the state z_4^1 .

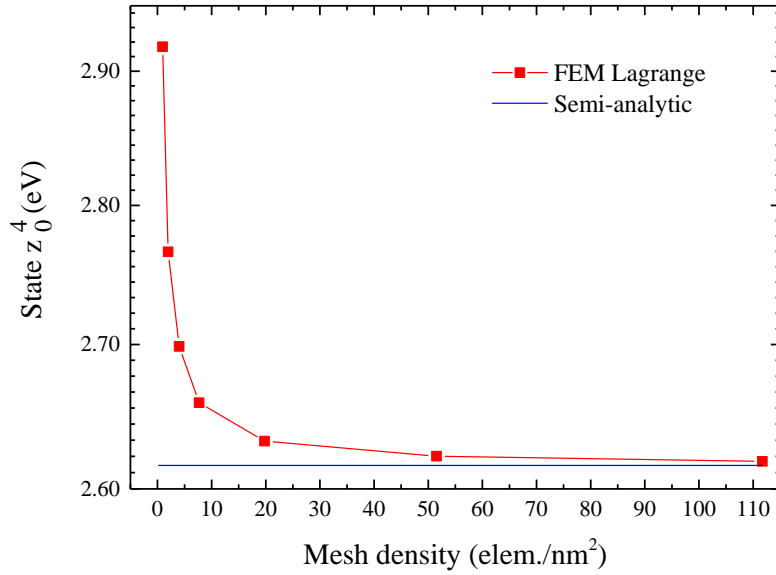


FIGURE 3.13 – Convergence of the state z_0^4 .

The convergence of the state z_4^4 is shown in Figure 3.14. The wave function of this state is the most complex one computed in these test series. The difference between the energy value computed with the FEM and the semi-analytic is 0.05615 eV ($\sim 1.01\%$) and 0.02130 eV ($\sim 0.38\%$) for a mesh density of 20 and 50 elem./nm², respectively. From these results, we fixed the standard mesh density in 20 elem./nm² which is sufficient to obtain good accuracy in energy values at least for the ground and the first excited states which are the states that we will be using most in our studies in this monograph. For QD models studied in this thesis, a nonuniform mesh is constructed (a mesh refined in the QD/WL-regions and

sparser in other regions). The mesh density of 20 elem./nm² is applied only in the interest regions of the QD and WL, where the elements have approximately the same area.

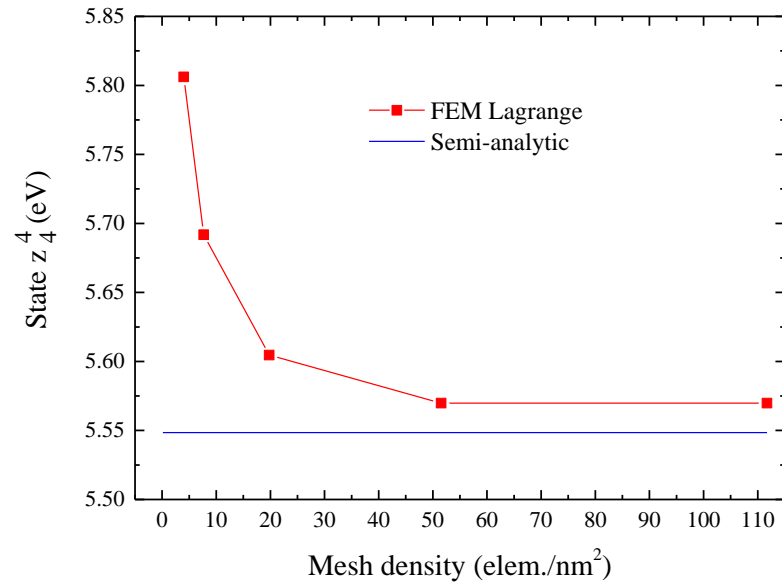


FIGURE 3.14 – Convergence of the state z_4^4 .

The graph of computation time of the FEM solver for the case of infinite spherical potential well as a function of the mesh density is shown in Figure 3.15. All the cases were executed in a computer equipped with a 64-bit Intel^(R) Core^(TM) i7 3.20 GHz processor and 24 GB of RAM.

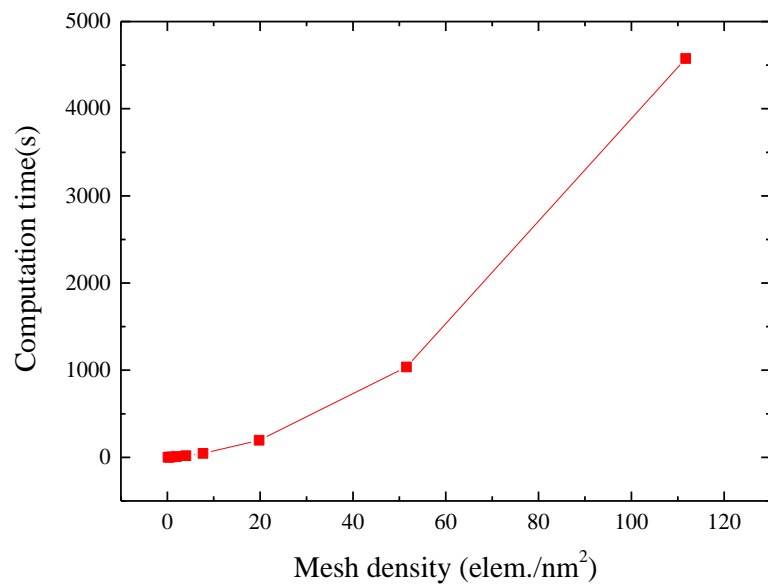


FIGURE 3.15 – Computation time as a function of the mesh density for the case of infinite spherical potential well.

For illustration purpose, Figure 3.16 presents the image of the probability density that was computed with FEM for the state z_0^1 .

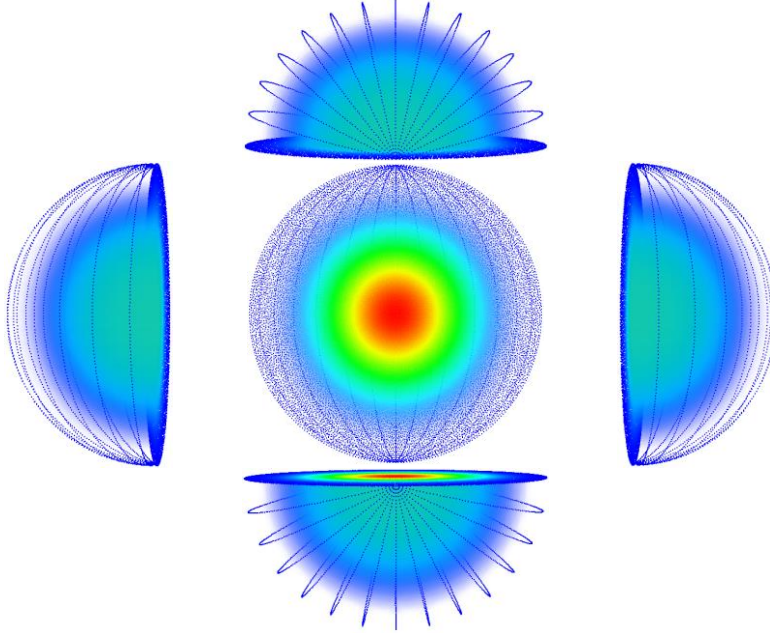


FIGURE 3.16 – Various views of the probability density computed with FEM for the state z_0^1 .

3.2.2 Validation of the finite element module with the Expansion Method

The use of the finite element module to solve the Schrödinger equation was also validated with results obtained from another method of resolution named, in this work, as Expansion Method (see Chapter 2, Section 2.4.2). The validation case used in this section reproduce the results presented by Maia *et al.* [90], which computed the energies of the ground state and first excited state of a lens-shaped QD as a function of its radius (R_{QD}) and height (H_{QD}). In this monograph, R_{QD} was varied in the range $4 \text{ nm} \leq R_{\text{QD}} \leq 20 \text{ nm}$ and H_{QD} was varied in the range $3 \text{ nm} \leq H_{\text{QD}} \leq 5 \text{ nm}$. These results are regarding homogeneous InAs QDs.

The parameters values of the Expansion Method used to compute the confined-states energies and wave functions are the same used in the cited article, which performed a convergence study of the Expansion Method and fixed the optimal values to obtain a compromise between computational time and precision. These values are $l_{\text{max}} = 70$, $n_{\text{max}} = 50$, and cylinder dimensions with $R_c = H_c = 80 \text{ nm}$.

The energy values for ground state and first excited state computed with both Expansion Method and FEM are shown in Figures 3.17 and 3.18, respectively. The energies values are presented relatively to the GaAs conduction band edge.

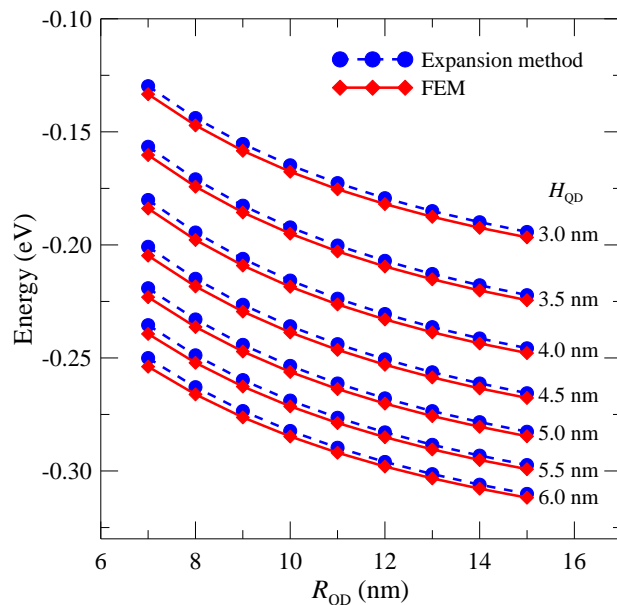


FIGURE 3.17 – Energies of the ground-state as a function of QD radius for different QD heights computed with the Expansion Method (dashed line) and FEM (continuous line).

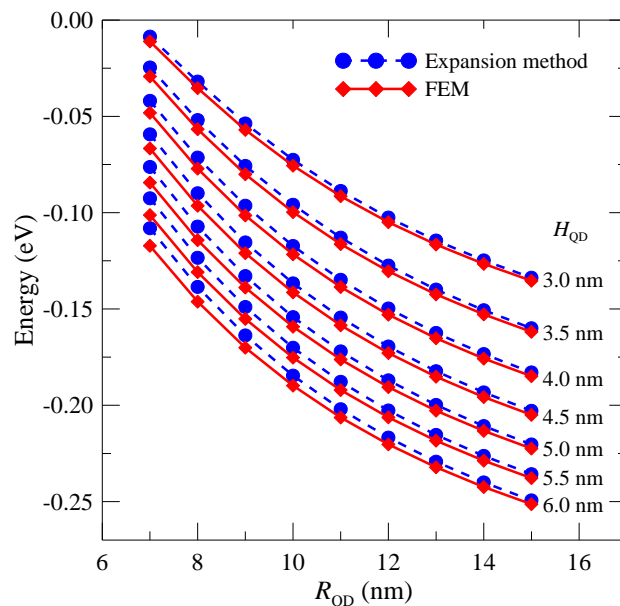


FIGURE 3.18 – Energies of the first excited state as a function of QD radius for different QD heights computed with the Expansion Method (dashed line) and FEM (continuous line).

The results obtained with FEM, implemented in this thesis, show a good agreement with the Expansion Method and reproduce the curves presented in [90]. The maximum

difference between the energy values computed by the FEM and the Expansion Method is less than 2.7% (~ 3 meV) for the ground state.

3.2.3 The finite element of Hermitian-type

The convergence with Hermitian-type finite elements was studied computing the energy values of the ground state and the first excited state in the conduction band of a lens-shaped QD with height of 4 nm and base radius of 12 nm. The convergence curves of the energies of these two states as a function of the mesh density are presented in Figures 3.19 and 3.20, respectively. The computational time to calculate these energies as a function of mesh density are presented in Figure 3.21. As a function of the mesh density, better results are obtained with the Hermitian finite elements than with the first order Lagrangian elements. The resolution with Hermitian finite elements converges with fewer elements than with Lagrangian finite elements. However, these calculations result in a considerable increase of computational resources (computation time and memory consumed). The more complex (in terms of quantity of operations) base functions allied to the increase in quantity of variables are the reasons for this behavior. Lagrangian finite elements have only one variable associated to the wave function, while Hermitian finite elements have six variables, one associated to the wave function, two associated to the radial and axial derivatives of the wave function, and three associated to the second derivatives of the wave function.

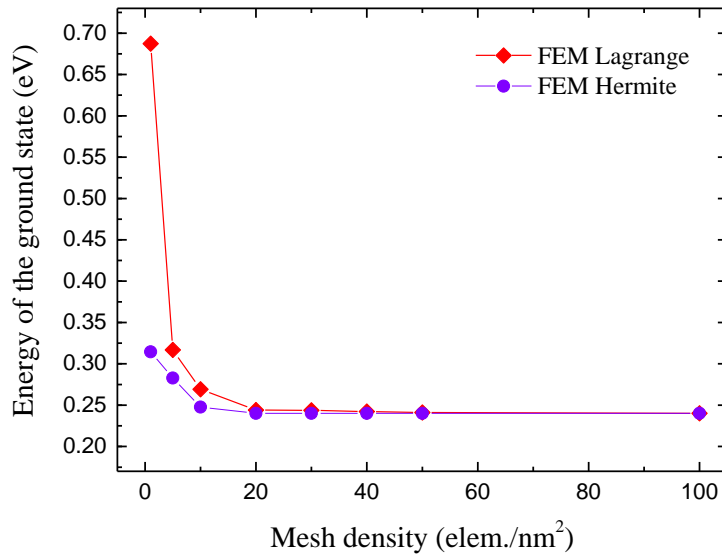


FIGURE 3.19 – Convergence curve of the ground state as a function of the density of elements using first order finite elements of Lagrangian-type (diamond) and Hermitian-type (circle).

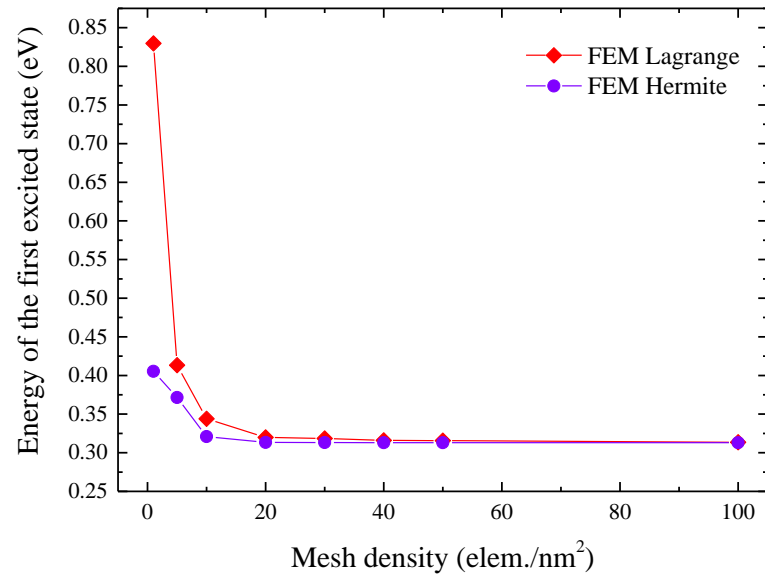


FIGURE 3.20 – Convergence curve of the first excited state as a function of the density of elements using first order finite elements of Lagrangian-type (diamond) and Hermitian-type (circle).

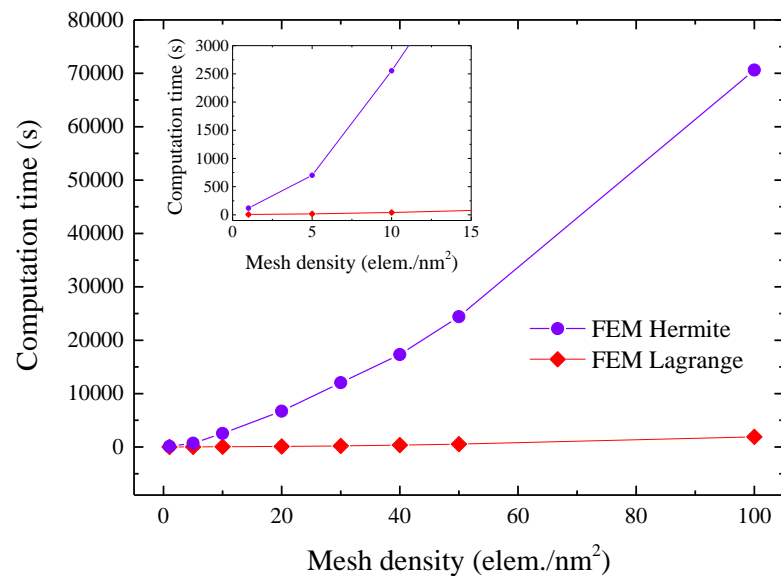


FIGURE 3.21 – Computational time to compute the energies of confined states as a function of the density of elements using first order finite elements of Lagrangian-type (diamond) and Hermitian-type (circle).

Despite de fact that the convergence obtained by using Hermitian-type finite elements, the time spent to achieve the solution with a mesh density of 10 elem./nm² is 22.4 times higher than the time spent to obtain good solutions by using Lagrangian-type finite elements with a mesh density of 20 elem./nm². The difference in computational time for these orders of mesh density is shown in the inset of Figure 3.21.

In order to execute such tests a 64-bit compiler was used because solving the equation system resulting from the Hermitian-type finite elements needs much more than 4GB of memory size, which is the limit of memory size that can be allocated by a 32-bit compiler. The computational times shown in this section were gathered in a Xi^(R) MTower^(TM) 2P64X Workstation equipped with two Intel^(R) Xeon^(R) CPU E5-2697 v3 2.60 GHz and 256 GB of memory size.

The Hermitian finite element is necessary only when it is strictly necessary to guarantee the BenDaniel-Duke continuity of derivatives of wave functions. In this thesis, it is required only the values of energies of confined states that are well computed by Lagrangian finite elements.

3.3 The wetting-layer

In this thesis, the WL is treated using the same approach presented by Maia *et al.* [90]. In that work, the WL is modeled as a one monolayer-thick InAs layer whose thickness and composition changes after capping by GaAs due to surface diffusion effect. Offermans *et al.* [101] studied the formation of InAs WLs by cross-sectional scanning tunneling microscopy and observed that surface diffusion of indium atoms in these layers was similar to the diffusion in QW nanostructures. This diffusion could be perfectly taken into account with the phenomenological model of Muraki *et al.* [98], which has been reported to model very well the segregation profile in InAs QWs by several papers in literature [102–104]. It computes the indium composition in the n -th monolayer of a QW by:

$$x_n = \begin{cases} x_0(1-R^n), & \text{if } 1 \leq n \leq Q \\ x_0(1-R^Q)R^{n-Q}, & \text{if } n > Q \end{cases}, \quad (3.1)$$

where x_0 and Q are the nominal indium composition and the well width in monolayers, respectively. The diffusion parameter R depends on the growing machine system besides

growing conditions. For the machine system used to grow the sample studied in this work it was computed that $R = 0.85$ for the standard growth conditions in that system [90, 105]. Hence, assuming that the nominal indium composition x_0 is 1, the indium concentration of the n -th monolayer of the WL is represented by the curve shown in Figure 3.22. The concentration of indium start at 0.15, quickly decreases to below 0.05 in the 10th monolayer, and is practically zero in 20th monolayer.

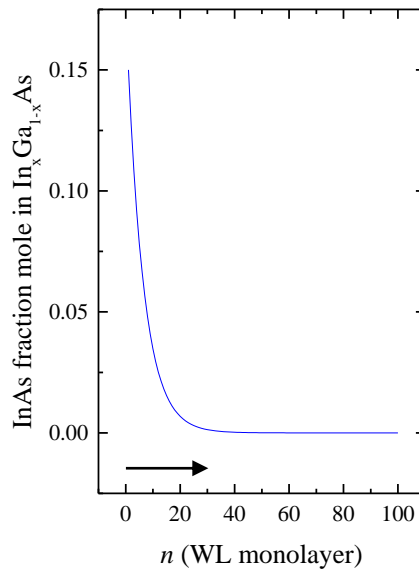


FIGURE 3.22 – Concentration of indium in the n -th monolayer of the WL. The arrow indicates the growth direction. Therefore, $n = 1$ indicates the lowest layer of the WL.

In order to test the effect of the WL in the calculated values of the confined states energies of a QD we considered models with and without the WL both shown in Figure 3.23. In this figure, the WL is represented up to the 20th monolayer. The material attribution (indium composition) in the nanostructure is shown in Figure 3.24, in which the WL is visible as a thin orange-color band.

The energy value of the ground state in conduction band and valence band for several QD height and base radius are presented in Figure 3.25. The curves with dashed line were computed without WL and the ones with continuous line were computed with WL. A similar graph with energy values of the first excited state is shown in Figure 3.26.

From Figures 3.25 and 3.26 we can observe that the energy values for both the ground state and the first excited state computed with the WL compared with the corresponding energy value computed without the WL are very similar with absolute difference ranging between 0.005 eV and 0.014 eV. Besides the computation time to solve a problem with the WL is almost twice the time needed to solve a similar case without the WL as shown in

Figure 3.27 that presents the computational time needed to solve each one of the case set with QD height of 3 nm. Hence, for this thesis, we will adopt the simplification of neglecting the WL since the focus will be on the computational procedure to study the nonuniform material composition of self-assembled QDs, which will be discussed in the next section.

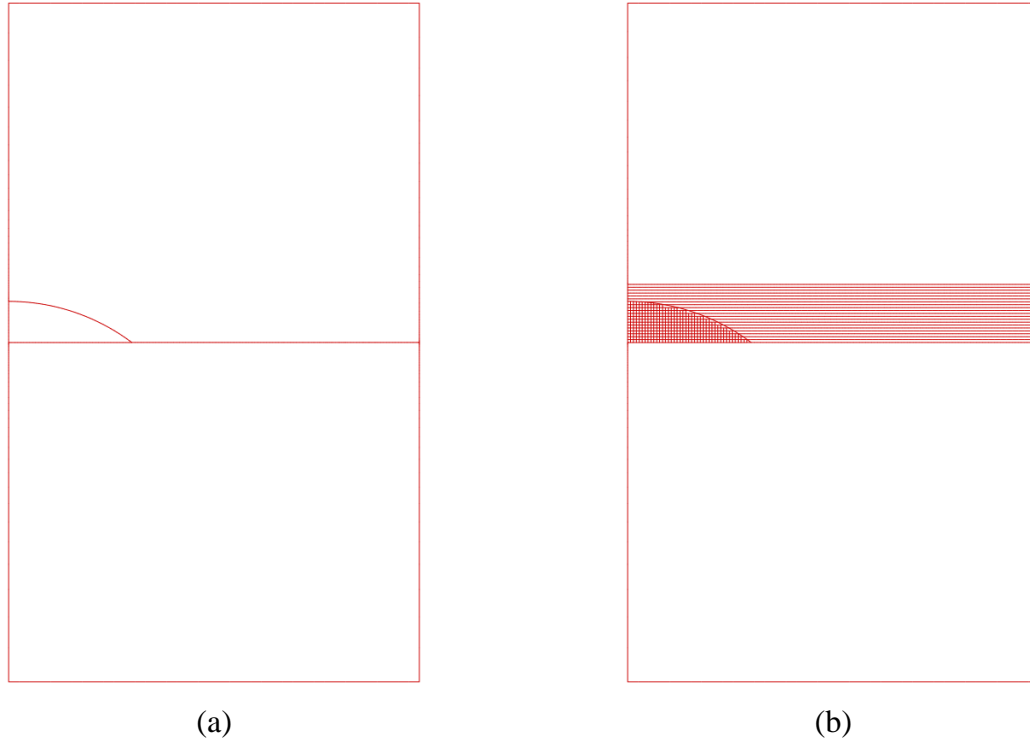


FIGURE 3.23 – FEM model of a lens-shaped QD (a) without WL and (b) with WL.

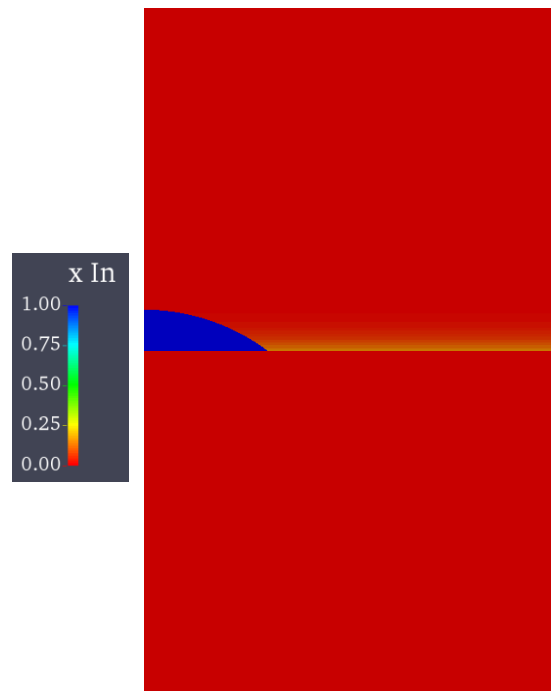


FIGURE 3.24 – Indium composition x ($\text{In}_x\text{Ga}_{1-x}\text{As}$).

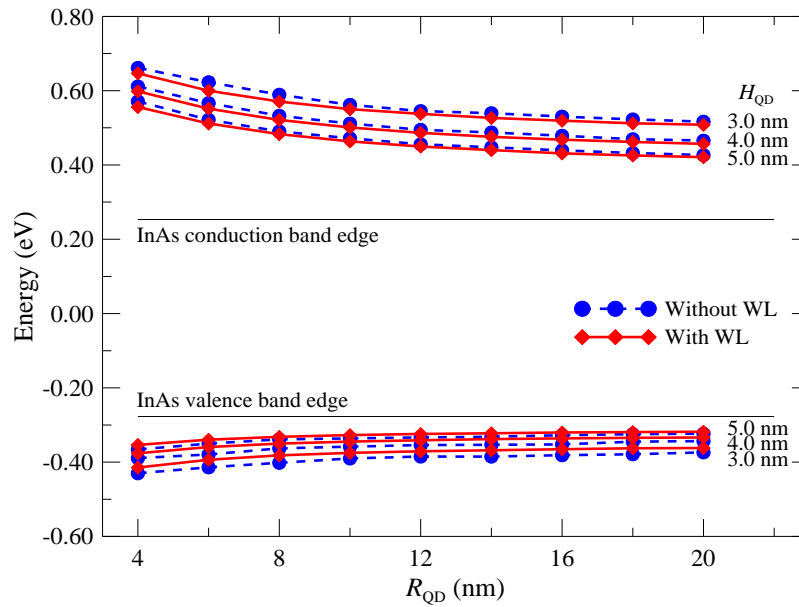


FIGURE 3.25 – Energy values of the ground state in the conduction band and the valence band for several pure InAs QDs with different heights and base radius. The dashed line curves were computed without WL and the continuous line with WL.

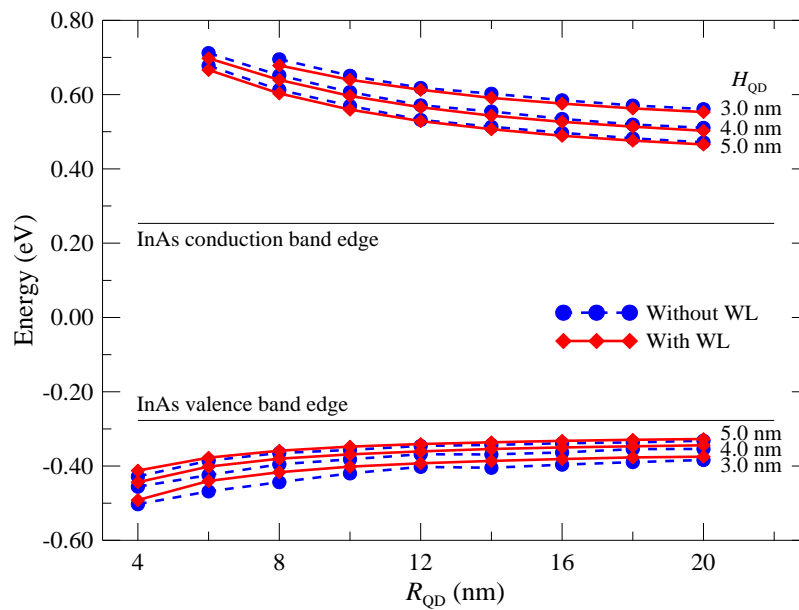


FIGURE 3.26 – Energy values of the first excited state in the conduction band and the valence band for several pure InAs QDs with different heights and base radius. The dashed line curves were computed without WL and the continuous line with WL.

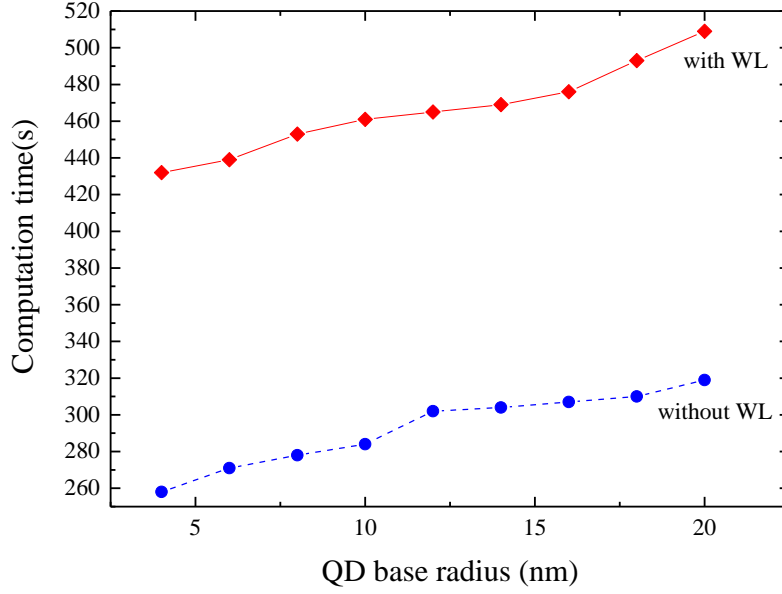


FIGURE 3.27 – Comparison of computation time between a case set calculated without the WL (dashed line) and calculated with the WL (continuous line). Case set with QD height of 3 nm.

3.4 Nonuniform indium distribution within QD

The intermixing between the film and the surrounding layers as well as the surface diffusion of indium atoms [98, 106, 107] are important to study self-assembled InAs/GaAs QDs because these phenomena modifies the nominal indium concentration, and consequently the electronic band structure of these nanostructures [62]. Moreover, the understanding of how indium atoms are distributed in the grown nanostructure is essential to obtain tailor-made optical properties in order to optimize the device performance. There are several experimental papers in literature aimed to study the nonuniform material composition of self-assembled QDs. However, due to the complex material distribution and the small spatial dimensions of QDs, there is not a consensus about either their real shape or how the indium atoms are distributed within these structures [67, 68, 108]. Only a small number of theoretical papers focuses on the material distribution, but there is no direct comparison with experimental data. In this thesis we explore two models of indium distribution, inspired in the results presented by Giddings *et al.* [68] and by Blokland *et al.* [67].

Giddings *et al.* [68] studied the composition of InAs/GaAs QDs samples through cross-sectional scanning tunneling microscopy and atom probe tomography and concluded that the core of the QD is indium rich, starting from 0% at the border and reaching 60% at the

center. We wrote a mathematical model for this distribution assuming a Gaussian distribution along the radial and vertical directions:

$$x(z) = X x_{\max} \exp\left[\frac{-(z - b_z)^2}{2\sigma_z^2}\right] + x_{\min}, \quad (3.2)$$

where $b_z = \alpha H_{\text{QD}}$ is the position of the center of the Gaussian function, $\sigma_z = \frac{1}{2}\gamma H_{\text{QD}}$ is the standard deviation, and x_{\max} (x_{\min}) is the maximum (minimum) concentration of dot material along the z direction. The parameter α defines the position of x_{\max} : a value of $\alpha = 1$ places the peak at the top of the QD, while $\alpha = 0.5$ shifts the peak position to the center of the QD. The second step consists of computing the concentration of the dot material at a point of coordinates (r, z) using the expression

$$x(r, z) = x(z) \exp\left[\frac{-r^2}{2\sigma_r^2}\right] + x_{\min}, \quad (3.3)$$

where $\sigma_r = \frac{1}{2}\beta r_{\text{QD}}(z)$. The function $r_{\text{QD}}(z)$ returns the effective value of the QD radius for a given height z and depends on the QD format. The parameter β is a factor that adjusts the width of the Gaussian function: a value of $\beta = 1$ restricts the width of the Gaussian curve to half of the QD radius; a value of $\beta = 2$ makes its width equal to the QD radius. The set $(\alpha = 0.5, \beta = 1, \gamma = 1, X = 0.6)$ allows to reproduce approximately the indium distribution proposed by Giddings et al. [68], Figure 3.28-a.

Blokland *et al.* [67] also studied the composition of self-assembled InAs QDs based on cross-sectional scanning tunneling microscopy and reported an indium composition that starts at 70% at the center of the base of the QDs and increases linearly to 100% at their top, while the indium concentration is only 25% at the base edge. The mathematical model of this distribution assumes that the value of $x(r, z)$ corresponding to the indium concentration at a position (r, z) inside a QD is a weighted arithmetic average of two indium concentrations calculated with a rule of three applied both to the radial coordinate r and to the axial coordinate z . Considering that the origin of the coordinate system is located at the center of the base of the QD, the equation for this indium profile is given by:

$$x(r, z) = \gamma \left[\left(X \cdot x_{z,\max} - x_{z,\min} \right) \frac{z}{H_{\text{QD}}} + x_{z,\min} \right] \frac{z}{H_{\text{QD}}} + \beta \left[\left(x_{r,\max} - x_{r,\min} \right) \frac{r}{R_{\text{QD}}} + x_{r,\min} \right] \frac{(R_{\text{QD}} - r)}{R_{\text{QD}}}, \quad (3.4)$$

$x_{r,\max}$, $x_{r,\min}$ and $x_{z,\max}$, $x_{z,\min}$ correspond to the maximum and minimum values of the indium concentration along the radial and vertical directions, respectively. The X parameter is used to change the value of the maximum of the indium concentration, while the γ and the β parameters have influence on the steepness of the indium distribution along the vertical and radial directions, respectively. The set ($\beta = 1$, $\gamma = 1$, $X = 1$) reproduces approximately the indium distribution proposed by Blokland, Figure 3.28-b.

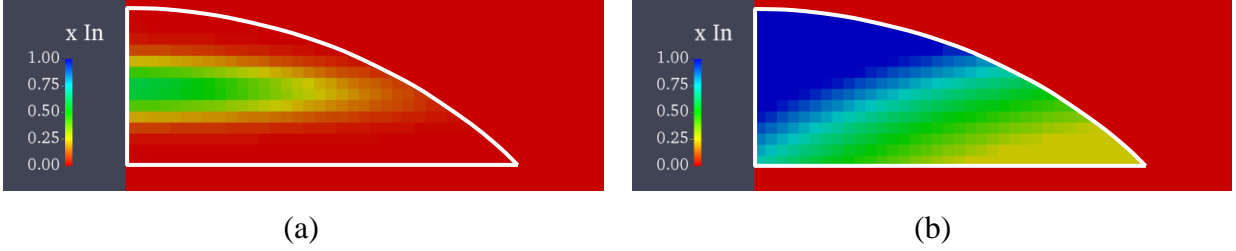


FIGURE 3.28 – Models of indium distribution within QDs: (a) Giddings, (b) Blokland.

The theoretical results obtained by us with these two models are presented in the next chapter. Considering the parameters presented in the previous paragraphs for each model, we could not reproduce the experimental PL spectrum of a reference QD sample.

In the next step, we mathematically modeled the problem in the form of an inverse problem in order to verify if there are sets of parameters (α , β , γ , X) for the Giddings distribution model or (β , γ , X) for the Blokland distribution model that allow to reproduce the experimental PL spectrum. The details are described in the following sections.

3.4.1 The inverse problem

Inverse problems can be described as problems where the response of the system is known but not the conditions that led to it [109]. As previously mentioned, self-assembled QDs have a non-homogeneous material composition that cannot be measured exactly because, in general, the very small volume of the QDs makes the signal of these measurements almost insensitive to the gradient of the indium composition inside these nanostructures [51–54]. The inverse problem approaches developed in this thesis aims to obtain a material composition profile inside a self-assembled QD sample that reproduces experimental photoluminescence (PL) transition energy peaks. Besides PL, additional experimental data, such as, high-resolution Transmission Electron Microscopy (TEM) and/or Scanning Tunneling Microscopy (STM) obtained from a QD sample can also contribute to solve the inverse problem. As we will see later, the image is not strictly necessary and aims to give a hint about the dimensions

of the QD. With these inputs, the solver of the inverse problem iteratively adjusts the concentration and distribution of material inside the QD until it finds a resulting electronic configuration that generates PL peaks that matches the measured ones. Table 3.1 shows the physical system, the governing physics, and the physical quantity that we are interested in this thesis, and what we actually consider to formulate the inverse problem.

TABLE 3.1 – Components of the inverse problem.

Physical system	Governing equations	Physical quantity	Observed data
QD material composition profile	Schrödinger equation, classical elasticity equation	Energy	PL peaks

In order to solve the inverse problem, metaheuristics are employed. Metaheuristics are a general set of stochastic procedures, often nature-inspired, designed to obtain approximate solutions of complex optimization problems [110–112]. In general, several runs of a given metaheuristics are executed in order to take into account the randomness of the stochastic procedure. The strategy adopted in this work involves the use of three different metaheuristics, each one with a certain number of runs. The three metaheuristics are: particle swarm optimization (PSO) [113, 114], black hole optimization (BH) [115], and genetic algorithm (GA) [116, 117].

An inverse problem can be formulated as a minimization (or maximization) problem. An objective function (O_F) represents a goal to be achieved and a set of constraining relations can be used to impose additional conditions associated to the specific problem. Therefore, a good approximate solution is the one that minimizes (or maximizes) the objective function subjected to specific constraints.

Two inverse problems are considered in this document. The first approach makes use of data from the experimental PL energy peaks and an estimative of the QD size based on a high-resolution image. In this case, the objective function, O_F , is written as:

$$O_F = \sum_{i=1}^n \left| P_i - (P_i^{exp} + E_X) \right| + \sum_{i=2}^n \left| P_i - P_{i-1} - \Delta_{i,i-1}^{exp} \right|, \quad (3.5)$$

where P_i and P_i^{exp} are the energy values of the i -th computed and experimental PL peaks, respectively, E_X is the exciton binding energy, and $\Delta_{i,i-1}^{exp}$ is the difference in energy between the i -th and $(i-1)$ -th experimental peaks. We applied this formulation to study an InAs/GaAs

QD sample, obtaining insights about the distribution of material within the nanostructure. These results were published in [70], and a summary is presented in the results section. In order to obtain coherent results, this approach needs the approximate dimensions of the QD as input parameters because there is not a mechanism to drive the system in the direction of a distribution with an indium-rich core as observed in high-resolution TEM images of QD sample.

A second approach was explored which includes the value of the elastic potential energy U , due to the lattice parameter misfit inside the QD (Chapter 2, Section 2.1), in the objective function. The minimum value of the elastic potential energy is unknown and it is certainly not zero. In order to take into account this uncertainty, the objective function was changed to the form presented in Equation (3.6).

$$O_F = d(P_i)U. \quad (3.6)$$

The penalty function d is related to the photoluminescence and is given by:

$$d(P_i) = \begin{cases} \exp\left(\sigma \sum_{i=1}^n \Delta P_i\right) + 1 - \exp(\sigma \varepsilon), & \text{if } \sum_{i=1}^n \Delta P_i > \varepsilon \\ 1, & \text{if } \sum_{i=1}^n \Delta P_i \leq \varepsilon \end{cases}, \quad (3.7)$$

where $\Delta P_i = \left| P_i - (P_i^{\text{exp}} + E_X) \right|$ and ε is associated to the experimental error. The variable σ is a parameter to adjust the sensitivity of the objective function to variations in ΔP_i . We set this parameter value to three after some rough analysis.

In order to compute the energy values of the PL peaks, the material distribution within the QD has to be defined. Both models presented in the previous section were used with different values of the parameters set $(\sigma, \beta, \gamma, X)$. The basic idea is to find the set that minimizes O_F . Once defined the indium distribution, we compute the corresponding anisotropic effective masses and potentials [Equations (2.8) and (2.9)] and solve the Schrödinger equation using FEM [Equation (2.23)] for both the conduction and valence bands. The final step is the computation of the photoluminescence peaks transition energies [Equation (2.13)]. Along the process, the metaheuristics guide the choice of the sets of parameters, trying to minimize O_F .

As mentioned previously, three different metaheuristics were employed to solve Equations (3.5) and (3.6). All of them are implemented in an optimization library here named *Optimization Framework* used in this thesis. The *Optimization Framework* was developed at

the Virtual Engineering Laboratory (LEV: Laboratório de Engenharia Virtual) in the Instituto de Estudos Avançados/DCTA. For each metaheuristic, we execute five runs.

3.4.2 Software implementation

The flowchart of the inverse problem algorithm developed in this work is shown in Figure 3.29. The flowchart has three boxes: metaheuristic framework, FEM solver, and objective function. The metaheuristic framework implements several metaheuristics. A configuration file allows to define the metaheuristics chosen to accomplish a given study as well as the control parameters of the metaheuristics and the parameters of the problem which have to be found. In this work, we use three metaheuristics already implemented in the framework. The difference among the metaheuristics is in the procedure that they adopt to update the new set of values of the unknown parameters (σ , β , γ , X). The update mechanisms of these metaheuristics are out of the scope of this work and hence they will not be discussed here. For those who are interested, additional information on each metaheuristic can be found in [113–117]. The Boxes “FEM solver” and “objective function” include the computer codes that were described in previous sections (Sections 3.2 and 3.4.1, respectively) of this chapter.

For the stopping criteria it was used the maximum number of iterations, set in 1,000 and the maximum number of consecutive iterations for which the objective function does not change, set in 100.

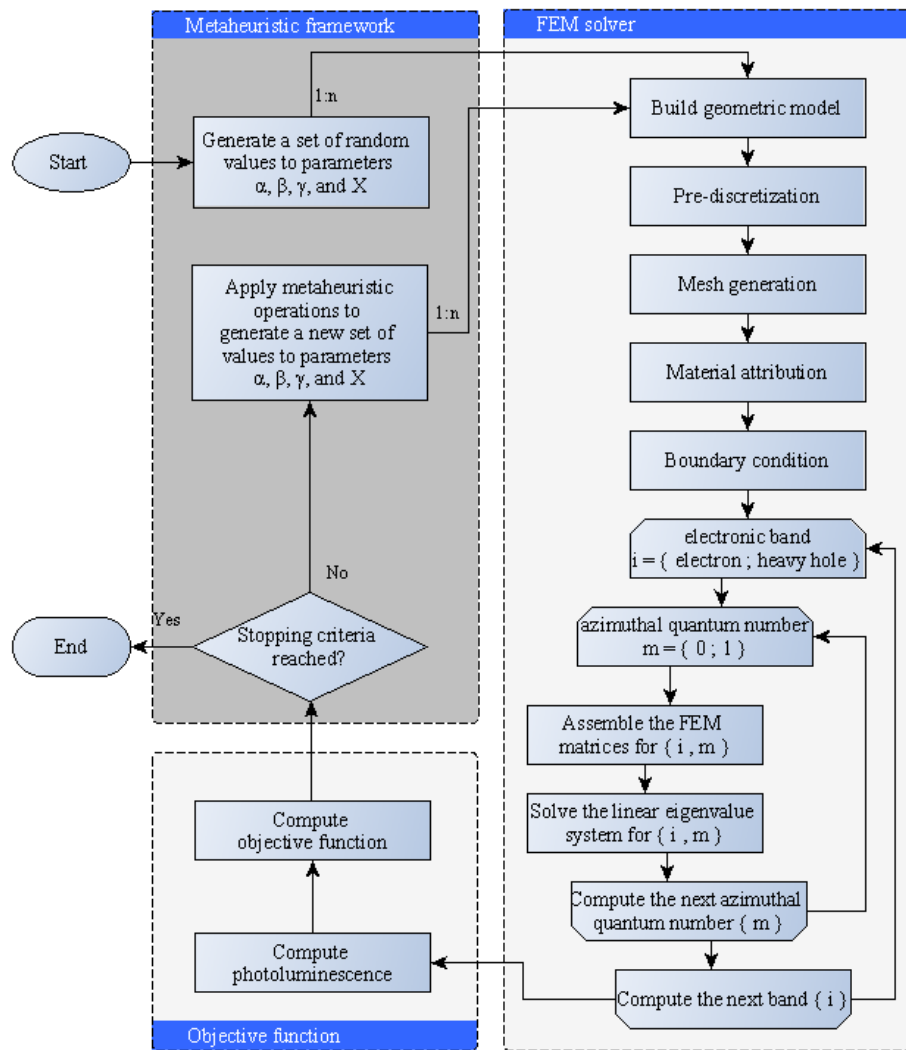


FIGURE 3.29 – Flowchart of the inverse problem.

4 Results and discussion

The reference sample used in this work consists of InAs/GaAs QDs grown by MBE. The growing details are described elsewhere [108]. The experimental data of a low-temperature PL measurement (Figure 4.1-a) of this sample shows a spectrum having two well separated excitonic emission peaks: the strongest one, around 1.068 eV, was assigned to the e1hh1 transition, while the lowest one, close to 1.141 eV, was related to the recombination from the first excited state (e2hh1). Figure 4.1-b shows a high-resolution cross-section TEM image of this sample, from which we could estimate the average base diameter and height of our buried QD, about 20 and 4 nm, respectively.

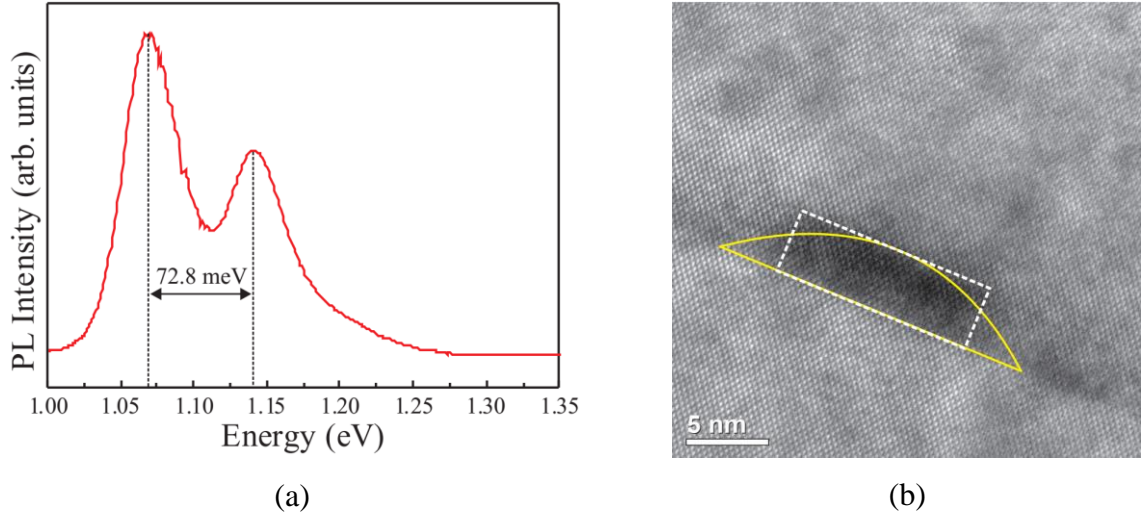


FIGURE 4.1 – (a) Low-temperature PL spectrum of the reference QD sample. (b) TEM image of the same sample showing a typical QD after GaAs capping. The full line shows the lens shape adopted in the first simulations, while the dashed line represents the disk shape used in the last simulations of this monograph. (Reproduced from [70].)

Figures 4.2-a and 4.2-b represents the indium distribution in a lens-shaped QD obtained by using the Giddings model with the parameters ($\alpha = 0.5$, $\beta = 1$, $\gamma = 1$, $X = 0.6$) and a homogeneous pure InAs distribution, respectively. The computer codes developed in this work are used to calculate the transition energies of lens-shaped QDs as a function of its base radius R_{QD} for height $H_{\text{QD}} = 3, 4$, and 5 nm for both proposed indium distributions. The results are plotted in Figure 4.2-c. The e1hh1 and e2hh1 emission energies observed in PL spectrum are also indicated as horizontal dashed lines across the figure, to be used as reference values. As can be seen in Figure 4.2, only one case ($R_{\text{QD}} = 4$ nm and $H_{\text{QD}} = 3$ nm) shows a result that

is close to the experimental e1hh1 transition energy when a homogeneous InAs distribution is assumed (empty symbols). However, such QD dimensions are far from the values estimated in the TEM image of the reference sample ($R_{\text{QD}} = 10$ nm and $H_{\text{QD}} = 4$ nm). This clearly suggests that a non-homogeneous indium distribution has to be taken into account in order to reproduce the experimental optical data. The results from the Giddings model show a blueshift when compared to the respective values obtained with the uniform InAs distribution, mostly due to the fact of lower average indium concentration in the QD, which results in a larger band gap. Moreover, the potential well of the electrons in the Giddings model with these parameter values is shallower. In this case, we find only one confined state.

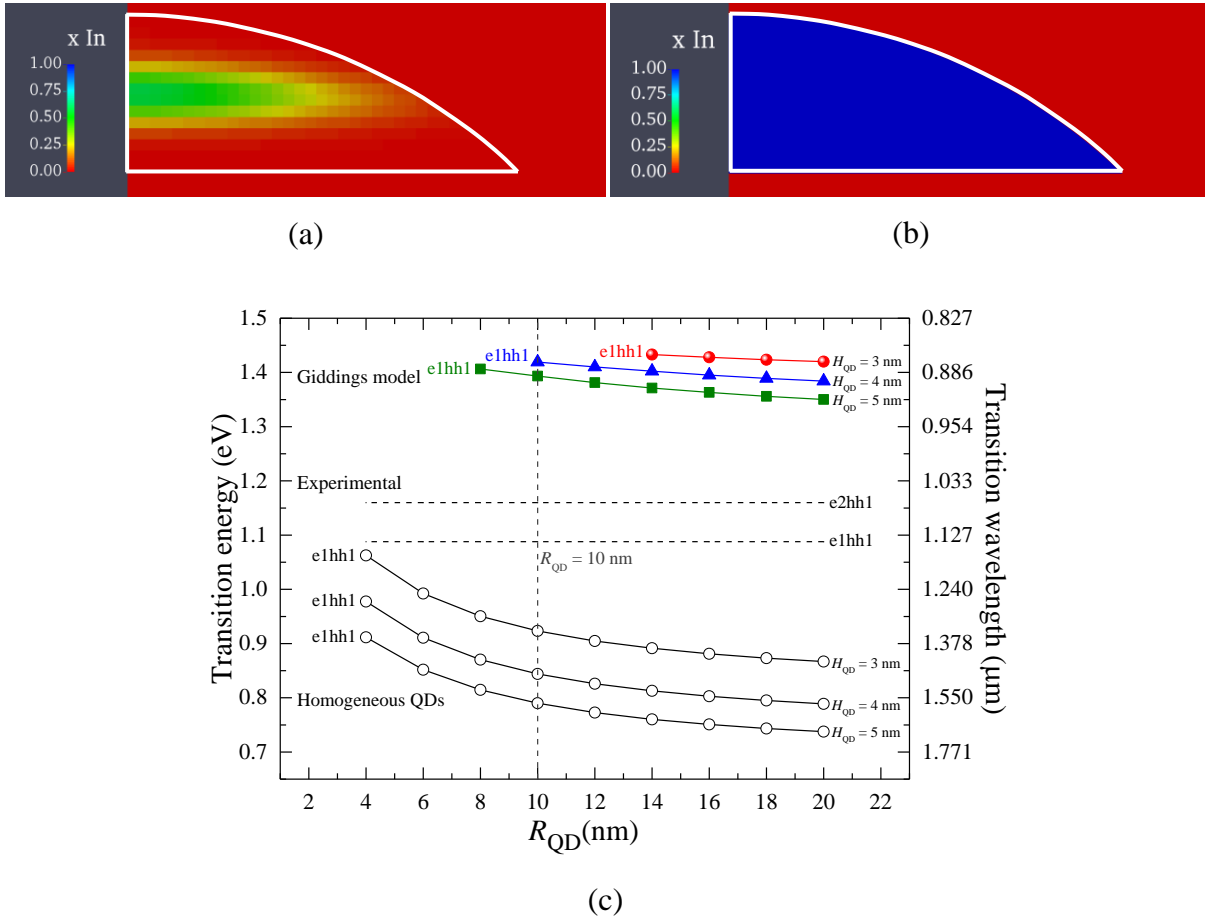


FIGURE 4.2 – Energy values of the fundamental transition energy e1hh1 from the ground state (e1) in conduction band to the first heavy-hole state (hh1) in the valence band for several QD heights and base radii. Comparison between the Giddings model and pure InAs QD results.

Figures 4.3-a and 4.3-b represents the indium distribution in a lens-shaped QD obtained by using the Blokland model with the parameters (β , γ , X) all equal 1 and a homogeneous pure InAs distribution. Again, the computer codes developed in this work are

used to calculate the transition energies of lens-shaped QDs as a function of its base radius R_{QD} for height $H_{\text{QD}} = 3, 4, \text{ and } 5 \text{ nm}$ for this indium distribution and the results were compared to the values already computed for the homogeneous pure InAs distribution.

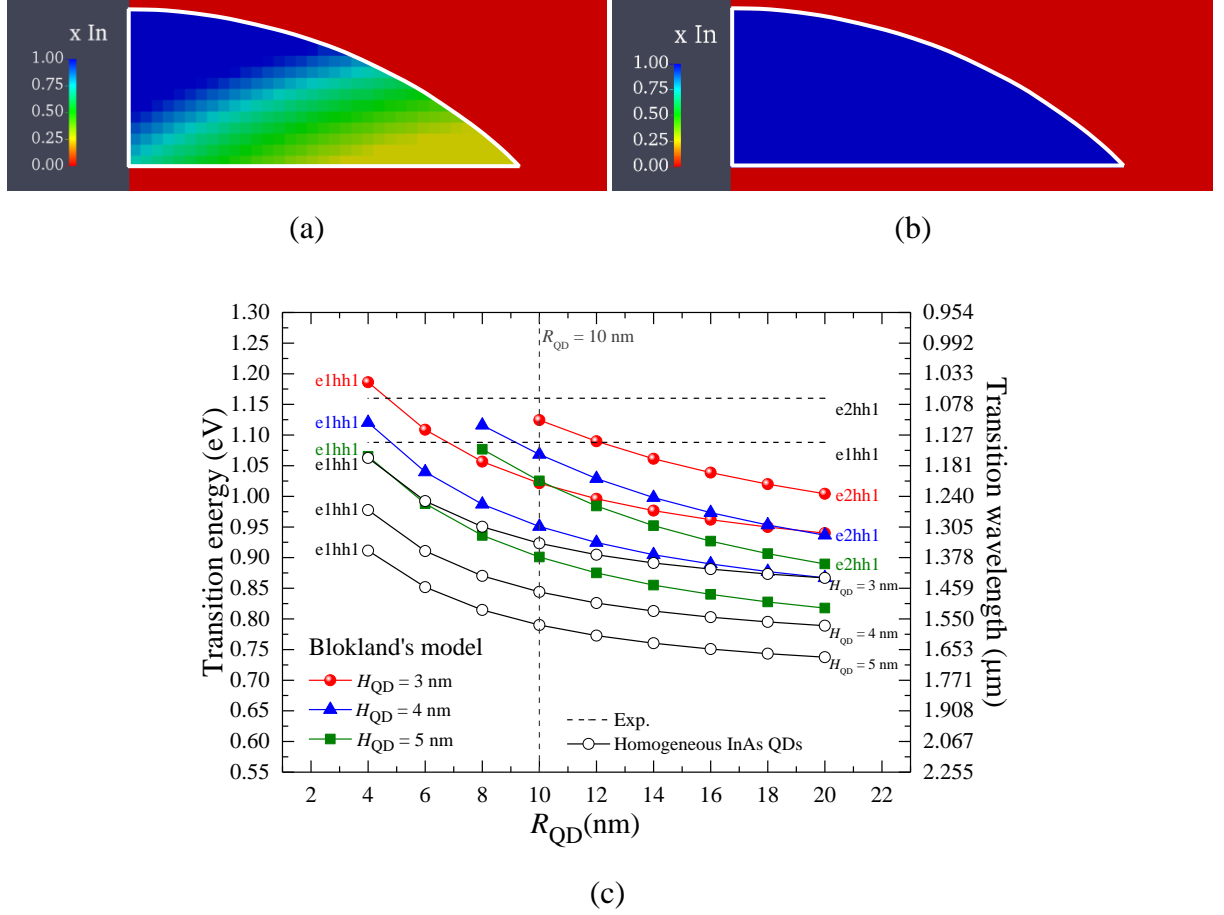


FIGURE 4.3 – Transition energies e1hh1 from the ground state (e1) in conduction band to the first heavy-hole state (hh1) in the valence band and e2hh1 from the first excited state (e2) in conduction band to the first heavy-hole state (hh1) in the valence band for several QD heights and base radii. Comparison between the Blokland model and pure InAs QD results.

Figure 4.3 reveals that the theoretical data obtained with the Blokland model of non-homogeneous indium distribution have two matches for e1hh1 transition. One case of a QD with height of 3 nm and base radius of approximately 7 nm and the other case of a QD with height of 4 nm and base radius of approximately 5 nm. But again, these dimensions are far from what we observed with the TEM images. Moreover, none of the cases matched the e2hh1 transition.

We solve the inverse problem, Equation (3.5), for a lens shaped QD with base radius R_{QD} of 10 nm and height H_{QD} of 4 nm considering both the Giddings and Blokland models,

trying to find sets of parameters (α , β , γ , X) that allow to reproduce the experimental PL peaks. The range of variation of each parameter of the Giddings model is:

$$0.1 \leq \alpha \leq 2.0,$$

$$0.1 \leq \beta \leq 2.0,$$

$$0.1 \leq \gamma \leq 2.0,$$

$$0.1 \leq X \leq 2.0.$$

The values of parameters and objective function for the best results obtained from the Giddings model are presented in Table 4.1. All these cases matched the experimental PL peaks with difference on the order of 1 meV. The corresponding image of the indium distribution profile for each case identified by the key “Case_ID” are presented in Figure 4.4.

TABLE 4.1 – Values of parameters α , β , γ , and X for the cases with smallest values of objective function for a lens-shaped QD ($R_{\text{QD}} = 10$ nm, $H_{\text{QD}} = 4$ nm).

Case_ID	α	β	γ	X	O_F
L_PSO_t3	0.4092	1.5057	0.2790	1.5452	8.70×10^{-7}
L_PSO_t4	0.4429	1.6529	0.2787	1.5158	4.70×10^{-6}
L_PSO_t0	0.3158	1.2201	0.2661	1.7647	2.99×10^{-6}
L_BH_t0	0.3382	1.4916	0.3262	1.2587	5.09×10^{-4}
L_GA_t4	0.4131	1.6971	0.3024	1.3315	6.28×10^{-4}
L_GA_t2	0.3827	1.6430	0.3294	1.2232	7.73×10^{-4}
L_BH_t1	0.3165	1.3772	0.3085	1.3786	7.79×10^{-4}

All the cases presented in Table 4.1 present a value of parameter X greater than 1 indicating an indium concentration higher than 100%, which is of course physically unrealistic. When that happens, the program automatically truncates the Gaussian curve where the value is greater than 1 and limits the indium content to 100%. This actually contributes to increase the average indium concentration and broadens the region of the QD where the indium content is maximum.

A maximum indium concentration of 100% instead of 60% is coherent to the fact that the maximum concentration (60%) originally proposed by Giddings *et al.* might be underestimated since the samples were measured by XSTM. For such an experiment, the

samples need to be cleaved in situ, and the exposed surface might pass anywhere within the QDs (close to the border or right through their center).

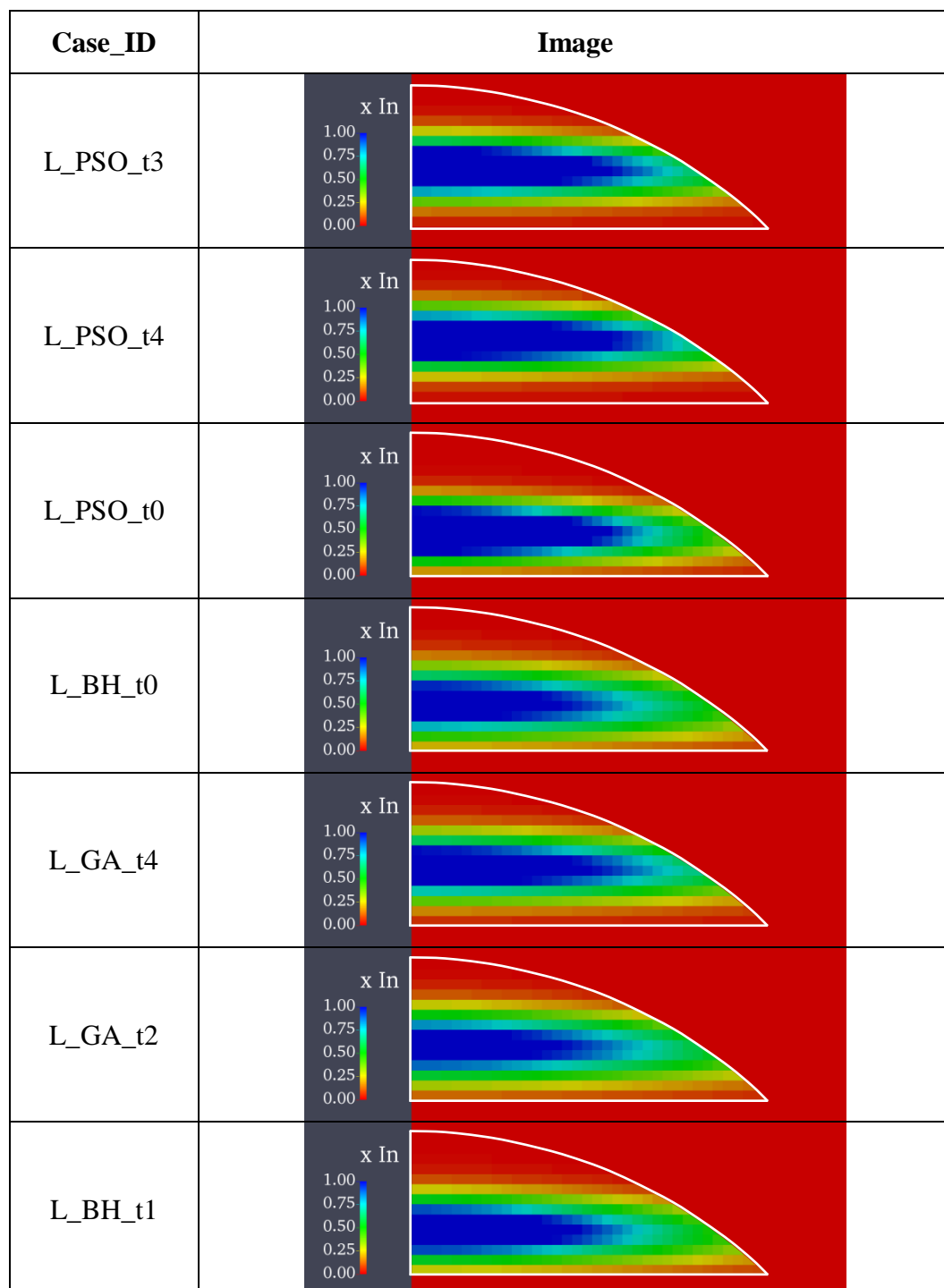


FIGURE 4.4 – Theoretical results of indium distribution that reproduce the experimental PL peaks according to the Giddings model using the parameters values presented in Table 4.1.

There are many possible solutions to the problem. Although all of them provided the right values for $e1hh1$ and $e2hh1$, the fact that there are 4 fitting parameters allows us the possibility to make minor changes to any two (or more) of those four parameters to obtain another valid solution, but all of the obtained results are qualitatively similar and have fitting parameters showing a variation of the order of 10-20%. A closer look at the figures in Figure 4.4 reveals that the indium concentration at the top of the QD goes to zero before reaching the maximum height of 4 nm, what actually makes the QD slightly lower and flatter than the lens shape initially adopted in the calculations. In that way, the QD looks like a truncated cone, and might even be approximated by a disk, as sometimes found in the literature [36, 68]. When the distribution profile, characterized by the values of parameters α , β , γ , and X presented in Table 4.1, is used to distribute material in a disk shaped QD we observed that the theoretical results fits very well with the experimental data for a QD with $R_{QD} = 8$ nm and $H_{QD} = 4$ nm (see [70] for more details). This is consistent to the fact that, though the QD appearing in the TEM image of the reference sample was initially supposed to have a lens shape (with a radius and height of $R_{QD} = 10$ nm and $H_{QD} = 4$ nm, respectively) it might actually be intuitively better approximated by a small disk with $R_{QD} = 8$ nm and $H_{QD} = 4$ nm, as shown in Figure 4.1-b.

Executing the inverse problem considering a disk shaped QD with base radius of 8 nm and height of 4 nm generated the results presented in Table 4.2. The respective images of the material profile are presented in Figure 4.5. The parameter α in the case of QD with the shape of a disk has a minimum effect since this format has symmetry along the growth direction, which is not the case for lens-shaped QD. Hence, the values of parameters β , γ , and X maintain the original variation of the order of 10-20% as previously stated although the difference between the values of α presented in Table 4.2 are greater than 50%.

TABLE 4.2 – Values of parameters α , β , γ , and X for the cases with smallest values of objective function for a disk-shaped QD ($R_{QD} = 8$ nm, $H_{QD} = 4$ nm).

Case_ID	α	β	γ	X	O_F
D_PSO_t3	0.4669	1.4512	0.2906	1.4554	1.11×10^{-5}
D_PSO_t1	0.3278	1.4704	0.2920	1.4496	2.11×10^{-5}
D_PSO_t0	0.6389	1.3937	0.2730	1.6158	1.75×10^{-4}

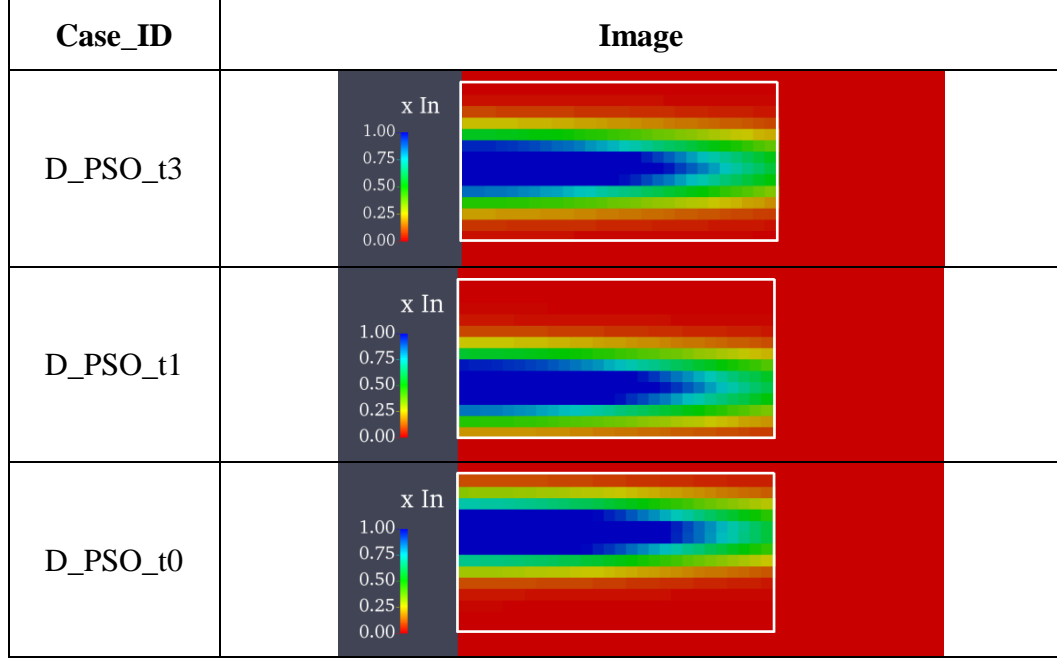


FIGURE 4.5 – Theoretical results of indium distribution that reproduce the experimental PL peaks according to the Giddings model using the parameters values presented in Table 4.2.

The set of solutions in Tables 4.1 and 4.2 can be described as $\alpha = 0.4 \pm 0.1$, $\beta = 1.5 \pm 0.2$, $\gamma = 0.29 \pm 0.02$ and $X = 1.5 \pm 0.2$. Despite the variation of the parameters, the indium profiles are still qualitatively very similar and in good agreement with the PL data and the experimental results of the literature (elongated indium-rich core).

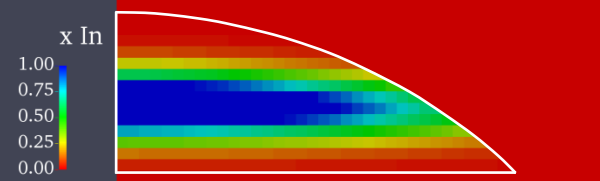
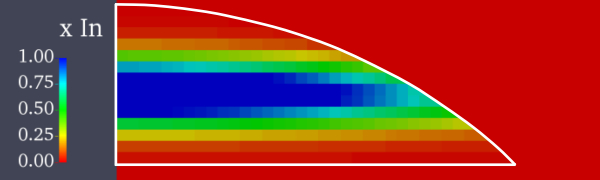
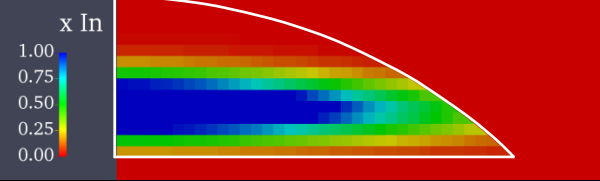
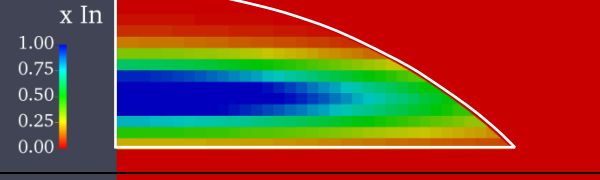
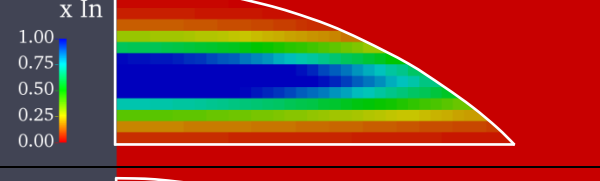
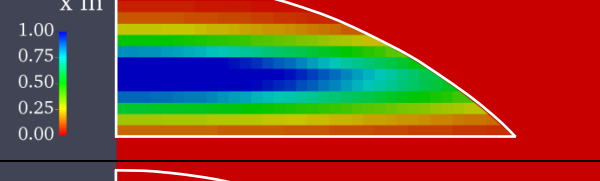
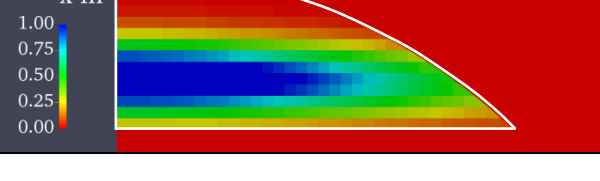
We have also solved the inverse problem with the Blokland model. The range of variation of each parameter of the model is:

$$\begin{aligned} 0.1 &\leq \beta \leq 2.0, \\ 0.1 &\leq \gamma \leq 2.0, \\ 0.1 &\leq X \leq 2.0. \end{aligned}$$

With this range of parameters, we allowed the indium concentration to vary from 0% to 70% at the center of the QD base, and from 0 to 50% in the border of the base. However, even with this flexibility in the parameters values we did not find any solution with this model.

4.1 The elastic potential energy

The results of computation of the elastic potential energy for the cases presented in the previous section are presented in Figure 4.6, in which the image of the indium profile are repeated aiming to help the reader to compare the results.

Case_ID	Image		U (J) [U (eV)]
L_PSO_t3			2.87×10^{-16} [1789.9]
L_PSO_t4			3.04×10^{-16} [1894.5]
L_PSO_t0			2.74×10^{-16} [1713.0]
L_BH_t0			2.27×10^{-16} [1415.3]
L_GA_t4			2.69×10^{-16} [1680.0]
L_GA_t2			2.32×10^{-16} [1447.2]
L_BH_t1			2.38×10^{-16} [1485.0]

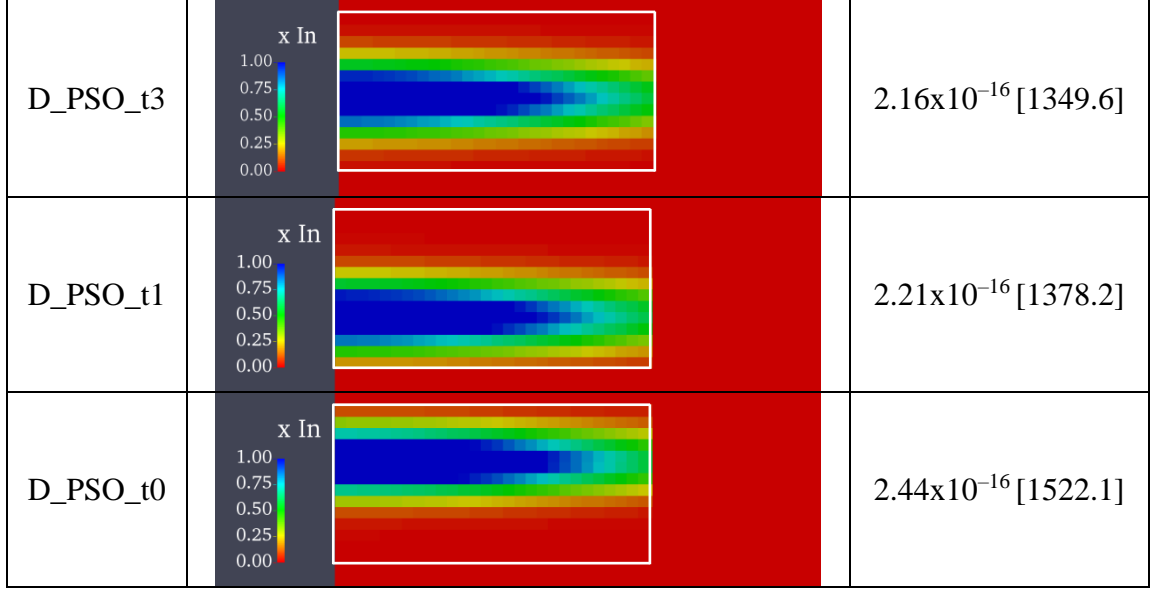


FIGURE 4.6 – Profile of indium distribution and elastic potential energy for the best solution found according to the Giddings model using the parameters values presented in Tables 4.1 and 4.2.

Assuming that the indium distribution is associated with a minimization of the elastic potential energy, we can elect the best configuration among the results presented previously. In Figure 4.6 the case with the minimum elastic potential energy is the one identified by “D_PSO_t3”. From this set of solutions, the average elastic potential energy is $(2.5 \pm 0.3) \times 10^{-16}$ J.

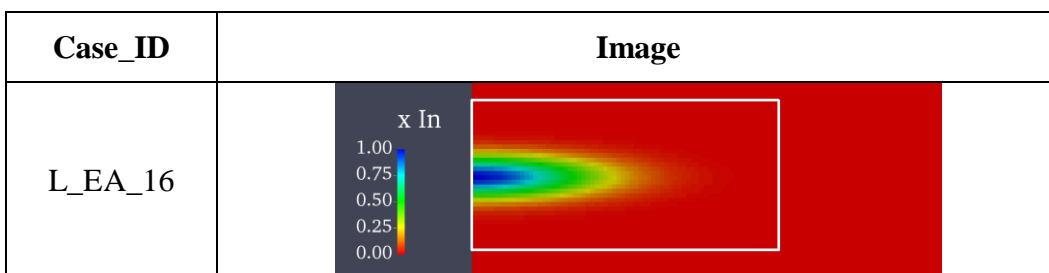
The inclusion of the elastic potential energy, Equation (2.5), into the objective function, Equation (3.6), is a step forward into the challenge to determine the non-uniform indium distribution inside self-assembled QDs. In order to maintain the original formulation of the Giddings model presented in section 3.4 and the meaning of the parameters β and γ , we define a large cylindrical region used just for reference, which is much greater than the expected dimensions of the QD. We let the inverse problem adjust automatically the indium content inside this region, i.e., the shape and size of the QD are determined freely by the minimization process. We maintain the labels R_{QD} and H_{QD} , but now they represent the size of the reference cylinder. Since the α parameter has little impact on the energy values for disk-shaped QDs (see results presented previously in this chapter), the α parameter value was fixed in 0.5, locating the peak of the Gaussian curve exactly at the middle of the cylindrical region in the growth direction. The values of the parameters α , β , γ , and X for the representative cases obtained by solving the inverse problem and ordered by the computed elastic potential energy are presented in Table 4.3. In order to allow direct comparison with the previous cases, the

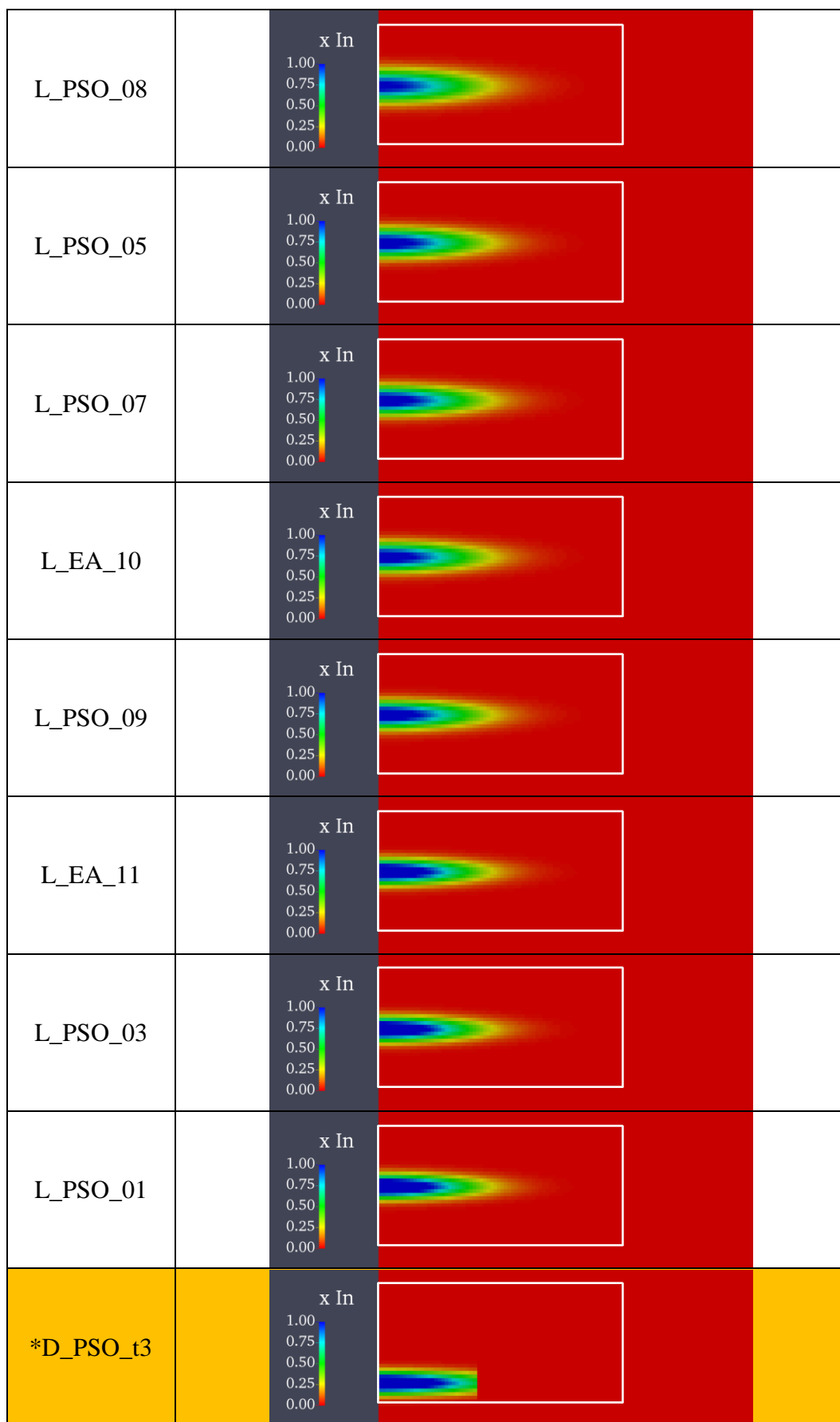
parameters γ and α were multiplied by H_{QD} , and the parameter β was multiplied by R_{QD} . The best result (“D_PSO_t3”) published in [70] was included for comparison with these new results. The respective images of the material distribution profile are presented in Figure 4.7. All these results match precisely the two PL peaks. Notice that for “D_PSO_t3” the indium distribution seems to be clipped in the r -direction. However, it is a natural consequence of the approach adopted by the first inverse problem model for which the region of the QD has to be previously defined in order to obtain results compatible with TEM images.

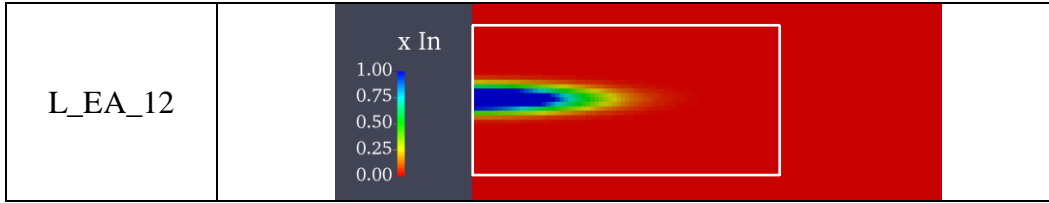
TABLE 4.3 – Values of parameters α , $\beta \cdot R_{\text{QD}}$, $\gamma \cdot H_{\text{QD}}$, and X for the best cases ordered by objective function ($R_{\text{QD}} = 20$ nm, $H_{\text{QD}} = 10$ nm, $*R_{\text{QD}} = 8$ nm, $*H_{\text{QD}} = 4$ nm).

Case_ID	$\alpha \cdot H_{\text{QD}}$ (nm)	$\beta \cdot R_{\text{QD}}$ (nm)	$\gamma \cdot H_{\text{QD}}$ (nm)	X	U (eV)
L_EA_16	5.000	11.123	1.845	1.0000	524.6
L_PSO_08	5.000	11.008	1.697	1.0477	598.0
L_PSO_05	5.000	10.782	1.503	1.1397	737.3
L_PSO_07	5.000	10.750	1.487	1.1509	751.0
L_EA_10	5.000	10.744	1.486	1.1521	752.2
L_PSO_09	5.000	10.638	1.424	1.1964	814.3
L_EA_11	5.000	10.222	1.275	1.3577	997.5
L_PSO_03	5.000	10.184	1.257	1.3814	1027.3
L_PSO_01	5.000	10.012	1.214	1.4507	1095.1
*D_PSO_t3	1.868	11.610	1.162	1.4554	1349.6
L_EA_12	5.000	9.043	1.026	1.9993	1507.5

* Result with minimum objective function obtained from the inverse problem without elastic potential energy







* Best result obtained from the inverse problem without elastic potential energy

FIGURE 4.7 – Theoretical results of indium distribution according to the Giddings model that reproduce the experimental PL peaks and minimizing the elastic potential energy, using the parameters values presented in Table 4.3.

The best solution presents an elastic potential energy five times smaller than the previous results, Figure 4.6. It is possible to observe a trend in the data presented in Table 4.3 and Figure 4.7. The strain energy is stronger when there is a heavy concentration of indium in the QD core as can be seen in the case “L_EA_12”. This is evidenced by the high value of X parameter, which is 1.9993, greater than 1 meaning that the distribution should contain a broader region where the indium content is maximum (100%, pure InAs). It is quite clear the direct correlation between the parameter X and the elastic potential energy evidenced in graph shown in Figure 4.8, in which the minimum elastic potential energy was achieved with the configuration with the minimum value of the parameter X . The behavior of β and γ as a function of X are shown in Figure 4.9, which indicates that as X decreases both variables increase. On other words, as the region where the maximum content decreases, the QD height and radius increase due to diffusion of indium atoms to the nearby regions, conserving approximately the total quantity of indium. This can be observed in the Figure 4.10 in which the cases with the greatest elastic potential energy (“L_EA_12”) and the one with smallest (“L_EA_16”) are reproduced together in order to facilitate the comparison. A small rectangle (dotted lines) with height of 4 nm and length of 10 nm was drawn around the indium distribution and we can observe that the indium distribution of the case “L_EA_16” occupies approximately the region of the small rectangle. This is a very interesting result because the best configuration found by the inverse problem has approximately the dimensions observed in the TEM image and it converged to this solution naturally without imposition of a QD size.

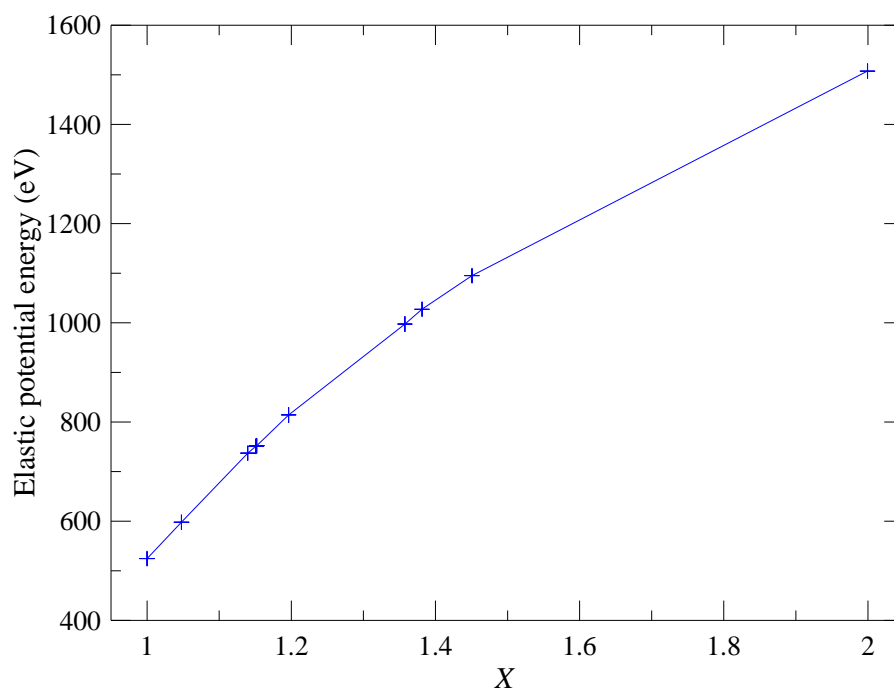


FIGURE 4.8 – Plot of the elastic potential energy as a function of the value of parameter X .

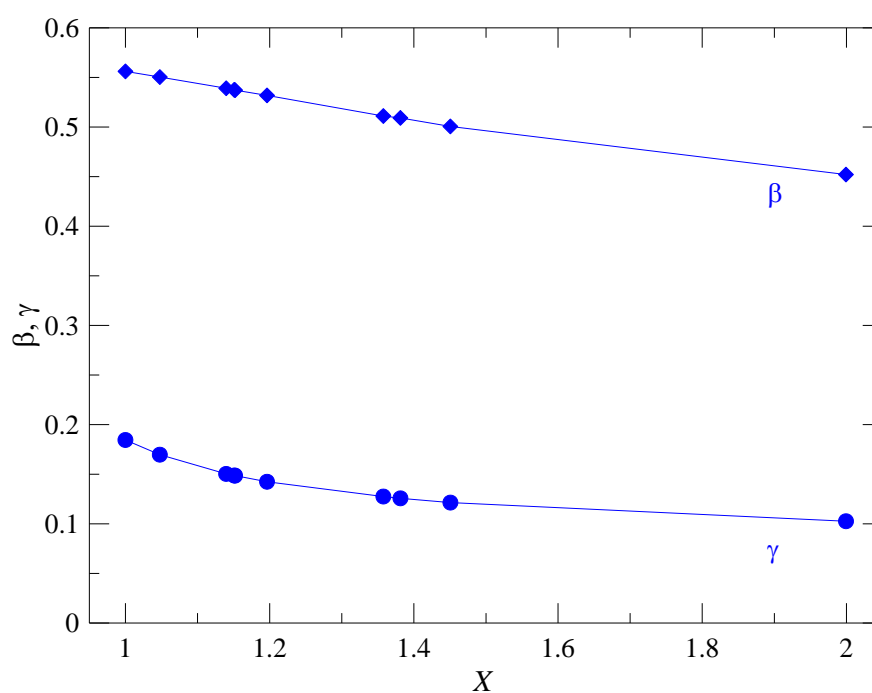


FIGURE 4.9 – Plots of the parameters β (diamond) and γ (circle) as a function of the value of parameter X .

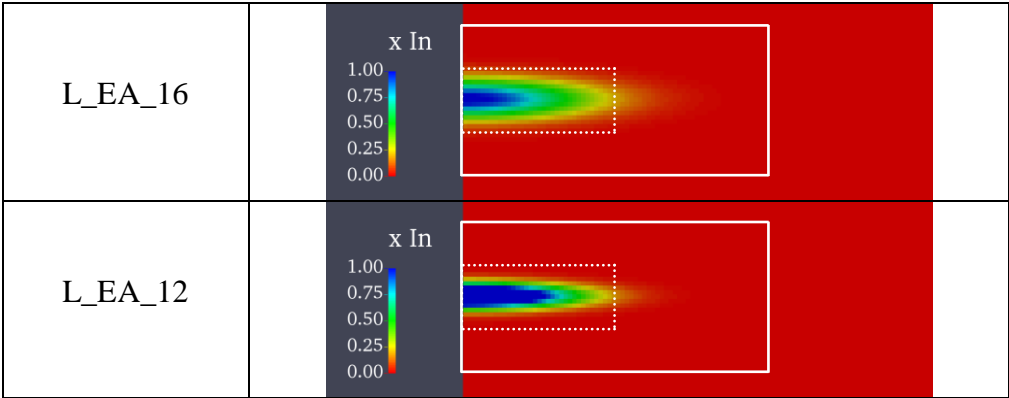


FIGURE 4.10 – Comparison between the case with the smallest (“L_EA_16”) elastic potential energy and the greater (“L_EA_12”) one. Dimensions (height x length) of rectangle with continuous lines: 10 nm x 20 nm. Dimension of rectangle with dotted lines: 4 nm x 10 nm.

The strain distribution for the case “L_EA_16” is presented in Figure 4.11. In the region near the center of the QD there is a compressive (negative ϵ_{xx}) strain in the radial plane, Equation (2.2), and a tensile strain (positive ϵ_{zz}) in the growth direction, Equation (2.3). The strain distribution trends to minimize the strain at the QD center.

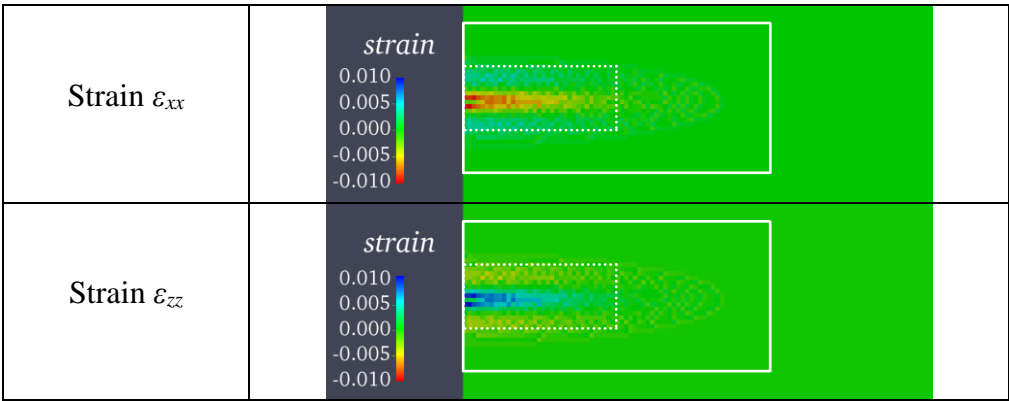


FIGURE 4.11 – Strain distribution for the case “L_EA_16”. Dimensions (height x length) of a rectangle with continuous lines: 10 nm x 20 nm. Dimension of rectangle with dotted lines: 4 nm x 10 nm.

5 Conclusion and future works

The better understanding of the non-homogeneity in the composition of self-assembled QDs is essential to improve the performance of QD based devices since they have direct impact on the eigenstates confined in these nanostructures. In this context, this thesis developed a methodology to estimate the 3D indium distribution in a self-assembled QD, based on the solution of an inverse problem and computation of the wave functions considering nonuniformity in the indium distribution and anisotropic strain in the lattice. Defined the properties associated to the QD, e.g., indium distribution, material strain, and electronic and hole bands, a finite element code was used to compute the energy of the quantum states of the conductive and the valence bands. The inverse problem was solved by using three different metaheuristics, improving the quality of the solutions. The three methods present compatible solutions in all tests carried out.

Two models of indium distribution within the QD were adopted in this work. These models, based on published papers, present different patterns of indium distribution, which should have impact on the electronic properties of the self-assembled structures. These models were parametrized and the set of parameters which allows to reproduce, at least qualitatively, the indium concentration proposed by the original authors were identified. It is worthwhile to mention that these set of parameters were not able to reproduce the experimental spectrum of photoluminescence.

Two models of inverse problem were proposed in this thesis. The first one needs a minimum of two inputs from a QD sample: a photoluminescence spectrum, and an approximate size of the QD. The indium distribution is established by evaluating the adequacy of each tentative distribution in terms of the energy of the photoluminescence peaks. In this case, there are several solutions for this problem and the experimental estimative of the QD size allows to obtain a subset of solutions compatible with the actual experimental data. The second model of inverse problem needs only one input: the photoluminescence spectrum. This last model takes into account the minimization of the elastic potential energy that remains after the coalescence of the self-assembled QD. The energy of the photoluminescence peaks are used to penalize tentative solutions that do not fit well the peaks energy. In this work, the tentative solutions are penalized by using multiplicative function, which takes the value 1 if the energy is compatible with the estimated

experimental error and has an exponential behavior as a function of the difference between the experimental and calculated peaks.

All solutions obtained from the two inverse problem formulations display indium distribution profiles qualitatively very similar and present good agreement with the PL data and the experimental results of the literature (elongated indium-rich core). Additionally, the second inverse problem formulation allows to obtain naturally a QD size which is in very good agreement with the size estimated from TEM image.

Moreover, only the Giddings model allows to obtain good solutions by the inverse problem formulations. We could not obtain solutions that resemble the distribution of indium proposed by Blokland et al. [70].

The methodology developed led to a novel and up-to-date computer program that can retrieve the qualitative and quantitative nature of a self-assembled QD sample. To the best of our knowledge, this is the first implementation that can take into account both the lateral and radial non-homogeneous composition within a QD and use this information to find a configuration that attends to multiple objectives such as the determination of the QD dimension for a given QD shape and to estimate the value of the energy peaks observed in PL measurements.

The computer program was built to take into account the WL and also to guarantee that the BenDaniel-Duke boundary condition on interfaces be respected. It was shown that both the WL and the imposition of the BenDaniel-Duke boundary condition have little impact on the energy values of confined states and its use increases too much the computational time. The WL might have a significant influence in studies of structures such as dots-in-a-well and vertically aligned QDs in which there is a coupling of the wave functions from several nanostructures. The BenDaniel-Duke continuity of the wave function might have influence when computing the dark current, which depends on the wave function at regions of interface. The WL and the BenDaniel-Duke continuity condition were not used in this work to evaluate the indium distribution within the QD.

Using the computational program we confirmed that the hypothesis of QDs made of pure InAs is incompatible with the available optical and structural data of an InAs/GaAs QDs sample grown by MBE, and that a non-homogeneous composition profile must be taken into account. A study including the WL could be executed with minor modifications in the current computer codes since all the necessary tools are already implemented.

There are several improvements that can be implemented in the developed program such as the inclusion of a self-consistent computation of the excitonic binding energy in QDs

but the first in list is the development and implementation of a method to compute the interband oscillator strength, which will allow to compute also the relative peak intensities of the PL spectra. Such additional tool will include information, which can be used as additional restrictions to solve the inverse problem.

A real three-dimensional FEM model will be necessary in order to compute lateral coupling of QDs but other coupling between nanostructures can be already be studied such as dots-in-a-well and vertical aligned QDs.

5.1 Dots-in-a-well nanostructures

Dots-in-a-well (DWELL) is a nanostructure in which QDs are embedded inside a quantum well (QW). Optical transitions in a DWELL can happen between states of the QD and between a state of the QD and a state of the QW. DWELL structure made of InAs QDs within a $\text{In}_{0.15}\text{Ga}_{0.85}\text{As}$ QW has been reported in several papers for use in both infrared detector [118–120] and laser [121] device applications. In an experimental work [122], a $\text{InAs}/\text{In}_{0.15}\text{Ga}_{0.85}\text{As}/\text{GaAs}$ DWELL photodetector was tuned to detect radiation with wavelength from 2-3 μm to 8-12 μm . This structure was designed to detect radiation through transitions between a state of QD and a state of the QW and selection of the wavelength was done by fine-tuning the QW width in the range between 30 Å to 50 Å. The intraband optical transitions of DWELL was extensively studied in [123] for different sizes of QDs and QWs. It also studied the effect of the position of the QD inside the QW, computing the optical absorption spectra with the QD positioned at the bottom of the QW and the QD positioned near the top inside the QW. The conclusion was that the spectra of absorption have weak dependence on both the QW size and the position of the QD (at the bottom or at the top) inside the QW. On the other hand, a stronger dependency was found between the QD size and the optical absorption spectra. However, the non-homogeneity in composition of QDs was not taken into account yet in the literature. A further insight from the optical transitions might be achieved including the non-homogeneity in QD composition into the computation of electronic states of DWELL nanostructures.

5.2 Vertically aligned QDs

The vertical alignment of QDs is a subject of great interest because it was found to enhance performance of devices such as light emitting diodes, lasers, infrared detectors, and solar cells [124–130]. Besides, the growth mechanism of these structures is relatively easy because the intrinsic strain in the formation of self-assembled QDs tends naturally to align vertically the QDs when a layer of QDs array is grown over the top of a previous one [131], leading to a formation of an array-like assembly of similar but not exactly equal vertical QDs as reported in [67]. The effects of the thickness of the space layers that vertically separate the QDs were studied in [132]. A theoretical study of the electronic structure of coupled pyramidal-shaped QDs on wetting layers is presented in [133]. The effect of the non-homogeneity in composition of QDs in vertically coupled QDs can be studied almost immediately with the computer code developed in this thesis.

Bibliography

- [1] KOUWENHOVEN, L. P.; AUSTING, D. G.; TARUCHA, S. Few-electron quantum dots. **Reports on Progress in Physics**, v. 64, n. 6, p. 701–736, 2001.
- [2] SAITO, H.; NISHI, K.; OGURA, I.; SUGOU, S.; SUGIMOTO, Y. Room-temperature lasing operation of a quantum-dot vertical-cavity surface-emitting laser. **Applied Physics Letters**, v. 69, n. 21, p. 3140, 1996.
- [3] FAFARD, S.; HINZER, K.; RAYMOND, S.; et al. Red-Emitting Semiconductor Quantum Dot Lasers. **Science**, v. 274, n. 5291, p. 1350–1353, 1996.
- [4] SELLIN, R. L.; RIBBAT, C.; GRUNDMANN, M.; LEDENTSOV, N. N.; BIMBERG, D. Close-to-ideal device characteristics of high-power InGaAs/GaAs quantum dot lasers. **Applied Physics Letters**, v. 78, n. 9, p. 1207, 2001.
- [5] LOSS, D.; DIVINCENZO, D. P. Quantum computation with quantum dots. **Physical Review A**, v. 57, n. 1, p. 120–126, 1998.
- [6] TAYLOR, J. M.; PETTA, J. R.; JOHNSON, A. C.; et al. Relaxation, dephasing, and quantum control of electron spins in double quantum dots. **Physical Review B**, v. 76, n. 3, p. 35315, 2007.
- [7] BLUHM, H.; FOLETTI, S.; MAHALU, D.; UMANSKY, V.; YACOBY, A. Enhancing the Coherence of a Spin Qubit by Operating it as a Feedback Loop That Controls its Nuclear Spin Bath. **Physical Review Letters**, v. 105, n. 21, p. 216803, 2010.
- [8] BAYER, M. Coupling and Entangling of Quantum States in Quantum Dot Molecules. **Science**, v. 291, n. 5503, p. 451–453, 2001.
- [9] LIU, H. C.; GAO, M.; MCCAFFREY, J.; WASILEWSKI, Z. R.; FAFARD, S. Quantum dot infrared photodetectors. **Applied Physics Letters**, v. 78, n. 1, p. 79, 2001.
- [10] RYZHII, V.; KHMYROVA, I.; MITIN, V.; STROSCIO, M.; WILLANDER, M. On the detectivity of quantum-dot infrared photodetectors. **Applied Physics Letters**, v. 78, n. 22, p. 3523, 2001.
- [11] MARTI, A.; CUADRA, L.; LUQUE, A. Partial filling of a quantum dot intermediate band for solar cells. **IEEE Transactions on Electron Devices**, v. 48, n. 10, p. 2394–2399, 2001.
- [12] NOZIK, A. . Quantum dot solar cells. **Physica E: Low-dimensional Systems and Nanostructures**, v. 14, n. 1–2, p. 115–120, 2002.
- [13] MALLARY, M.; SRINIVASAN, K.; BERTERO, G.; et al. Head and Media Challenges for 3 Tb/in² Microwave-Assisted Magnetic Recording. **IEEE Transactions on Magnetics**, v. 50, n. 7, p. 1–8, 2014.
- [14] TEO, K. K.; CHAN, K. S.; GREAVES, S. J.; KANAI, Y. Areal Density Prediction for Microwave-Assisted Magnetic Recording. **IEEE Transactions on Magnetics**, v. 51, n. 11, p. 1–4, 2015.
- [15] IMAMURA, K.; SUGIYAMA, Y.; NAKATA, Y.; MUTO, S.; NAOKIYOKOYAMA.

New Optical Memory Structure Using Self-Assembled InAs Quantum Dots. **Japanese Journal of Applied Physics**, v. 34, n. Part 2, No. 11A, p. L1445–L1447, 1995.

- [16] KROUTVAR, M.; DUCOMMUN, Y.; HEISS, D.; et al. Optically programmable electron spin memory using semiconductor quantum dots. **Nature**, v. 432, n. 7013, p. 81–84, 2004.
- [17] MORELLO, A.; PLA, J. J.; ZWANENBURG, F. A.; et al. Single-shot readout of an electron spin in silicon. **Nature**, v. 467, n. 7316, p. 687–691, 2010.
- [18] SYSTEM, U. A. Third Infrared Window. Disponível em: <<http://www.sensorsinc.com/technology/third-infrared-window>>. Acesso em: 20/6/2016.
- [19] DOWNS, C.; VANDERVELDE, T. Progress in Infrared Photodetectors Since 2000. **Sensors**, v. 13, n. 4, p. 5054–5098, 2013.
- [20] ROGALSKI, A. HgCdTe infrared detector material: history, status and outlook. **Reports on Progress in Physics**, v. 68, n. 10, p. 2267–2336, 2005.
- [21] HANSEN, G. L. Energy gap versus alloy composition and temperature in $\text{Hg}_{1-x}\text{Cd}_x\text{Te}$. **Journal of Applied Physics**, v. 53, n. 10, p. 7099, 1982.
- [22] BHATTACHARYA, P.; SU, X. H.; CHAKRABARTI, S.; ARIYAWANSA, G.; PERERA, A. G. U. Characteristics of a tunneling quantum-dot infrared photodetector operating at room temperature. **Applied Physics Letters**, v. 86, n. 19, p. 191106, 2005.
- [23] MARTYNIUK, P.; ROGALSKI, A. Quantum-dot infrared photodetectors: Status and outlook. **Progress in Quantum Electronics**, v. 32, n. 3–4, p. 89–120, 2008.
- [24] UPADHYAY, S.; MANDAL, A.; AGARWAL, A.; et al. Enhancement in multicolor photoresponse for quaternary capped $\text{In}_{0.5}\text{Ga}_{0.5}\text{As}/\text{GaAs}$ quantum dot infrared photodetectors implanted with hydrogen ions. **Materials Research Bulletin**, v. 84, p. 79–84, 2016.
- [25] DAS, D.; GHADI, H.; SENGUPTA, S.; et al. Optimization of the Number of Stacks in the Submonolayer Quantum Dot Heterostructure for Infrared Photodetectors. **IEEE Transactions on Nanotechnology**, v. 15, n. 2, p. 214–219, 2016.
- [26] RAMIRO, Í.; MARTÍ, A.; ANTOLÍN, E.; et al. Optically Triggered Infrared Photodetector. **Nano Letters**, v. 15, n. 1, p. 224–228, 2015.
- [27] RAFAILOV, E. U.; CATALUNA, M. A.; AVRUTIN, E. A. **Ultrafast Lasers Based on Quantum Dot Structures**. Weinheim, Germany: Wiley-VCH, 2011. .
- [28] JOYCE, P. B.; KRZYZEWSKI, T. J.; BELL, G. R.; et al. Optimizing the growth of 1.3 μm InAs/GaAs quantum dots. **Physical Review B**, v. 64, n. 23, p. 235317, 2001.
- [29] BENYOUCHEF, M.; YACOB, M.; REITHMAIER, J. P.; KETTLER, J.; MICHLER, P. Telecom-wavelength (1.5 μm) single-photon emission from InP-based quantum dots. **Applied Physics Letters**, v. 103, n. 16, p. 162101, 2013.
- [30] DIMROTH, F. High-efficiency solar cells from III-V compound semiconductors. **physica status solidi (c)**, v. 3, n. 3, p. 373–379, 2006.
- [31] GREEN, M. A.; EMERY, K.; HISHIKAWA, Y.; WARTA, W.; DUNLOP, E. D. Solar cell efficiency tables (version 47). **Progress in Photovoltaics: Research and Applications**, v. 24, n. 1, p. 3–11, 2016.
- [32] LUQUE, A.; MARTÍ, A. Increasing the Efficiency of Ideal Solar Cells by Photon

- Induced Transitions at Intermediate Levels. **Physical Review Letters**, v. 78, n. 26, p. 5014–5017, 1997.
- [33] BROWN, A. S.; GREEN, M. A. Intermediate band solar cell with many bands: Ideal performance. **Journal of Applied Physics**, v. 94, n. 9, p. 6150, 2003.
 - [34] LUQUE, A.; MARTÍ, A. The intermediate band solar cell: progress toward the realization of an attractive concept. **Advanced materials (Deerfield Beach, Fla.)**, v. 22, n. 2, p. 160–74, 2010.
 - [35] WU, J.; MAKABLEH, Y. F. M.; VASAN, R.; et al. Strong interband transitions in InAs quantum dots solar cell. **Applied Physics Letters**, v. 100, n. 5, p. 51907, 2012.
 - [36] KEIZER, J. G.; HENRIQUES, A. B.; MAIA, A. D. B.; QUIVY, A. A.; KOENRAAD, P. M. Atomically resolved study of the morphology change of InAs/GaAs quantum dot layers induced by rapid thermal annealing. **Applied Physics Letters**, v. 101, n. 24, p. 243113, 2012.
 - [37] DARUKA, I.; BARABÁSI, A.-L. Dislocation-Free Island Formation in Heteroepitaxial Growth: A Study at Equilibrium. **Physical Review Letters**, v. 79, n. 19, p. 3708–3711, 1997.
 - [38] TEICHERT, C. Self-organization of nanostructures in semiconductor heteroepitaxy. **Physics Reports**, v. 365, n. 5–6, p. 335–432, 2002.
 - [39] STANGL, J.; HOLÝ, V.; BAUER, G. Structural properties of self-organized semiconductor nanostructures. **Reviews of Modern Physics**, v. 76, n. 3, p. 725–783, 2004.
 - [40] GRUNDMANN, M.; STIER, O.; BIMBERG, D. InAs/GaAs pyramidal quantum dots: Strain distribution, optical phonons, and electronic structure. **Physical Review B**, v. 52, n. 16, p. 11969–11981, 1995.
 - [41] PRYOR, C.; KIM, J.; WANG, L. W.; WILLIAMSON, A. J.; ZUNGER, A. Comparison of two methods for describing the strain profiles in quantum dots. **Journal of Applied Physics**, v. 83, n. 5, p. 2548, 1998.
 - [42] SNYDER, C.; MANSFIELD, J.; ORR, B. Kinetically controlled critical thickness for coherent islanding and thick highly strained pseudomorphic films of $\text{In}_x\text{Ga}_{1-x}\text{As}$ on GaAs(100). **Physical Review B**, v. 46, n. 15, p. 9551–9554, 1992.
 - [43] RAMACHANDRAN, T. R.; HEITZ, R.; CHEN, P.; MADHUKAR, A. Mass transfer in Stranski–Krastanow growth of InAs on GaAs. **Applied Physics Letters**, v. 70, n. 5, p. 640, 1997.
 - [44] BARABÁSI, A.-L. Self-assembled island formation in heteroepitaxial growth. **Applied Physics Letters**, v. 70, n. 19, p. 2565, 1997.
 - [45] LEONARD, D.; POND, K.; PETROFF, P. M. Critical layer thickness for self-assembled InAs islands on GaAs. **Physical Review B**, v. 50, n. 16, p. 11687–11692, 1994.
 - [46] KOBAYASHI, N. P.; RAMACHANDRAN, T. R.; CHEN, P.; MADHUKAR, A. In situ, atomic force microscope studies of the evolution of InAs three-dimensional islands on GaAs(001). **Applied Physics Letters**, v. 68, n. 23, p. 3299, 1996.
 - [47] SCHINDLER, A. C.; GYURE, M. F.; SIMMS, G. D.; et al. Theory of strain relaxation in heteroepitaxial systems. **Physical Review B**, v. 67, n. 7, p. 75316, 2003.

- [48] TU, Y.; TERSOFF, J. Coarsening, Mixing, and Motion: The Complex Evolution of Epitaxial Islands. **Physical Review Letters**, v. 98, n. 9, p. 96103, 2007.
- [49] SPENCER, B. J.; TERSOFF, J. Symmetry breaking in shape transitions of epitaxial quantum dots. **Physical Review B**, v. 87, n. 16, p. 161301, 2013.
- [50] WU, J.; JIN, P. Self-assembly of InAs quantum dots on GaAs(001) by molecular beam epitaxy. **Frontiers of Physics**, v. 10, n. 1, p. 7–58, 2015.
- [51] LI, X. L.; WANG, C. X.; YANG, G. W. Thermodynamic theory of growth of nanostructures. **Progress in Materials Science**, v. 64, p. 121–199, 2014.
- [52] PEHLKE, E.; MOLL, N.; KLEY, A.; SCHEFFLER, M. Shape and stability of quantum dots. **Applied Physics A: Materials Science & Processing**, v. 65, n. 6, p. 525–534, 1997.
- [53] DARUKA, I.; TERSOFF, J.; BARABÁSI, A.-L. Shape Transition in Growth of Strained Islands. **Physical Review Letters**, v. 82, n. 13, p. 2753–2756, 1999.
- [54] KRATZER, P.; CHAKRABARTI, A.; LIU, Q. K. K.; SCHEFFLER, M. Theory of shape evolution of InAs quantum dots on In_{0.5}Ga_{0.5}As/InP(001) substrate. **New Journal of Physics**, v. 11, n. 7, p. 73018, 2009.
- [55] JOYCE, P. B.; KRZYZEWSKI, T. J.; BELL, G. R.; JOYCE, B. A.; JONES, T. S. Composition of InAs quantum dots on GaAs(001): Direct evidence for (In,Ga)As alloying. **Physical Review B**, v. 58, n. 24, p. R15981–R15984, 1998.
- [56] ROSENAUER, A.; GERTHSEN, D.; DYCK, D. VAN; et al. Quantification of segregation and mass transport in In_xGa_{1-x}As/GaAs Stranski-Krastanow layers. **Physical Review B**, v. 64, n. 24, p. 245334, 2001.
- [57] LEMAITRE, A.; PATRIARCHE, G.; GLAS, F. Composition profiling of InAs/GaAs quantum dots. **Applied Physics Letters**, v. 85, n. 17, p. 3717, 2004.
- [58] BIASIOL, G.; HEUN, S. Compositional mapping of semiconductor quantum dots and rings. **Physics Reports**, v. 500, n. 4–5, p. 117–173, 2011.
- [59] CHERKASHIN, N.; REBOH, S.; HÛTCH, M. J.; et al. Determination of stress, strain, and elemental distribution within In(Ga)As quantum dots embedded in GaAs using advanced transmission electron microscopy. **Applied Physics Letters**, v. 102, n. 17, p. 173115, 2013.
- [60] BULUTAY, C.; CHEKHOVICH, E. A.; TARTAKOVSKII, A. I. Nuclear magnetic resonance inverse spectra of InGaAs quantum dots: Atomistic level structural information. **Physical Review B**, v. 90, n. 20, p. 205425, 2014.
- [61] SOKOLOV, P. S.; PETROV, M. Y.; MEHRTENS, T.; et al. Reconstruction of nuclear quadrupole interaction in (In,Ga)As/GaAs quantum dots observed by transmission electron microscopy. **Physical Review B**, v. 93, n. 4, p. 45301, 2016.
- [62] WALTHER, T.; CULLIS, A. G.; NORRIS, D. J.; HOPKINSON, M. Nature of the Stranski-Krastanow Transition during Epitaxy of InGaAs on GaAs. **Physical Review Letters**, v. 86, n. 11, p. 2381–2384, 2001.
- [63] BIASIOL, G.; HEUN, S.; GOLINELLI, G. B.; et al. Surface compositional gradients of InAs/GaAs quantum dots. **Applied Physics Letters**, v. 87, n. 22, p. 223106, 2005.
- [64] BOSCHERINI, F.; CAPELLINI, G.; GASPARE, L. DI; et al. Ge-Si intermixing in Ge

- quantum dots on Si(001) and Si(111). **Applied Physics Letters**, v. 76, n. 6, p. 682, 2000.
- [65] LIAO, X. Z.; ZOU, J.; COCKAYNE, D. J. H.; LEON, R.; LOBO, C. Indium Segregation and Enrichment in Coherent $\text{In}_x\text{Ga}_{1-x}\text{As}/\text{GaAs}$ Quantum Dots. **Physical Review Letters**, v. 82, n. 25, p. 5148–5151, 1999.
- [66] BRULS, D. M.; VUGS, J. W. A. M.; KOENRAAD, P. M.; et al. Determination of the shape and indium distribution of low-growth-rate InAs quantum dots by cross-sectional scanning tunneling microscopy. **Applied Physics Letters**, v. 81, n. 9, p. 1708, 2002.
- [67] BLOKLAND, J. H.; BOZKURT, M.; ULLOA, J. M.; et al. Ellipsoidal InAs quantum dots observed by cross-sectional scanning tunneling microscopy. **Applied Physics Letters**, v. 94, n. 2, p. 23107, 2009.
- [68] GIDDINGS, A. D.; KEIZER, J. G.; HARA, M.; et al. Composition profiling of InAs quantum dots and wetting layers by atom probe tomography and cross-sectional scanning tunneling microscopy. **Physical Review B**, v. 83, n. 20, p. 205308, 2011.
- [69] BLANK, H.; LITVINOV, D.; SCHNEIDER, R.; et al. Quantification of the In-distribution in embedded InGaAs quantum dots by transmission electron microscopy. **Crystal Research and Technology**, v. 44, n. 10, p. 1083–1088, 2009.
- [70] TANAKA, R. Y.; ABE, N. M.; SILVA, E. C. F. DA; QUIVY, A. A.; PASSARO, A. Modeling the 3D In profile of $\text{In}_x\text{Ga}_{1-x}\text{As}/\text{GaAs}$ quantum dots. **Journal of Physics D: Applied Physics**, v. 49, n. 21, p. 215101, 2016.
- [71] LI, S.-S.; XIA, J.-B.; YUAN, Z. L.; et al. Effective-mass theory for InAs/GaAs strained coupled quantum dots. **Physical Review B**, v. 54, n. 16, p. 11575–11581, 1996.
- [72] HARRISON, P. **Quantum Wells, Wires and Dots: Theoretical and Computational Physics of Semiconductor Nanostructures**. 2nd ed. West Sussex: Wiley, 2005. .
- [73] NYE, J. F. **Physical Properties of Crystals: Their Representation by Tensors and Matrices**. Dordrecht: Clarendon Press, 1985. .
- [74] SMITH, D. L.; MAILHOT, C. Theory of semiconductor superlattice electronic structure. **Reviews of Modern Physics**, v. 62, n. 1, p. 173–234, 1990.
- [75] IPATOVA, I. P.; MALYSHKIN, V. G.; SHCHUKIN, V. A. On spinodal decomposition in elastically anisotropic epitaxial films of III-V semiconductor alloys. **Journal of Applied Physics**, v. 74, n. 12, p. 7198, 1993.
- [76] VURGAFTMAN, I.; MEYER, J. R.; RAM-MOHAN, L. R. Band parameters for III–V compound semiconductors and their alloys. **Journal of Applied Physics**, v. 89, n. 11, p. 5815, 2001.
- [77] ADACHI, S. **Properties of semiconductor alloys: group-IV, III-V and II-VI semiconductors**. John Wiley & Sons Inc, 2009. .
- [78] CHUANG, S. L. **Physics of Optoelectronic Devices**. Wiley, 1995. .
- [79] SEEGER, K. **Semiconductor physics: an introduction**. Berlin: Springer, 2010. .
- [80] FONSECA, L. R. C.; JIMENEZ, J. L.; LEBURTON, J. P.; MARTIN, R. M. Self-consistent calculation of the electronic structure and electron-electron interaction in self-assembled InAs-GaAs quantum dot structures. **Physical Review B**, v. 57, n. 7, p. 4017–4026, 1998.
- [81] PLANELLES, J.; CLIMENTE, J. I.; RAJADELL, F.; et al. Effect of strain and variable

mass on the formation of antibonding hole ground states in InAs quantum dot molecules. **Physical Review B**, v. 82, n. 15, p. 155307, 2010.

- [82] MARZIN, J.-Y.; GÉRARD, J.-M.; IZRAËL, A.; BARRIER, D.; BASTARD, G. Photoluminescence of Single InAs Quantum Dots Obtained by Self-Organized Growth on GaAs. **Physical Review Letters**, v. 73, n. 5, p. 716–719, 1994.
- [83] AOKI, T. Photoluminescence Spectroscopy. **Characterization of Materials**, 2012. Hoboken, NJ, USA: John Wiley & Sons, Inc.
- [84] SANGUINETTI, S.; MANO, T.; OSHIMA, M.; et al. Temperature dependence of the photoluminescence of InGaAs/GaAs quantum dot structures without wetting layer. **Applied Physics Letters**, v. 81, n. 16, p. 3067, 2002.
- [85] PERKOWITZ, S. **Optical characterization of semiconductors: infrared, raman, and photoluminescence spectroscopy**. London: Academic Press, 1993. .
- [86] BASTARD, G. **Wave mechanics applied to semiconductor heterostructures**. Les Éditions de Physique, 1988. .
- [87] BARAFF, G. A.; GERSHONI, D. Eigenfunction-expansion method for solving the quantum-wire problem: Formulation. **Physical Review B**, v. 43, n. 5, p. 4011–4022, 1991.
- [88] MUNKRES, J. R. **Topology; a First Course**. book, Prentice-Hall, 1974. .
- [89] DHATT, G.; LEFRANÇOIS, E.; TOUZOT, G. **Finite Element Method**. Hoboken: John Wiley & Sons, 2012. .
- [90] MAIA, A. D. B.; SILVA, E. C. F. DA; QUIVY, A. A.; et al. Simulation of the electronic properties of In_xGa_{1-x}As quantum dots and their wetting layer under the influence of indium segregation. **Journal of Applied Physics**, v. 114, n. 8, p. 83708, 2013.
- [91] BHATTACHARYA, P.; GHOSH, S.; STIFF-ROBERTS, A. D. QUANTUM DOT OPTO-ELECTRONIC DEVICES. **Annual Review of Materials Research**, v. 34, n. 1, p. 1–40, 2004.
- [92] BOXBERG, F.; TULKKI, J. Theory of the electronic structure and carrier dynamics of strain-induced (Ga, In)As quantum dots. **Reports on Progress in Physics**, v. 70, n. 8, p. 1425–1471, 2007.
- [93] PAN, D.; TOWE, E.; KENNERLY, S. Normal-incidence intersubband (In, Ga)As/GaAs quantum dot infrared photodetectors. **Applied Physics Letters**, v. 73, n. 14, p. 1937, 1998.
- [94] MAIMON, S.; FINKMAN, E.; BAHIR, G.; et al. Intersublevel transitions in InAs/GaAs quantum dots infrared photodetectors. **Applied Physics Letters**, v. 73, n. 14, p. 2003, 1998.
- [95] CHEN, Z.; BAKLENOV, O.; KIM, E. T.; et al. Normal incidence InAs/Al_xGa_{1-x}As quantum dot infrared photodetectors with undoped active region. **Journal of Applied Physics**, v. 89, n. 8, p. 4558, 2001.
- [96] GHADI, H.; SHETTY, S.; ADHIKARY, S.; et al. Enhancement in Peak Detectivity and Operating Temperature of Strain-Coupled InAs/GaAs Quantum Dot Infrared Photodetectors by Rapid Thermal Annealing. **IEEE Transactions on Nanotechnology**, v. 14, n. 4, p. 668–672, 2015.

- [97] LATINI, V.; PLACIDI, E.; ARCIPRETE, F.; PATELLA, F. In-line correlation and ordering of InAs/GaAs multistacked Quantum Dots structures. **Journal of Crystal Growth**, v. 419, p. 138–142, 2015.
- [98] MURAKI, K.; FUKATSU, S.; SHIRAKI, Y.; ITO, R. Surface segregation of In atoms during molecular beam epitaxy and its influence on the energy levels in InGaAs/GaAs quantum wells. **Applied Physics Letters**, v. 61, n. 5, p. 557, 1992.
- [99] BENDANIEL, D. J.; DUKE, C. B. Space-Charge Effects on Electron Tunneling. **Physical Review**, v. 152, n. 2, p. 683–692, 1966.
- [100] TANAKA, R. Y. **Metodologia computacional para projeto de dispositivos semicondutores nanoestruturados**, 2008. Instituto Nacional de Pesquisas Espaciais - INPE.
- [101] OFFERMANS, P.; KOENRAAD, P. M.; NÖTZEL, R.; WOLTER, J. H.; PIERZ, K. Formation of InAs wetting layers studied by cross-sectional scanning tunneling microscopy. **Applied Physics Letters**, v. 87, n. 11, p. 111903, 2005.
- [102] SCHOWALTER, M.; ROSENAUER, A.; GERTHSEN, D.; et al. Investigation of In segregation in InAs/AlAs quantum-well structures. **Applied Physics Letters**, v. 79, n. 26, p. 4426, 2001.
- [103] MARTINI, S.; QUIVY, A. A.; SILVA, M. J. DA; et al. Ex-situ investigation of indium segregation in InGaAs/GaAs quantum wells using high-resolution x-ray diffraction. **Journal of Applied Physics**, v. 94, n. 11, p. 7050, 2003.
- [104] DUSSAIGNE, A.; DAMILANO, B.; GRANDJEAN, N.; MASSIES, J. In surface segregation in InGaN/GaN quantum wells. **Journal of Crystal Growth**, v. 251, n. 1–4, p. 471–475, 2003.
- [105] MARTINI, S.; QUIVY, A. A.; SILVA, E. C. F. DA; LEITE, J. R. Real-time determination of the segregation strength of indium atoms in InGaAs layers grown by molecular-beam epitaxy. **Applied Physics Letters**, v. 81, n. 15, p. 2863, 2002.
- [106] HAXHA, V.; DROUZAS, I.; ULLOA, J.; et al. Role of segregation in InAs/GaAs quantum dot structures capped with a GaAsSb strain-reduction layer. **Physical Review B**, v. 80, n. 16, p. 165334, 2009.
- [107] PELÁ, R. R.; TELES, L. K.; MARQUES, M.; MARTINI, S. Theoretical study of the indium incorporation into III-V compounds revisited: The role of indium segregation and desorption. **Journal of Applied Physics**, v. 113, n. 3, p. 33515, 2013.
- [108] MAIA, A. D. B.; SILVA, E. C. F. DA; QUIVY, A. A.; et al. The influence of different indium-composition profiles on the electronic structure of lens-shaped $\text{In}_x\text{Ga}_{1-x}\text{As}$ quantum dots. **Journal of Physics D: Applied Physics**, v. 45, n. 22, p. 225104, 2012.
- [109] KERN, M. **Numerical Methods for Inverse Problems**. Hoboken: Wiley, 2016. .
- [110] BIANCHI, L.; DORIGO, M.; GAMBARDELLA, L. M.; GUTJAHR, W. J. A survey on metaheuristics for stochastic combinatorial optimization. **Natural Computing**, v. 8, n. 2, p. 239–287, 2009.
- [111] BOUSSAÏD, I.; LEPAGNOT, J.; SIARRY, P. A survey on optimization metaheuristics. **Information Sciences**, v. 237, n. 10, p. 82–117, 2013.
- [112] TALBI, E. G. **Metaheuristics: From Design to Implementation**. Hoboken: Wiley, 2009. .

- [113] TRELEA, I. C. The particle swarm optimization algorithm: convergence analysis and parameter selection. **Information Processing Letters**, v. 85, n. 6, p. 317–325, 2003.
- [114] KENNEDY, J.; EBERHART, R. Particle swarm optimization. . In: Proceedings of ICNN'95 - International Conference on Neural Networks, 1995, Piscataway, NJ, USA. **Proceedings...** Piscataway, NJ, USA: IEEE, 1995. p. 1942–1948.
- [115] HATAMLOU, A. Black hole: A new heuristic optimization approach for data clustering. **Information Sciences**, v. 222, p. 175–184, 2013.
- [116] GOLDBERG, D. E.; HOLLAND, J. H. Genetic Algorithms and Machine Learning. **Machine Learning**, v. 3, n. 2/3, p. 95–99, 1988.
- [117] GOLDBERG, D. E. **Genetic Algorithms in Search, Optimization, and Machine Learning**. Addison-Wesley Publishing Company, 1989. .
- [118] KRISHNA, S. Quantum dots-in-a-well infrared photodetectors. **Journal of Physics D: Applied Physics**, v. 38, n. 13, p. 2142–2150, 2005.
- [119] KRISHNA, S.; FORMAN, D.; ANNAMALAI, S.; et al. Demonstration of a 320x256 two-color focal plane array using InAs/InGaAs quantum dots in well detectors. **Applied Physics Letters**, v. 86, n. 19, p. 193501, 2005.
- [120] ARIYAWANSA, G.; PERERA, A. G. U.; RAGHAVAN, G. S.; et al. Effect of well width on three-color quantum dots-in-a-well infrared detectors. **IEEE Photonics Technology Letters**, v. 17, n. 5, p. 1064–1066, 2005.
- [121] SELLERS, I. R.; MOWBRAY, D. J.; BADCOCK, T. J.; et al. Infrared modulated interlevel spectroscopy of 1.3 μm self-assembled quantum dot lasers using a free electron laser. **Applied Physics Letters**, v. 88, n. 8, p. 81108, 2006.
- [122] RAGHAVAN, S.; FORMAN, D.; HILL, P.; et al. Normal-incidence InAs/In[_{0.15}]Ga[_{0.85}]As quantum dots-in-a-well detector operating in the long-wave infrared atmospheric window (8–12 μm). **Journal of Applied Physics**, v. 96, n. 2, p. 1036, 2004.
- [123] CHAGANTI, V. R.; APALKOV, V. Theoretical study of intraband optical transitions in conduction band of dot-in-a-well system. **AIP Advances**, v. 4, n. 2, p. 27125, 2014.
- [124] LEE, J.-H.; WU, Z.-M.; LIAO, Y.-M.; et al. The operation principle of the well in quantum dot stack infrared photodetector. **Journal of Applied Physics**, v. 114, n. 24, p. 244504, 2013.
- [125] CHAKRABARTI, S.; STIFF-ROBERTS, A. D.; BHATTACHARYA, P.; et al. High-Temperature Operation of InAs–GaAs Quantum-Dot Infrared Photodetectors With Large Responsivity and Detectivity. **IEEE Photonics Technology Letters**, v. 16, n. 5, p. 1361–1363, 2004.
- [126] CHEN, S. M.; ZHOU, K. J.; ZHANG, Z. Y.; et al. Ultra-broad spontaneous emission and modal gain spectrum from a hybrid quantum well/quantum dot laser structure. **Applied Physics Letters**, v. 100, n. 4, p. 41118, 2012.
- [127] KHAN, M. Z. M.; NG, T. K.; LEE, C.-S.; BHATTACHARYA, P.; OOI, B. S. Chirped InAs/InP quantum-dash laser with enhanced broad spectrum of stimulated emission. **Applied Physics Letters**, v. 102, n. 9, p. 91102, 2013.
- [128] LAGHUMAVARAPU, R. B.; EL-EMAWY, M.; NUNTAWONG, N.; et al. Improved device performance of InAs/GaAs quantum dot solar cells with GaP strain compensation

- layers. **Applied Physics Letters**, v. 91, n. 24, p. 243115, 2007.
- [129] GUIMARD, D.; MORIHARA, R.; BORDEL, D.; et al. Fabrication of InAs/GaAs quantum dot solar cells with enhanced photocurrent and without degradation of open circuit voltage. **Applied Physics Letters**, v. 96, n. 20, p. 203507, 2010.
- [130] TOMIĆ, S. Intermediate-band solar cells: Influence of band formation on dynamical processes in InAs/GaAs quantum dot arrays. **Physical Review B**, v. 82, n. 19, p. 195321, 2010.
- [131] LEDENTSOV, N.; SHCHUKIN, V.; GRUNDMANN, M.; et al. Direct formation of vertically coupled quantum dots in Stranski-Krastanow growth. **Physical Review B**, v. 54, n. 12, p. 8743–8750, 1996.
- [132] KIM, H. S.; SUH, J. H.; PARK, C. G.; et al. Effects of the thickness of GaAs spacer layers on the structure of multilayer stacked InAs quantum dots. **Journal of Crystal Growth**, v. 311, n. 2, p. 258–262, 2009.
- [133] BETCKE, M. M.; VOSS, H. Numerical simulation of electronic properties of coupled quantum dots on wetting layers. **Nanotechnology**, v. 19, n. 16, p. 165204, 2008.

Appendix A – Semiconductor parameters values

TABLE A.1 – Values of parameters E_g^0 , A and B. Sources [76, 78].

Compound	E_g^0 (eV)	A (eV/K)	B (K)
GaAs	1.519	0.5405×10^{-3}	204
AlAs	3.099	0.885×10^{-3}	530
InAs	0.4105	0.276×10^{-3}	93
GaP	2.886	$E_g^0 + 0.1081[1 - \coth(164/T)]$	
AlP	3.63	0.5771×10^{-3}	372
InP	1.4236	0.363×10^{-3}	162
GaSb	0.812	0.417×10^{-3}	140
AlSb	2.386	0.42×10^{-3}	140
InSb	0.235	0.32×10^{-3}	170
GaN-ZB	3.299	0.593×10^{-3}	600
AlN-ZB	4.9	0.593×10^{-3}	600
InN-ZB	1.94	0.245×10^{-3}	624

TABLE A.2 – Values of parameters F , E_P , Δ_{SO} , γ_1 , γ_2 , and VBO. Source [76].

Material	F	E_P (eV)	Δ_{SO} (eV)	γ_1	γ_2	VBO (eV)
GaAs	−1.94	28.8	0.341	6.98	2.06	−0.80
AlAs	−0.48	21.1	0.28	3.76	0.82	−1.33
InAs	−2.90	21.5	0.39	20.0	8.5	−0.59
GaP	−2.04	31.4	0.08	4.05	0.49	−1.27
AlP	−0.65	17.7	0.07	3.35	0.71	−1.74
InP	−1.31	20.7	0.108	5.08	1.60	−0.94
GaSb	−1.63	27.0	0.76	13.4	4.7	−0.03
AlSb	−0.56	18.7	0.676	5.18	1.19	−0.41
InSb	−0.23	23.3	0.81	34.8	15.5	0
GaN-ZB	−0.92	25.0	0.017	2.67	1.92	−2.64
AlN-ZB	0.76	27.1	0.019	0.75	0.47	−3.44
InN-ZB	−0.92	25.0	0.006	1.10	0.85	−2.38

TABLE A.3 – Values of parameters C_{11} , C_{12} , C_{44} , a_c , a_v , b e a^{lc} . Sources [76, 78].

Material	C_{11} (GPa)	C_{12} (GPa)	C_{44} (GPa)	a_c (eV)	a_v (eV)	b (eV)	a^{lc} (Å)
GaAs	1187.9	537.6	600	−7.17	1.16	−1.7	5.6533
AlAs	1250	534	542	−5.64	2.47	−2.3	5.66
InAs	832.9	452.6	395.9	−5.08	1.0	−1.8	6.0584
GaP	1405	620.3	703.3	−8.2	1.7	−1.6	5.45
AlP	1330	630	615	−5.7	3.0	−1.5	5.47
InP	1011	561	456	−6.0	0.6	−2.0	5.87
GaSb	884.2	402.6	432.2	−7.5	0.8	−2.0	6.10
AlSb	876.9	434.1	407.6	−4.5	1.4	−1.35	6.14
InSb	684.7	373.5	311.1	−6.94	0.36	−2.0	6.48
GaN-ZB	293	159	155	−2.2	5.2	−2.2	4.50
AlN-ZB	304	160	193	−6.0	3.4	−1.9	4.38
InN-ZB	187	125	86	−1.85	1.5	−1.2	4.98

TABLE A.4 – Bowing values for ternary alloys. Source [76].

Material	E_g	Δ_{so}	E_p	F	VBO	a^{lc}
Al_xGa_{1-x}As	−0.127+1.310x	-	-	-	-	-
In_xGa_{1-x}As	0.477	0.15	−1.48	1.77	−0.38	2.61
Al_xIn_{1-x}As	0.70	0.15	−4.81	−4.44	−0.64	−1.4
Ga_xIn_{1-x}P	0.65	-	-	0.78	-	-
Al_xIn_{1-x}P	−0.48	−0.19	-	-	-	-
Ga_xIn_{1-x}Sb	0.415	0.1	-	−6.84	-	-
Al_xIn_{1-x}Sb	0.43	0.25	-	-	-	-
Al_xGa_{1-x}Sb	−0.044+1.22x	0.3	-	-	-	-
Ga_xAs_{1-x}Sb	1.43	0.6	-	-	−1.06	-
InAs_{1-x}Sb_x	0.67	1.2	-	-	-	-
AlAs_{1-x}Sb_x	0.8	0.15	-	-	−1.71	-
GaAs_{1-x}P_x	0.19	-	-	-	-	-
InAs_{1-x}P_x	0.10	0.16	-	-	-	-

Appendix B – Solution of the Schrödinger equation for the infinite spherical potential well

The infinite spherical potential well could be defined in spherical coordinates (r, θ, φ) as

$$V(r) = \begin{cases} 0, & \text{if } 0 \leq r \leq a \\ \infty, & \text{if } r > a \end{cases}. \quad (\text{B.8})$$

It is well known from the studies of hydrogen atom that the wave function that describes the particle behavior can be separated in two different independent functions when it is in a potential with spherical symmetry:

$$\psi(r, \theta, \varphi) = R(r)Y(\theta, \varphi), \quad (\text{B.9})$$

where $Y(\theta, \varphi)$ is the spherical harmonics function and $R(r)$ is the radial function. Hence, the radial Schrödinger equation could be separated in angular and radial components:

$$\begin{cases} \frac{-\hbar^2}{Y(\theta, \varphi)} \left\{ \frac{1}{\sin \theta} \frac{\partial}{\partial \theta} \left[\sin \theta \frac{\partial Y(\theta, \varphi)}{\partial \theta} \right] + \frac{1}{\sin^2 \theta} \frac{\partial^2 Y(\theta, \varphi)}{\partial \varphi^2} \right\} = -l(l+1)\hbar^2 \\ \frac{-\hbar^2}{R(r)} \frac{\partial}{\partial r} \left[r^2 \frac{\partial R(r)}{\partial r} \right] + 2mr^2[V(r) - E] = -l(l+1)\hbar^2 \end{cases}, \quad (\text{B.10})$$

where l is a quantum number ($l = 0, 1, 2, \dots$). The angular part is potential independent and does not interfere in the energy of the eigenstates. Hence, to obtain the energies we must solve the radial part of the Schrödinger equation:

$$r^2 \frac{\partial^2 R(r)}{\partial r^2} + 2r \frac{\partial R(r)}{\partial r} - l(l+1)R(r) - \frac{2mr^2}{\hbar^2} V(r)R(r) + \frac{2mr^2}{\hbar^2} E R(r) = 0. \quad (\text{B.11})$$

Remembering that the potential is null inside the QD and introducing two variables, $k = \sqrt{\frac{2mE}{\hbar^2}}$ and $z = kr$, the radial component of the Schrödinger equation can be written as

$$z^2 \frac{\partial^2 R(z)}{\partial z^2} + 2z \frac{\partial R(z)}{\partial z} + [z^2 - l(l+1)]R(z) = 0, \quad (\text{B.12})$$

which is the spherical Bessel equation with the well-known solutions:

$$j_l(z) = (-z)^l \left(\frac{1}{z} \frac{\partial}{\partial z} \right)^l \left(\frac{\sin z}{z} \right), \quad (\text{B.13})$$

and

$$y_l(z) = -(-z)^l \left(\frac{1}{z} \frac{\partial}{\partial z} \right)^l \left(\frac{\cos z}{z} \right). \quad (\text{B.14})$$

The functions $y_l(z)$ are irregular solutions because they are non-integrable in the interval containing $z = 0$, hence unphysical. It follows that the radial wave function $R(r)$ is thus proportional to $j_l(kr)$ only. In order to satisfy the boundary condition at $r = a$, the value of k must be chosen such that ka corresponds to one of the zeros of the $j_l(z)$. If we denote the n^{th} zero of $j_l(z)$ as z_l^n , then $z_l^n = ka$ and the allowed energy levels are given by

$$E_l^n = \frac{\hbar^2}{2m} \left(\frac{z_l^n}{a} \right)^2. \quad (\text{B.15})$$

The zeros of the spherical Bessel function for $1 \leq n \leq 4$ and $0 \leq l \leq 4$ are shown in Table B.1.

TABLE B.1: Some zeros of the spherical Bessel function j_l .

z_l^n	$n = 1$	$n = 2$	$n = 3$	$n = 4$
$l = 0$	3.141593	6.283185	9.424778	12.566371
$l = 1$	4.493409	7.725252	10.904122	14.066194
$l = 2$	5.763459	9.095011	12.322941	15.514603
$l = 3$	6.987932	10.417119	13.698023	16.923621
$l = 4$	8.182561	11.704907	15.039665	18.301256

FOLHA DE REGISTRO DO DOCUMENTO

1. CLASSIFICAÇÃO/TIPO TD	2. DATA 20 de dezembro de 2016	3. REGISTRO N° DCTA/ITA/TD-043/2016	4. N° DE PÁGINAS 103
5. TÍTULO E SUBTÍTULO: Study of Indium Segregation in Self-Assembled Quantum Dots.			
6. AUTOR(ES): Roberto Yuji Tanaka			
7. INSTITUIÇÃO(ÕES)/ÓRGÃO(S) INTERNO(S)/DIVISÃO(ÕES): Instituto Tecnológico de Aeronáutica – ITA			
8. PALAVRAS-CHAVE SUGERIDAS PELO AUTOR: 1. Quantum dot. 2. Indium segregation. 3. Inverse problem.			
9. PALAVRAS-CHAVE RESULTANTES DE INDEXAÇÃO: Pontos quânticos semicondutores; Índio (elemento metálico); Problemas inversos; Teoria do quantum; Método de elementos finitos; Equação de Schroedinger; Nanoestruturas; Física.			
10. APRESENTAÇÃO: (X) Nacional () Internacional ITA, São José dos Campos. Curso de Doutorado. Programa de Pós-Graduação em Ciências e Tecnologias Espaciais. Área de Sensores e Atuadores Espaciais. Orientador: Prof. Dr. Angelo Passaro. Coorientadora: Profª. Drª. Euzi Conceição Fernandes da Silva. Defesa em 13/12/2016. Publicada em 2016.			
11. RESUMO: Self-assembled InAs/GaAs quantum dots have a non-homogeneous indium composition profile resulting from segregation and intermixing effects. Currently, there is not a method to obtain any real-time information on the migration of atoms inside the quantum dots. <i>Ex-situ</i> x-ray measurements are always possible, but in general, the very small volume of the quantum dots makes the signal almost insensitive to the indium gradient inside these nanostructures. The description of this indium composition profile is most crucial in any calculation. This thesis presents a novel iterative procedure that combines a Finite Element based solver for the Schrödinger equation and a metaheuristic optimization to match experimental photoluminescence peaks by fine-tuning the indium distribution inside $\text{In}_x\text{Ga}_{1-x}\text{As}/\text{GaAs}$ quantum dots grown by molecular-beam epitaxy. This procedure takes into account both the vertical and radial indium-composition profiles resulting from segregation and intermixing effects.			
12. GRAU DE SIGILO: <div style="text-align: center;">(X) OSTENSIVO () RESERVADO () SECRETO</div>			